Development of a Prototype Detector for Supernovae Neutrinos

A thesis submitted to The University of Manchester for the degree of Doctor of Philosophy in the Faculty of Science and Engineering

2004

Cristian Bungau

THE UNIVERSITY of MANCHESTER

Particle Physics Group
Department of Physics and Astronomy

Contents

List of Figures

List of Tables

Abstract

Due to the tremendous neutrino luminosity generated during stellar collapse, the detection of supernovae neutrinos would provide a unique scenario for extremely long baseline measurements, allowing a vastly increased region of neutrino mixing parameter space to be probed, and placing more stringent limits than can otherwise be achieved on neutrino masses and mixing angles.

In this thesis I present my work on the development of a prototype detector for the study of neutrino bursts from supernovae within our Galaxy. This involves the use of gadolinium and scintillators to detect the neutrons produced by the neutrino collisions. Large organic plastic scintillators have been tested for the possible use in the OMNIS (Observatory for Multiflavour Neutrino Interactions from Supernovae) experiment. The calibration of the detector is performed and the response of the scintillators to gammas emitted following the neutron capture on Gd is analysed in some detail.

Simulations using GEANT4 of the particle interactions inside the detector were performed to investigate the optimum configurations for the detector with respect to neutron detection efficiency.

Declaration

No portion of the work referred to in this thesis has been submitted in support of an application for another degree or qualification of this or any other university or other institute of learning.

The Author

The author was educated at the University of Bucharest, Romania, before joining the Department of Physics and Astronomy at the University of Manchester. The work presented here was undertaken at The University of Manchester.

Acknowledgements

A lot of people deserve to be mentioned here. I would like to thank my supervisor, Robin Marshall, for getting me involved in the project, and for his help and constructive comments on the writing of this thesis. Thanks must also go to all the members of the Manchester HEP group, with whom working has always been a pleasure, in particular John Allison for the help with the GEANT simulation and Andrew Elvin for helping me lift the 'so-heavy' scintillator blocks.

I would like to say THANK YOU in particular to Keith Stephens for his constant help and support throughout my time at Manchester. There are not enough words in the English language to thank you enough.

I would also like to thank my wife once more for her continuous support (both moral and technical with the C++ simulations) and her infinite patience, and to my parents for staying by me all the way and even further.

Chapter 1

Introduction

The optically visible Universe is made of stars and galaxies of all shapes and sizes. What it can not be seen, however, it is that it is filled with low mass, charge-less particles called neutrinos. These particles were created less than one second after the Big Bang, and large numbers of these primordial particles remain in the Universe today because they interact only very weakly with matter. Indeed, every cubic centimetre of space contains about 300 of these relics [1]. These neutrinos are very low energy; they are so low in fact, that they can not be detected. These neutrinos, along with microwave radiation, are believed to constitute the cosmic background radiation that permeates the entire Universe.

Neutrinos come also from other several sources. They are produced during the stellar evolution of stars such as our own Sun, where four protons combine with two electrons to form a helium nucleus and two electron neutrinos. In addition there are the so-called man-made sources, such as particle accelerators used to smash high energy particles into fixed or moving targets.

Neutrinos are arguably the least understood particles in the standard model of particle physics, with a potential to show evidence for new physics beyond the Standard Model. They are a fundamental part of nature and relatively little is known about them.

1.1 Birth of Neutrinos

Neutrinos have been shrouded in mystery since they were first suggested by Wolfgang Pauli, as a "desperate remedy" to save the law of energy conservation, which was under threat from observations of beta decay in radioactive materials. The beta radiation (electron), the presumed only particle emitted, should have a well fixed energy. Instead, following studies performed by Lise Meitner, Otto Hahn, Wilson and von Baeyer, James Chadwick showed in 1914 that this was not the case: the electron had a continuous energy spectrum. This finding even led Niels Bohr to speculate that the energy may not be conserved in these processes. The solution to this problem is due to Pauli who proposed in 1930 the existence of a new neutral particle with intrinsic angular momentum (spin) of $\hbar/2$, where $\hbar$ is Planck's constant divided by 2π. Initially Pauli dubbed this particle the "neutron". It was not until three years later, after James Chadwick discovered the neutron in 1932, that Pauli admitted the possibility of a zero mass neutral particle. Fermi re-named the particle and he called it neutrino.

1.2 The Standard Model of Particle Physics

Within the Standard Model of particle physics all the elementary particles are grouped into three families or generations - six quarks and six leptons (see Fig. 1.1).

Matter is built from members of the lightest generation: the up and down quarks that make up protons and neutrons, the electron and the electron neutrino, ν_e, involved in beta decay. Heavier versions of these particles, but with equal quantum numbers, are observed in decay processes and are comprised by the second and third generations. Each of this particle has a correspondent antiparticle with opposite electric charge.

Within the Standard Model there are also particles that transmit the interactions between these elementary particles. There are four known fundamental interactions between these particles: the strong interaction (mediated by eight *gluons*), the elec-

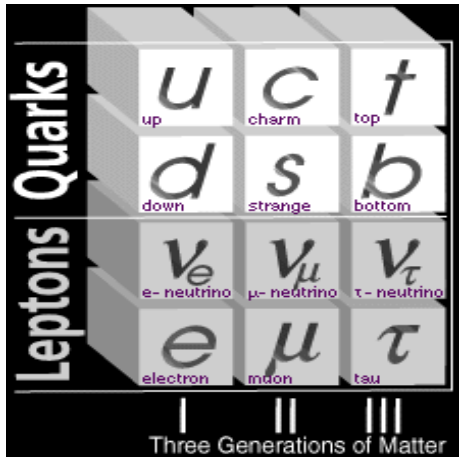

Figure 1.1: Elementary particles within the Standard Model [2]

tromagnetic interaction (carried by *photons*) and the weak interaction (mediated by the massive W^+, W^- and Z^0 particles). The gravitational interaction was not included in the Standard Model. The neutrinos interact only via the weak interaction and this allows them to pass through Earth without any deviation or so and makes them difficult to detect.

Although the Standard Model cannot predict the mass of these particles, it does provide a mechanism whereby they can acquire mass. This was done by introducing a new particle called the Higgs boson that fills the "vacuum". The interaction between a particle and the Higgs boson is considered to be the explanation for the particle mass. For example an electron cannot travel through vacuum at the speed of light, it has to become massive and the mass of a particle is proportional to the interaction rate between that particle and the Higgs boson.

The study of the neutrinos from inverse beta decay of ^{152}Eu has proved that the neutrino is a left-handed particle, i.e. its spin always points in the opposite direction of its momentum. But in the Standard Model the handedness of a particle changes each time it interacts with the Higgs boson which implies that the neutrino has to be massless if the Standard Model is a complete theory.

The Standard Model describes extremely well all known particle physics phenomena and, at present, it provides the most elegant theoretical framework. However the

Standard Model is far from being a complete theory. Detectors at LHC at CERN and Fermilab are searching for the Higgs particle, which, if found, will either explain the Standard Model or force us to readjust our conception of matter. Also the Standard Model does not include gravity, which does not play a significant part in atomic and subatomic processes because it is too weak on those scales.

On 5th of June 1998, the SuperKamiokande collaboration announced the first evidence for neutrino mass [3]. The observation of neutrino masses and lepton mixing constitutes the first confirmed evidence for physics beyond the Standard Model.

1.3 The Solar Neutrino Problem

The neutrinos produced in the fusion reactions in the core of the Sun can also be detected using large underground detectors on Earth. The measured neutrino flux can be compared with the theoretical predictions based on our understanding of how the Sun works and the the Standard Model (SM) of particle physics. Solar neutrino experiments such as Homestake [28], Kamiokande [29], GALLEX [30], SAGE [34] and Super-Kamiokande [35] suggest a flux of $\nu_e's$ inconsistent with the Bahcall-Pinsonneault standard solar model [50]. The measured flux is roughly one half of the flux expected from theory. Every experiment has measured only between one and two thirds of the expected neutrino flux and this represents the so-called "solar neutrino problem". This implied that either our theoretical model of particle physics is wrong or the model describing the interior of the Sun is incorrect (see Fig. 1.2).

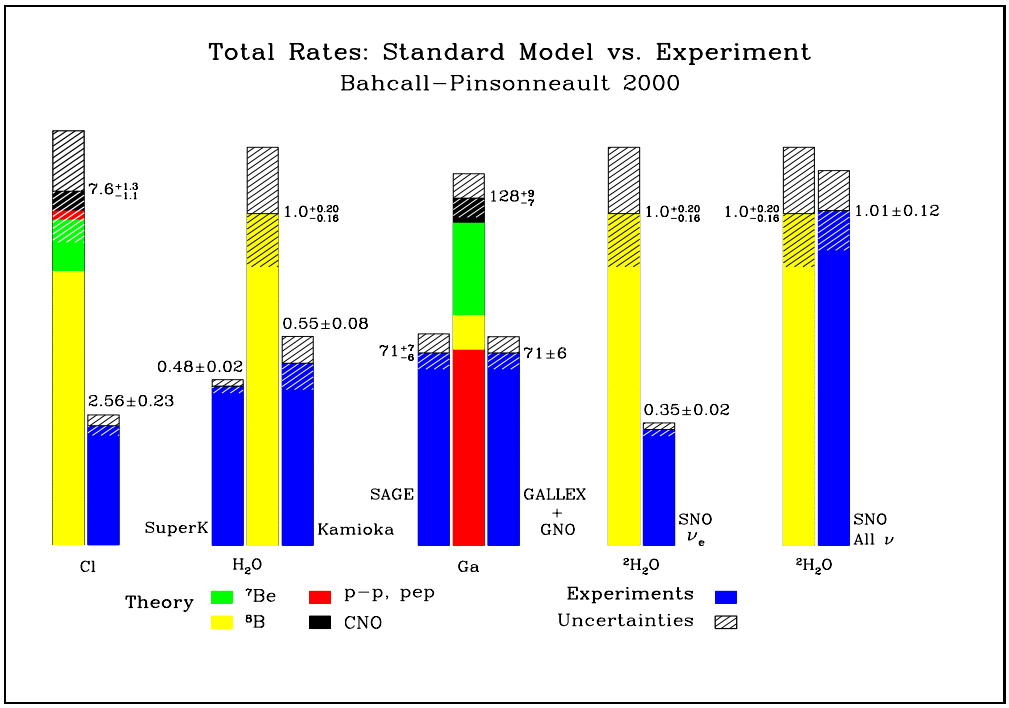

Figure 1.2: Discrepancies between the Standard Model predictions and the experimental data for solar neutrinos [26]

The most favoured solution to these discrepancies is an extension of the standard model of particle physics to one in which the neutrinos have mass and are allowed to oscillate between flavours via the vacuum and/or the Mikheyev-Smirnov-Wolfenstein (MSW-) oscillation mechanism [50]. The favoured MSW solution implies that the ν_e's emitted by the Sun converted or "oscillated" to ν_μ's or ν_τ's before arriving to the detector. This implies that there is a finite mass difference between the mass eigenstates of the three neutrino flavours and therefore the neutrinos must have a nonzero mass.

Atmospheric neutrino experiments at Super-Kamiokande [22], IMB [23], Soudan2 [24] and Kamiokande [25] also exhibit a disappearance of ν_μ [27].

Although the neutrino oscillation experiments proved that the neutrinos are massive particles, to date, no experiment has measured an absolute, non-zero neutrino mass.

1.4 The Need for a Neutral-Current Based Neutrino Detector

Many experiments have been designed to determine the mass of the neutrino. The direct measurements of the neutrino masses [4] provide only upper limits on the masses of all three neutrino flavours.

Neutrino flavour	Upper mass limit	Confidence level
ν_e	m $\leq$ 3 eV	90%
ν_μ	m $\leq$ 170 keV	90%
ν_τ	m $\leq$ 18.2 MeV	95%

Table 1.1: Upper Limits on Neutrino Masses

This lack of a definite neutrino mass measurement has led to the proposal made by Zatsepin [5] in 1968 to use the neutrino flux from a supernova to determine the neutrino mass. During the final stages of stellar evolution, the core of a massive star undergoes a catastrophic implosion, in which only about 1% of the gravitational binding energy of the neutron star goes into the shock wave that explodes the star, and about 0.01% into visible light. The remaining 98.99% is carried out into space by the neutrino flux.

The characteristics of a SN explosion can be predicted and modelled so that predictions about the nature of the neutrino flux can be made. The standard model [6] of this process suggests that the resulting neutrinos have the mean energies given in Table 1.2.

According to conventional supernova theory [7], the recently observed supernova explosion [8] (SN19897A) in the nearby Large Magellanic Cloud should have released approximately 3×10^{46} J of gravitational binding energy in a burst consisting of $\sim 10^{58}$ neutrinos over a time interval of a few seconds. The $\overline{\nu_e}$ observed by the Kamiokande [20] and IMB [19] from supernova 1987-A confirmed that neutrinos play

Neutrino flavour	Mean Energy Value
ν_e	E = 11 MeV
$\overline{\nu_e}$	E = 16 MeV
$\nu_\mu, \nu_\tau, \overline{\nu_\mu}, \overline{\nu_\tau}$	E = 25 MeV

Table 1.2: The Mean Values of the Neutrino Energies

an important role in core collapse supernovae. The observed neutrinos were detected over a few seconds, much longer than the weak interactions time-scales which are thought to be required to produce them. This confirmed the main features of the standard model of core-collapse supernovae and suggests that the behaviour of the neutrino opacity in matter beyond nuclear densities is understood [50].

Most of the current neutrino detectors are primarily sensitive to charged-current interactions of $\overline{\nu_e}$ with protons in water or mineral oil.

OMNIS, the proposed supernova observatory, will detect neutrinos originating from a core collapse supernova by the detection of spalled neutrons from Pb- or Fe-nuclei. OMNIS is being designed to provide a much larger sample of $\mu-$ and $\tau-$ neutrino events than would be provided by other detectors, allowing a significantly more detailed measurement of the neutrino spectra for different flavours, resolved in time, and the stellar conditions that produced them [50].
An observation of the fluxes of different neutrino flavours is also vital for the understanding of core-collapse supernovae and helpful for the investigation of new physics beyond the Standard Model. In this context, the need for a large neutral-current neutrino detector has become increasingly pressing in recent years [36].

It is the goal of this thesis to describe the developments leading to the design and construction of a neutron detector suitable for use in the OMNIS experiment. To begin with, chapter 2 will describe the properties of OMNIS, a proposed neutrino observatory. Here the neutrino detection mechanism will be discussed in some detail. Chapter three gives an outline of the theory of particle interaction processes inside

the detector. Chapter four describes the experimental set up of the OMNIS detector and describes the selection of large plastic scintillator blocks to build and test a prototype detector which can be used in the OMNIS project for neutron detection. Chapter five describes the analysis of the experimental data and shows that the prototype detector can be used in the OMNIS project. Chapter six shows the results of the simulation of particle interactions inside the detector using GEANT4 and gives the more specific analysis of the experimental and simulated data. Chapter seven presents the results for the optimum configuration for the detector with respect to neutron detection efficiency. Chapter eight summarises the results.

Chapter 2

Motivation and Properties of OMNIS

2.1 Stellar Evolution until Collapse

The only large fluxes of neutrinos from outside our solar system that could be detected on Earth are those from supernovae produced by the collapse of massive stars. It is believed that core-collapse supernovae are the final stage of the evolution of stars with masses between 8 and 60 solar masses. Lighter stars end their life as white dwarfs, whereas heavier stars are unstable and probably collapse into black holes without a supernova explosion.

A star is born when a cloud of gas (mainly hydrogen) contracts due to the gravitational force and to the radiative losses. As a consequence, the central temperature increases until thermonuclear fusion begins, when four hydrogen nuclei form a helium nucleus:

$$^{1}\mathrm{H} + {}^{1}\mathrm{H} \rightarrow {}^{2}\mathrm{H} + e^{+} + \nu_e \tag{2.1}$$

$$^{2}\mathrm{H} + {}^{1}\mathrm{H} \rightarrow {}^{3}\mathrm{He} + \gamma \tag{2.2}$$

$$^{3}\mathrm{He} + {}^{3}\mathrm{He} \rightarrow {}^{4}\mathrm{He} + 2\,{}^{1}\mathrm{H} + \gamma \tag{2.3}$$

So overall,

$$6\,^{1}\mathrm{H} \rightarrow {}^{4}\mathrm{He} + 2\,e^{+} + 2\,\nu_e + 3\,\gamma + 2\,^{1}\mathrm{H} \tag{2.4}$$

which can also be written as

$$4\,^{1}\mathrm{H} \rightarrow {}^{4}\mathrm{He} + 2\,e^{+} + 2\,\nu_e + 3\,\gamma \tag{2.5}$$

This cycle is called the pp chain and describes the evolution of a star of mass comparable to the mass of our Sun. The star will reach the main stage of its evolution when the nuclear fusion of the hydrogen in the centre of the newly formed star compensates the radiative losses at the surface. In the centre the ^{4}He is developing; however, at this early stage in the stellar evolution, elements with higher Z can't be produced because the energies of the nuclei which could undergo this process are not high enough to exceed the Coulomb potential.

For heavier stars the main sequence phase is the burning of H to He in core via the CNO cycle. The first collapse takes place when the helium core can no longer sustain the pressure caused by the gravitational field. This happens at less than 10^8 years from the birth of the star if its mass is greater than 8 $M_\odot$ ($M_\odot$ being the solar mass). The collapse temperature of the helium core will suddenly increase allowing the fusion of He nuclei and the formation of C.

The burning of He will take place for less than 10^6 years. During this period several collapses will take place, followed by the fusion of C, N, O and at the end Si, in alternating layers forming an onion-like interior structure (Fig. 2.1). The Fe nucleus has the highest binding energy and therefore there is no more thermonuclear fuel to burn: the iron core is endothermic; it can only absorb energy by breaking into lighter nuclei or creating heavier elements [15]. It will be the last to form in this sequence of fusion processes and it will form the inner core of the star.

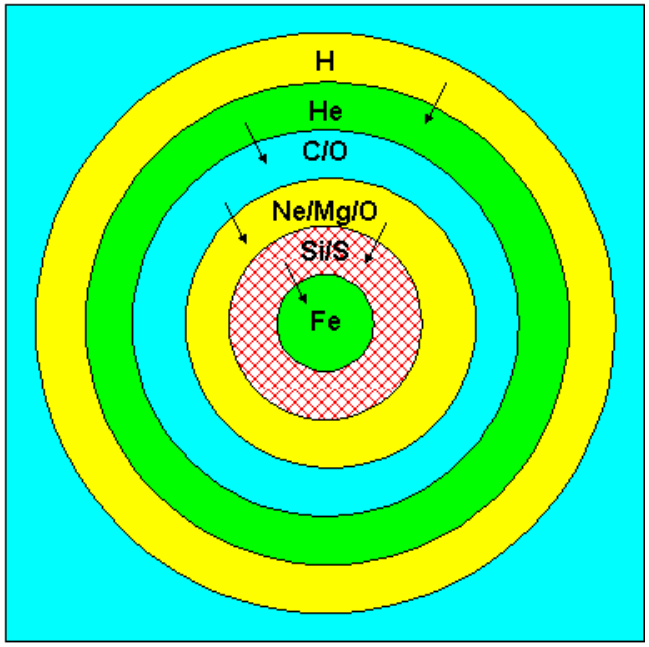

Figure 2.1: Onion-like interior structure of a star just before the onset of collapse

Before the final collapse the iron core density is $\rho \approx 4 \times 10^9\, g/cm^3$ and the radius of the star is $R \approx 500$ km.

Stars with mass in excess of 12 solar masses are thought to undergo all the stages of nuclear fusion of hydrogen, helium, carbon, neon, oxygen, silicon (see Table 2.1), until the star has the structure shown in Fig. 2.1, with an iron core surrounded by shells composed of elements with decreasing atomic mass [15].

The iron formed in the core of the star will cause the final collapse of the star, when the pressure of the degenerate electrons gas can no longer sustain the gravitational pressure. This happens when the core has reached the so-called Chandrasekhar mass limit of about 1.4 solar masses, when the core contracts and the increased temperature causes photodissociation of iron through the process [15]

$$\gamma +^{56} \mathrm{Fe} \rightarrow 13\alpha + 4n \tag{2.6}$$

This reaction absorbs about 124 MeV of energy and reduces the kinetic energy

	$1M_\odot$			$25M_\odot$		
phase	T_c (keV)	ρ_c (g/cm^3)	Δt (yr)	T_c (keV)	ρ_c (g/cm^3)	Δt (yr)
H burning	1.3	153	1.1×10^{10}	3.3	3.8	6.7×10^6
He burning	11	2.0×10^4	1.1×10^8	17	762	8.4×10^5
C burning				72	1.3×10^5	522
Ne burning				135	4.0×10^6	0.89
O burning				180	3.6×10^6	0.40
Si burning				314	3.0×10^7	2.0×10^{-3}

Table 2.1: Central temperature T_c, central density ρ_c and time scale Δt of the evolutionary phases of stars with initial masses $1M_\odot$ and $25M_\odot$ (values taken from Ref. [15]).

and pressure of electrons [15]. As the iron core starts to collapse, the density and temperature increase and a new process begins: the electron capture inside the iron core:

$$e^- + Fe \rightarrow Co + \nu_e \tag{2.7}$$

or at the nuclear level,

$$e^- + p \rightarrow n + \nu_e \tag{2.8}$$

This process produces a sudden decrease in the pressure of the electrons.

Anti-electron neutrinos are produced via the URCA process:

$$n + e^+ \rightarrow p + \overline{\nu_e} \tag{2.9}$$

At the onset of the collapse, when the density of the iron core is not too high, the electron neutrinos produced by electron capture leave the core carrying away most of the kinetic energy of the capture electrons. At this moment the pressure of the degenerate relativistic electrons can no longer sustain the weight of the core any more and collapse of the iron core commences forming a neutron star [15].

2.2 Time Profile of Neutrino Burst

Core collapse supernovae occur when the iron core of a massive star collapses due to the force of gravity. Once the density in the core exceeds that of nuclear matter, the core rebounds generating pressure waves that propagate outward. At the sonic point, i.e. the point at which the velocity of the infalling material exceeds the velocity of sound in the stellar matter, the pressure wave becomes a shock wave that propagates toward the surface of the iron core. As the shock wave propagates outward through the outer iron core, which is still collapsing, its energy is dissipated by the photodissociation of nuclei into protons and neutrons. Thus, the material behind the shock wave is mainly composed of free nucleons. Free protons have a high electron capture rate, leading to the transformation of most protons in neutrons, with the huge production of electron neutrinos (see equation 2.8). These neutrinos pile up behind the shock, which is dense and opaque to them, until the shock reaches a zone where the density has fallen to about $10^{11}\,gcm^{-3}$ ("shock breakout") and the electron neutrinos behind the shock are released in a few milliseconds. This neutrino emission is usually called the "prompt electron neutrino burst" or "neutronization burst", to be distinguished from the thermal production of all neutrino flavors [15].

The energy lost by photodissociation of nuclei and neutrino emission weakens the shock. In the so-called "prompt" supernova explosion scenario, the shock, although somewhat weakened, is able to expel the envelope of the star generating the supernova explosion on a time scale of the order of 100 ms. If the star weighs more than about 10 solar masses, the shock is weakened and stalls about 100 ms after bounce, at a radius of about 200-300 km, with insufficient energy to reach the outer layers of the star. It is widely believed that in order to obtain a supernova explosion if the shock stalls, the shock must be revived by some mechanism that is able to renew its energy. The mechanism which is currently thought to be able to revive the shock is the energy deposition by the huge neutrino flux produced thermally in the proto-neutron star [15].

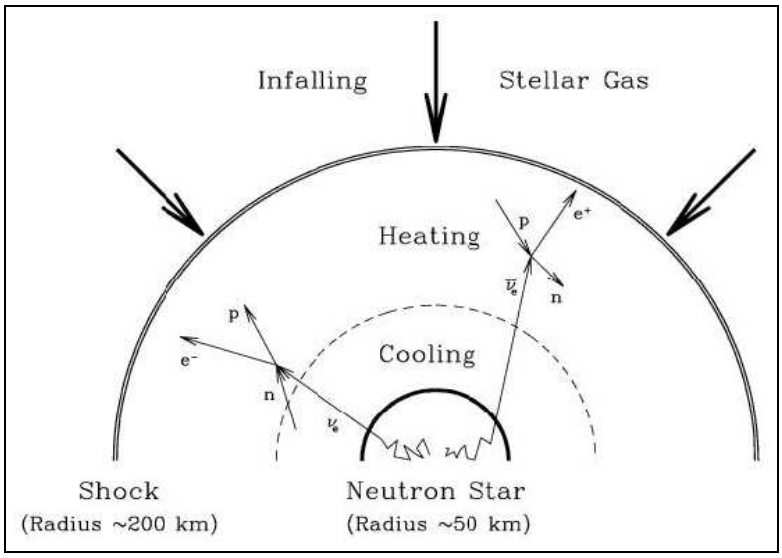

Figure 2.2: *Competing processes that determine the destiny of the supernova shock: Gas infall from the collapsing star damps shock expansion. The gas between the neutron star and the shock is cooled and heated by neutrinos. Only when the neutrino heating is strong enough, an explosion can be triggered.*

Although the neutrinos interact only very weakly with the stellar gas around the neutron star, they can deposit enough energy within the innermost few hundred kilometres to power the explosion of the star. The involved complex processes are not properly understood. Contemporary approaches to the reheating mechanism are based on the idea that neutrinos produced in the core transfer gravitational energy released by core collapse to the cooler outer regions of the star. During the reheating process, core electron neutrinos and antineutrinos radiate from their respective neutrinospheres (the sphere within the core of the star defined by the radius where the stellar material becomes optically thin to neutrinos), and a fraction of these neutrinos are absorbed by the material immediately behind the shock, thereby adding energy to the shock.

Neutrinos of all flavors are produced in the hot core of the proto-neutron star, which has a temperature of about 40 MeV [15], through electron-positron pair annihilation,

$$e^+ + e^- \rightarrow \nu_x + \overline{\nu_x} \tag{2.10}$$

electron-nucleon bremsstrahlung,

$$e^\pm + N \rightarrow e^\pm + N + \nu_x + \overline{\nu_x} \tag{2.11}$$

nucleon-nucleon bremsstrahlung,

$$N + N \rightarrow N + N + \nu_x + \overline{\nu_x} \tag{2.12}$$

and photoannihilation

$$\gamma + e^\pm \rightarrow e^\pm + \nu_x + \overline{\nu_x} \tag{2.13}$$

These neutrinos are emitted with a broad time distributions of a few seconds.

Models differ in detail and are still the subject of theoretical study. However the basic mechanism of stellar collapse and supernova explosions has been reviewed and summarised by Raffelt [18] and the generic form of the neutrino burst is generally agreed to be as illustrated in figure 2.3 which shows luminosity versus time for the three neutrino flavours and their antiparticles.

The mean energies of the resulting neutrinos are shown in Table 1.2. The neutrinos will be trapped inside the 'neutrino sphere' due to the high core density. The electron neutrinos which undergo both charged-current and neutral-current reactions and are therefore trapped further from the core. However the neutrinos can escape due to the increasing pressure gradient.

The surface temperature of the resulting 'neutrino sphere' decreases with the distance from the core and the electron neutrinos emerge at lower energies than those of the muon and tau neutrinos. The 19 neutrino events recorded in the IMB [19] and Kamiokande [20] detectors from supernova SN1987A confirmed that ~70% of the neutrinos are released in the first 2 seconds.

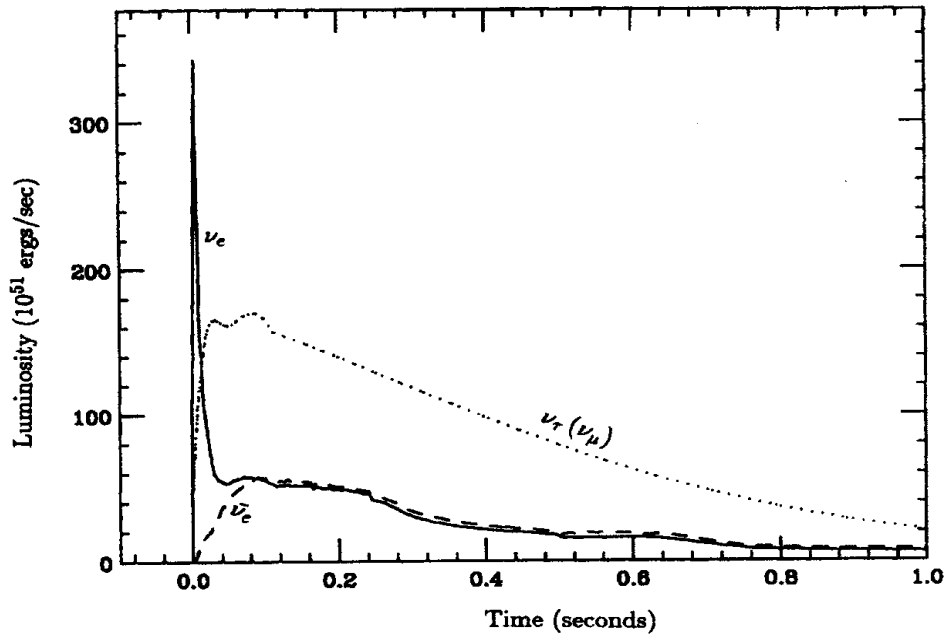

Figure 2.3: Expected neutrino luminosity as a function of time for a Type II Supernova event [16]

The emission time profile shown in figure 2.3 provides a unique opportunity to discover neutrino properties which are difficult or impossible to determine using terrestrial neutrino sources. The existence of a 'cosmological significant' mass (eg 10 - 100 eV) for one flavour (such as ν_τ) would produce an observable time-of-flight delay in the arrival time profile of that flavour, relative to the arrival time profile of the lower mass flavours. If ν_τ has a larger mass compared to the others, its arrival time will be delayed by:

$$\Delta t(s) = 0.5 \left(\frac{R}{10kpc}\right) \left(\frac{m(\nu_\tau)}{20eV/c^2}\right)^2 \left(\frac{20MeV}{E(\nu_\tau)}\right)^2 \tag{2.14}$$

For masses greater than $\sim$ 20eV this would be directly observable as a delayed component of the time profile in figure 2.3, allowing direct time-of-flight measurement of the mass of at least one neutrino type. The range of $\sim$ 2-20 kpc for Galactic supernovae is ideal for time-of-flight measurements of the neutrino mass. Therefore,

information on the profile shape of all three neutrino types would be of considerable astrophysical interest, providing the first direct observation of a 'cosmologically significant' neutrino mass, for which it would form a major component of the mass of the matter in the universe and could be a candidate for the Galactic dark matter.

2.3 Galactic Supernova Types and Rates

For historical reasons, supernovae are divided in the four different types listed in Table 2.2, characterised by their spectroscopic characteristics near maximum luminosity, which depend on the composition of the envelope of the supernova progenitor star. The two wide categories called Type I and Type II are characterised by the absence or presence of hydrogen. However, the most important physical characteristic is the mechanism that generates the supernova, that distinguishes supernovae of Type Ia from supernovae of Type Ib, Ic and II, as shown in Table 2.2. This difference becomes noticeable from the electromagnetic spectrum some months after maximum luminosity, when the innermost regions become visible. From the point of view of neutrino physics, Type Ib, Ic and II are much more interesting than Type Ia supernovae, because they produce a huge flux of neutrinos of all types [15].

	near maximum			months later			
Type	H	He	Si	Fe	O and C	Mechanism	Remnant
Ia	No	No	Yes	Yes	No	Mass Accretion	None Star
Ib	No	Yes	No	No	Yes	Core Collapse	Neutron Star
Ic	No	No	No	No	Yes	Core Collapse	Neutron Star
II	Yes	?	?	No	Yes	Core Collapse	Neutron Star

Table 2.2: Main characteristics of supernova types [15]

The majority of optically visible recorded supernovae lie within 4-5 kpc of the sun; those at larger distances (in the Galactic plane) being obscured by intervening dust. This observable region contains 5-6% of the relevant Galactic star population (see Fig. 2.4), so that the total supernova rate should be $\sim$ 16-20 times the rate recorded

optically. It should be mentioned that some people [9] argue that our region of the Galaxy may be favoured for supernovae production and therefore a simple scaling is incorrect. No plausible reasons are given for this point of view.

Although 200 supernova remnants have been recorded in our Galaxy, only the last two millennia provide a sufficiently complete record to estimate the rate [10]. Adding to those listed in [10] the recently-discovered remnant dated 1320 [11], there are 8 ± 1 type II/Ib supernovae recorded in 2200 years in the local 5-6% sample of our Galaxy (figure 2.4). This indicates a most probable total rate of 6-8 per century, within our Galaxy.

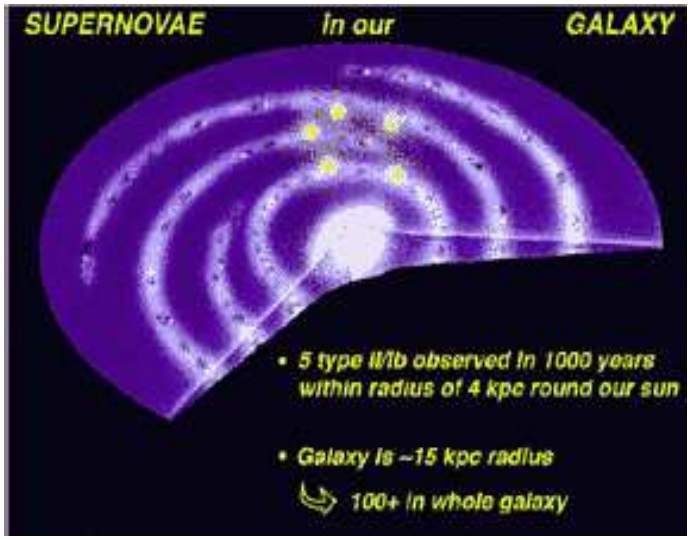

Figure 2.4: Supernovae Rate in our Galaxy [17]

However, reviews of rate estimates based on a variety of astrophysical methods [13, 14] show that these can range from 3-10 per century, consistent with the historical record [17].

2.4 The Detection Concept

The recently proposed neutrino observatory would provide a means to study, in detail, the neutrino emissions of the supernovae explosions throughout the Galaxy. Data from such a facility would result in major advances in the understanding of both the astrophysical mechanism causing supernovae, and fundamental neutrino physics. This new proposal is based on the detection of neutrons emitted following supernova neutrino induced excitation of nuclei in any target via neutral current interactions, which would allow the observation of all three neutrino flavours and hence provide tight mass limits for neutrinos to be determined. Presented here are details of a prototype neutron detector which is under study at Manchester University. Tests have been performed to determine whether the proposed design satisfies the special requirements of the new observatory.

OMNIS is a proposed project which is designed to detect neutrinos from supernovae and to determine their masses and the presence of oscillations between different flavours. High Z (lead and iron) targets are primarily sensitive to the high energy component of the supernova neutrino flux. The neutrino detection mechanism is based on the observation of neutrons emitted from the following neutral current (NC) reaction

$$\nu_x +^{A}_{Z} \mathrm{X} \rightarrow^{A-1}_{Z} \mathrm{X} + n + \nu_x \tag{2.15}$$

for all neutrino flavours emitted by supernova.

In addition, neutrons can arise from charged current (CC) neutrino interactions

$$\nu_e +^{A}_{Z} \mathrm{X} \rightarrow^{A-1}_{Z+1} \mathrm{Y} + e^- + n \tag{2.16}$$

$$\nu_e +^{A}_{Z} \mathrm{X} \rightarrow^{A-2}_{Z+1} \mathrm{Y} + e^- + 2n \tag{2.17}$$

The cross section for these processes increases with neutrino energy; therefore the neutrino flavours detected are expected to be mostly muon and tau (which are emitted with higher temperatures, hence energies, than electron type neutrinos). The energy dependence of the flux averaged cross section is given by [32]:

$$\sigma_{FD}(T_\nu) = \frac{\sigma_0 \int_0^\infty F_\nu(E_\nu) dE_\nu \int_0^{E_\nu} dE'_\nu E'^2_\nu \beta(E_\nu - E'_\nu)}{\int_0^\infty F_\nu(E_\nu) dE_\nu} \tag{2.18}$$

where $F_\nu(E_\nu)$ is the neutrino flux at energy E_ν, $\sigma_0 = 2.583 \times 10^{-44} cm^2 MeV^{-2}$, E_ν and $E_\nu^{'}$ are the incident and scattered neutrino energies, respectively, and $\beta(E_\nu - E_{\nu'})$ is the weak nuclear strength function.

By itself, the observation of a neutron in OMNIS provides no information on the type of neutrino initiating the reaction. The use of multiple nuclear targets with different sensitivies to ν_e and neutral current reactions would enhance flavour sensitivity.
Lead is a particularly efficient converter of neutrinos to neutrons, as its threshold for neutron emission via neutral current interactions is 7.37 MeV [50].

Iron has a higher threshold of 11.20 MeV [50] for neutron emission processes. This will result in a lower efficiency, but all the events will be virtually coming from ν_μ's, ν_τ's and their antiparticles.
The threshold for double neutron events from charged current processes in iron targets is sufficiently high that such production will be negligible.

The charged current processes in lead targets have a threshold of 14.98 MeV [50]. These processes are extremely dependent on the energy of the $\nu_e^{'}s$ and $\overline{\nu}_e^{'}s$. The conversion of ν_μ and ν_τ to ν_e would produce much more energetic $\nu_e^{'}s$ than would be expected from the supernova. The maximal mixing increases the number of neutron events by a factor of four, while the rate of double neutron events is enhanced by a factor of 40 [31]. Thus a clear signature of oscillations of this type would be provided by the ratio of one- to two-neutron events from lead.

The proposed neutron detection process involves the possible use of gadolinium which has the largest thermal neutron capture cross section of all practical nuclei. The neutron capture on Gd is usually followed by the emission on average of 3-4 gammas. The mean value of the total energy of these gammas is $\sim$ 8 MeV (8 MeV being the mean value of the neutron binding energy of the Gd isotopes plus the energy of the captured neutron).
The theory of neutron and gamma interactions inside the detector and the detection mechanism are described in chapter 3.

2.5 OMNIS in Conjunction with Other Experiments

A number of existing world detectors are sensitive to supernova neutrinos, in particular Super-Kamiokande, Macro, LVD and SNO. However, the existing neutrino detectors are predominantly charged current based and therefore insensitive to ν_μ's and ν_τ's or the flavour of the incident neutrino [33]. OMNIS would provide a large signal for ν_μ's and ν_τ's (see figure 2.5) complementing in this way the sensitivity of the existing detectors to ν_e's.

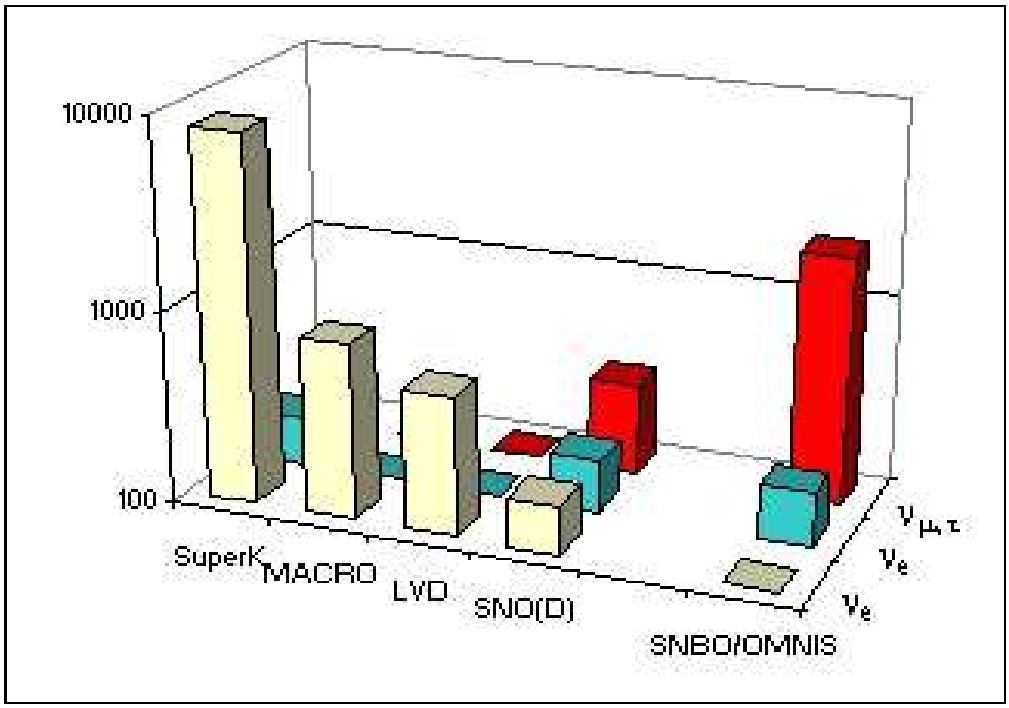

Figure 2.5: Comparison of detected neutrino events from OMNIS and other major world detectors from an 8 kpc supernova (4000 tons of Pb and Fe targets assumed for the OMNIS detector)

The measurements made by Kamiokande and IMB at the time of SN1987A were considered to provide a limit on the $\overline{\nu_e}$ mass. The analyses were limited by the small number of detected neutrino events and by uncertainties in modeling the supernova

mechanism and associated neutrino emission [31]. Even though these uncertainties will affect the time-of-flight neutrino mass limits derived from neutrino detector, OMNIS has two important advantages. First, the large number of events from a Galactic supernova (see Fig. 2.5) will provide a detailed time history of neutrino emission associated with the supernova. Second, complementary information from others detectors, such as Super-Kamiokande, will reduce the degree to which analyses must depend on poorly understood aspects of supernova models [31].

Chapter 3

Theory of Neutron and Gamma Interactions

3.1 Neutron Detection Process

Since neutrons are uncharged they can be detected either by scattering from charged or uncharged particles and recording the recoils, or by generating nuclear reactions whose products are detected. Since the cross section for neutron interactions in most materials is a strong function of neutron energy, the neutrons can be classified according to their energy:

Type	Neutron Energy
Cold neutrons	$\leq$ 1 meV
Slow (thermal)	$\leq$ 0.5 eV
Epi-thermal	0.5 eV - 50 keV
Thermal	0.025 eV
Fast	$\geq$ 50 keV
High energy	$\geq$ 1 MeV

Table 3.1: Regimes of Neutron Energies

In order to design a suitable neutron detector it is necessary to have a proper understanding of the neutron thermalization process, since the methods used in neutron detection are dependent on the energy of the neutrons. Neutron detection in OMNIS is based on two processes :

- Neutron capture on protons inside organic scintillation detectors, which is followed by the emission of a single 2.2 MeV gamma ray. The cross section of thermal neutron capture on hydrogen is $\sigma = 0.33$ barns.
- Neutron capture on Gd, which is followed by the emission on average of 3-4 gammas with a summed energy of ~ 8 MeV i.e. the neutron binding energy of the formed Gd isotope. The cross section for thermal neutron capture on natural gadolinium is $\sigma = 49,700$ barns (see Section 3.1.2).

In both processes the neutron capture cross section dependence on the neutron velocity is described by the "$1/v$ law", so the smaller the neutron velocity v is, the higher the capture cross section. If the neutron energy is high, a moderator is required to thermalize the neutrons.

The neutron thermalization process depends on the elastic scattering of the neutrons on light nuclei.
In such collisions the incident neutron transfers a fraction of its kinetic energy to the scattering nucleus. This process can be used for the detection of fast neutrons. The elastic scattering gives rise to a *recoil nucleus* (see Fig. 3.1) which can be detected directly for neutrons with energies above the keV range.
Elementary application of the laws of conservation of energy and momentum for an elastic collision between a neutron with initial energy E and a target nucleus of mass A initially at rest gives the ratio between the scattered neutron energy $E^{'}$ and the initial energy:

$$\frac{E'}{E} = \frac{A^2 + 1 + 2Acos\theta}{(A+1)^2} \tag{3.1}$$

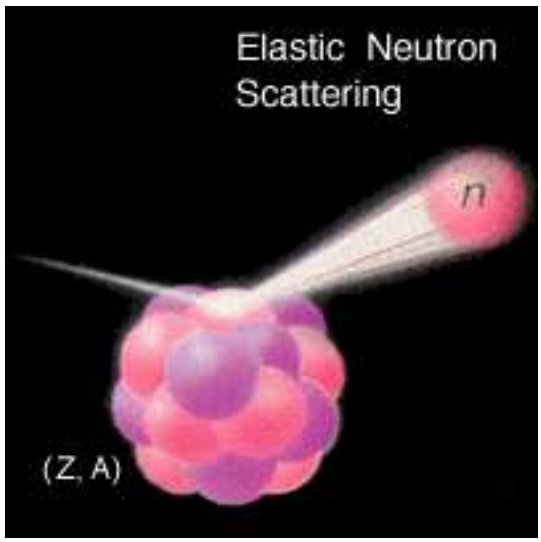

Figure 3.1: Elastic Neutron Scattering [37]

where θ is the scattering angle in the centre-of-mass system. The energies E and $E^{'}$ are the energies measured in the laboratory system. For no scattering ($\theta = 0$), Equation 3.1 gives $E^{'}/E = 1$, as it should. The maximum energy loss occurs for a head-on collision ($\theta = 180°$):

$$\left(\frac{E'}{E}\right)_{min} = \left(\frac{A-1}{A+1}\right)^2 \tag{3.2}$$

For scattering on hydrogen (A = 1), the neutron can give all its energy to the struck proton in one collision. Therefore hydrogenous materials are chosen for neutron thermalization. For the prototype neutron detector tested at Manchester University, paraffin wax ($C_{25}H_{52}$) or light water (H_2O) were chosen as possible neutron moderators to thermalize the neutrons emitted by a source. The experiment is described in chapter 4.

For neutron energies $\leq$ 10 MeV the scattering is mostly s wave and thus (in the centre-of-mass system) independent of θ [51]. The values of $E^{'}/E$ are uniformly distributed between $E^{'}/E = 1$ and the minimum value given by Equation 3.2.

3.1.1 Neutron Thermalization Process

The analysis of the neutron thermalization is based on the random walk process. For one neutron travelling inside a moderator, the probability density $\rho(r)$ for the neutron to travel a distance r before interacting is given by :

$$\rho(r)\,dr \;=\; \frac{1}{\lambda}\,e^{-\frac{r}{\lambda}}\,dr, \quad for\ 0 \leq r < \infty; \tag{3.3}$$

where λ is the mean free path between two collisions (mean distance between two successive collisions).

The mean squared distance travelled between two collisions is given by:

$$< r^2 > = \int_0^\infty \rho(r)\,r^2\,dr \;=\; 2\,\lambda^2 \tag{3.4}$$

If the neutron is created at $x = y = z = t = 0$ and it suffers isotropic collisions with the mean free path λ, then after n collisions its spatial coordinates will be

$$x_n \;=\; \sum_{i=0}^{n} \Delta x_i \tag{3.5}$$

$$y_n \;=\; \sum_{i=0}^{n} \Delta y_i \tag{3.6}$$

$$z_n \;=\; \sum_{i=0}^{n} \Delta z_i \tag{3.7}$$

Since the collisions are isotropic, Δx_i, Δy_i and Δz_i are positive or negative with equal probabilities, and therefore the mean coordinate values after n collisions are:

$$< x_n > = < y_n > = < z_n > = \;0 \tag{3.8}$$

From equation 3.4 it follows that the mean distance travelled between two collisions is

$$2\,\lambda^2 \;= < \Delta x^2 \;+\; \Delta y^2 \;+\; \Delta z^2 > \tag{3.9}$$

The collisions are isotropic so the problem has spherical symmetry. Therefore after n collisions the probability density to find the neutron at position x is given by:

$$\rho(n,x) \;=\; \alpha(n)\, e^{-\beta(n)\, x^2}, \quad -\infty < x < \infty; \tag{3.10}$$

where $\alpha(n)$ and $\beta(n)$ are two variables which have to be determined using the value of the mean squared distance travelled along x axis after n collisions i.e.:

$$< x_n^2 > = \int_{-\infty}^{\infty} x^2\, \rho(n,x)\, dx \;=\; \frac{2\,n}{3}\,\lambda^2 \tag{3.11}$$

and the normalization condition:

$$\int_{-\infty}^{\infty} \rho(n,x)\, dx \;=\; 1 \tag{3.12}$$

The values of the coefficients α and β can be determined by substituting $\rho(n,x)$ (equation 3.10) into equations (3.11-3.12):

$$\rho(n,x) \;=\; \frac{1}{\lambda\,(\frac{4\pi}{3}\,n)^{\frac{1}{2}}}\, e^{-\frac{3\,x^2}{4\,n\,\lambda^2}}, \quad -\infty < x < \infty; \tag{3.13}$$

The probability density to find the neutron at a distance r after n collisions is given by the product:

$$\rho(n,r) \;=\; \rho(n,x)\,\rho(n,y)\,\rho(n,z) \tag{3.14}$$

and because the collisions are isotropic it can be obtained:

$$\rho(n,r) \;=\; \frac{1}{\lambda^3\,(\frac{4\pi}{3}\,n)^{\frac{3}{2}}}\, e^{-\frac{3\,r^2}{4\,n\,\lambda^2}}, \quad 0 < r < \infty; \tag{3.15}$$

Introduce the parameter ξ, defined as the ratio between the neutron energy decrease following each collision ΔE and the neutron energy E before the collision:

$$\xi \;=\; \frac{\Delta E}{E} \;=\; \Delta(lnE) \tag{3.16}$$

Hence if after each collision the relative energy decrease is $\Delta(lnE)$, the number of collisions required to decrease the neutron energy from E_0 to E is:

$$n = \frac{1}{\xi} \ln \frac{E_0}{E} \tag{3.17}$$

The spatial distribution becomes:

$$\rho(E,r) = \frac{1}{\lambda^3 \left(\frac{4\pi}{3} \frac{1}{\xi} \ln \frac{E_0}{E}\right)^{\frac{3}{2}}} e^{-\frac{3\,r^2}{4\,\frac{\lambda^2}{\xi} \ln \frac{E_0}{E}}}, \quad 0 < r < \infty; \tag{3.18}$$

The values of the ξ parameter for different neutron moderators are given in [47]. Its value in light water is $\xi = 0.92$.

For paraffin wax ξ can be calculated as in the case of a composition of several isotopes using [48]:

$$\overline{\xi}(E) = \frac{\sum_j \xi_j \Sigma_s^j(E)}{\Sigma_s(E)} \tag{3.19}$$

where $\Sigma_s^j(E)$ and $\Sigma_s(E)$ have the same energy dependence, and therefore $\overline{\xi}(E)$ is a constant.

The values of ξ and λ which were used to calculate the probability density (Equation 3.18) are given in the following table:

The ξ parameter		The mean free path	
paraffin wax	light water	paraffin wax	light water
0.92	0.92	17.8 mm	22 mm

Table 3.2: Values used to calculate the probability to thermalize the neutrons

Therefore approximately 19 collisions are required to thermalize a 1 MeV neutron in paraffin wax or light water.

3.1.2 Principle of Neutron Detection

Once the neutrons are thermalized, there will be a high probability for them to be captured on the Gd or H nuclei causing a nuclear reaction in which secondary radiation (gamma rays) will be emitted and detected.

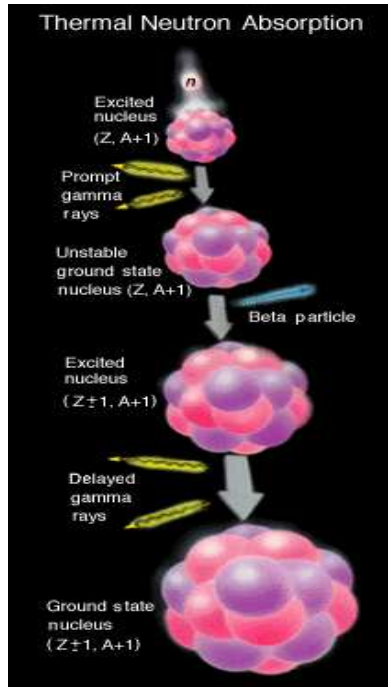

Figure 3.2: Thermal Neutron Capture [37]

The relative isotopic abundances of the natural Gd isotopes and the thermal neutron capture cross-sections for each isotope are given in Table 3.3.

The Gd isotopes have different cross-sections for the capture of thermal neutrons. The most efficient is $^{157}_{64}$Gd which has a cross-section for thermal neutron capture $\sigma = 259,000$ barns, followed by $^{155}_{64}$Gd which has $\sigma = 61,100$ barns. The other Gd isotopes have low cross-sections and may be neglected when the absorption of thermal neutrons on natural Gd is considered. Natural Gd can be used with a cross-section for the (n, γ) reaction being still large $\sigma = 49,700$ barns.
Due to their relative short half-life, the $^{153}_{64}$Gd and $^{159}_{64}$Gd isotopes are not present in natural Gadolinium. The ^{153}Gd isotope has a half-life of 241.6 days, undergoing an EC decay mode to ^{153}Eu, while the ^{159}Gd has a half-life of 18.6 hours undergoing a

Isotope	% Abundance	Thermal n capture cross-section (barns)
^{152}Gd	0.20	735
^{154}Gd	2.18	85
^{155}Gd	14.80	61100
^{156}Gd	20.47	1.5
^{157}Gd	15.65	259000
^{158}Gd	24.84	2.2
^{160}Gd	21.86	0.77

Table 3.3: Relative Isotopic Abundances of the Natural Gd [38]

β^- decay to ^{159}Tb.

The absorption of thermal neutrons is described as follows

$$^{155(157)}\mathrm{Gd} + n \rightarrow \mathrm{Gd}^* \rightarrow^{156(158)} \mathrm{Gd} + \gamma^{'}s \tag{3.20}$$

where Gd* is the excited state of a Gd nucleus.

When considering the dimensions of a detector the following should be observed:

- if a scintillator is used as a detector as well as a moderator, it must be large enough to thermalize the neutrons which enter it.
- the detector must be also large enough to detect the secondary radiation (gammas) produced in the neutron capture event.
- the scintillation detectors should not be so large as to increase too much the light attenuation effects. Its length will be limited by the attenuation length for scintillation photons inside the scintillator.

Once thermalized, the neutrons not captured on Gd may be captured on H inside the scintillator which will give rise to secondary radiation (2.2 MeV gammas).
The thermal neutron capture on the Gd isotopes contained in natural Gd is expected to be followed by the emission of a cascade of 3 - 4 γ's with a total energy of $\sim$ 8 MeV,

the mean Q value for these processes (see equation 3.20). A more exact consideration of the gamma signal can be made considering the Gd spectrum measured by Groshev et al. [39] in 1959 using a NaI magnetic spectrometer, shown in figure 3.3.

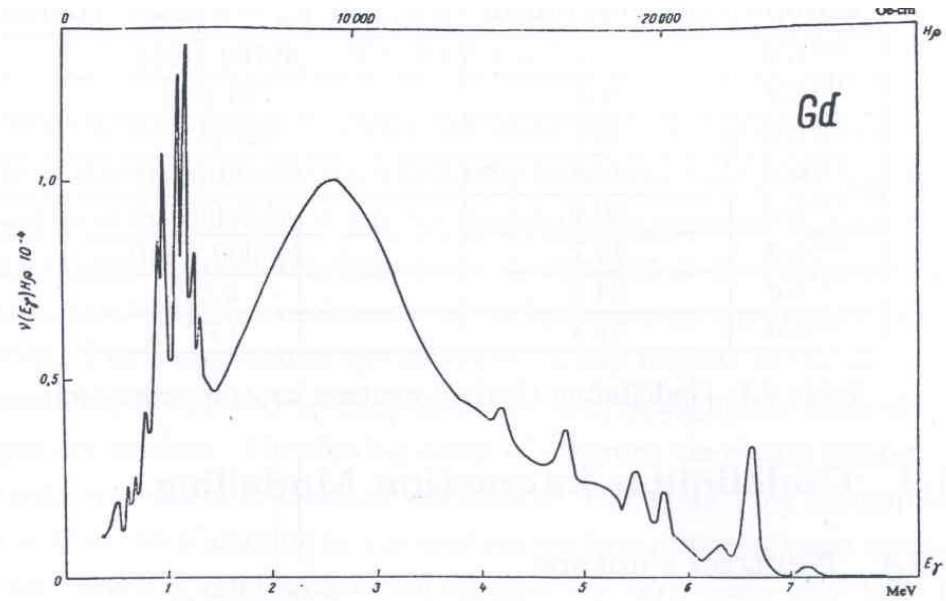

Figure 3.3: The gamma energy spectrum for natural Gd [39]

The binding energies of both significant Gd isotopes are: $B_n(^{156}\text{Gd}) = 8.53\,MeV$ and $B_n(^{158}\text{Gd}) = 7.93\,MeV$. Figure 3.4 shows the energy levels below the neutron binding energy for both Gd isotopes.

The transition from the capture state to the ground state are labelled with different numbers from 1 to 6 to distinguish between the different energies of the gammas emitted in each transitions.

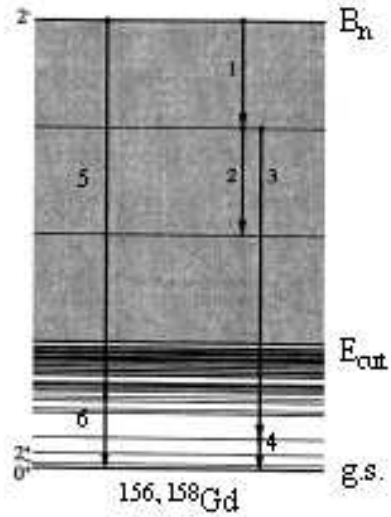

Figure 3.4: Energy levels for Gd isotopes [49]

The energy spectrum of emitted gammas from ^{nat}Gd, as measured by Groshev et al. (Fig. 3.3) can be divided into two energy ranges: a discrete range and a continuum.

- Below the energy threshold denoted E_{cut} (Fig. 3.4) are the discrete energy levels. The nucleus can de-excite from the capture state *directly* to the ground state (g.s.), in which case a gamma of energy equal to the neutron binding energy $E_\gamma \approx 8\,MeV$ is emitted.

  It can also de-excite from the capture state to one of the discrete energy levels (transition 5) emitting a gamma of energy $E_\gamma \geq 4.5\,MeV$, followed by the transition to the ground state (transition 6), emitting a gamma of energy $E_\gamma \leq 1.5\,MeV$.

  These two energy ranges will form the discrete part of the gamma energy spectrum for ^{nat}Gd (Fig. 3.3).

- Above the energy E_{cut} there is no detailed information about the energy levels. This region is the continuum range. Another possible way for the Gd nucleus to de-excite is to undergo first a transition from the capture state to one of the energy levels in the continuum range above E_{cut} (transition 1) followed by a transition to one discrete energy level (transition 3).

These gamma energies will form the continuum energy range of the measured gammas energy spectrum for ^{nat}Gd: $1.5 \leq E_\gamma(MeV) \leq 4.5$ (Fig. 3.3).

The mean value of the gamma energy in the continuum energy range of the gamma energy spectrum of ^{nat}Gd (Fig. 3.3) is $\sim$ 2.7 MeV.

Since the gammas from Gd decay are emitted in different transitions from the capture state to the ground state, they are emitted eventually isotropically.
In the detection of these gammas both the geometric and the intrinsic efficiencies of the detector have to be taken into account.
These gammas can be detected using organic plastic scintillators. A prototype detector tested at Manchester University is presented in chapter 4. The analysis of the size of scintillator needed to detect the gammas from the Gd decay following the thermal neutron capture involves the computation of the values of gamma mean free paths inside the scintillators for different gamma energies.

3.2 Gamma Interactions inside Scintillators

In order to calculate the penetration and energy deposited into the scintillators by the gammas emitted in Gd decay, two further parameters are needed:

- the attenuation coefficient of the gamma rays inside the scintillators $[\mu(cm^{-1})]$;
- the energy-absorption coefficient for the gamma rays by the scintillators $[\mu_{en}(cm^{-1})]$;

The ratios μ/ρ and μ_{en}/ρ, where $\rho\,(g/cm^3)$ is the density of the scintillator, represent the mass attenuation coefficient and the mass energy-absorption coefficient respectively.

3.2.1 The Mass Attenuation Coefficient $\mu/\rho\,(cm^2/g)$

A narrow beam of monoenergetic gammas with an initial intensity I_0 will have a final intensity I, after passing through a distance x inside the scintillator given by the following relation:

$$I = I_0\, exp[-(\frac{\mu}{\rho})\rho x] \tag{3.21}$$

The values of μ/ρ are related to the total cross-section σ_{tot} according to:

$$\frac{\mu}{\rho} = \frac{\sigma_{tot}}{uA} \tag{3.22}$$

where u is the atomic mass unit, A is the relative atomic mass of the scattering material and σ_{tot} is the total cross-section summing over all the contributions from the main photon interactions:

$$\sigma_{tot} = \sigma_{pe} + \sigma_{coh} + \sigma_{incoh} + \sigma_{pair} + \sigma_{phn} \tag{3.23}$$

where σ_{pe} is the photoelectric cross-section, $\sigma_{coh/incoh}$ are the coherent / incoherent (Compton) cross sections respectively, σ_{pair} is the pair production cross section and σ_{phn} is the photonuclear cross-section.

For mixtures and compounds the value of the mass attenuation coefficient is calculated as follows:

$$\frac{\mu}{\rho} = \sum_i w_i \left(\frac{\mu}{\rho}\right)_i \tag{3.24}$$

where w_i is the fraction by weight of the ith atomic element.

The mass attenuation coefficient gives the attenuation of the intensity, and therefore number of gammas inside the beam passing through the scintillator. The energy deposited by the gamma rays inside the scintillator can be calculated using a second coefficient, called the energy-absorption coefficient μ_{en}.

3.2.2 The Mass Energy-Absorption Coefficient $\mu_{en}/\rho\,(cm^2/g)$

The gammas may undergo a variety of different interactions inside the scintillator. The energy range for the gammas entering the scintillators is $E_\gamma \leq 8$ MeV (figure 3.3).

The energy dependence of the mass attenuation coefficient inside scintillators for gamma energies below 10 MeV is shown in Figure 3.5:

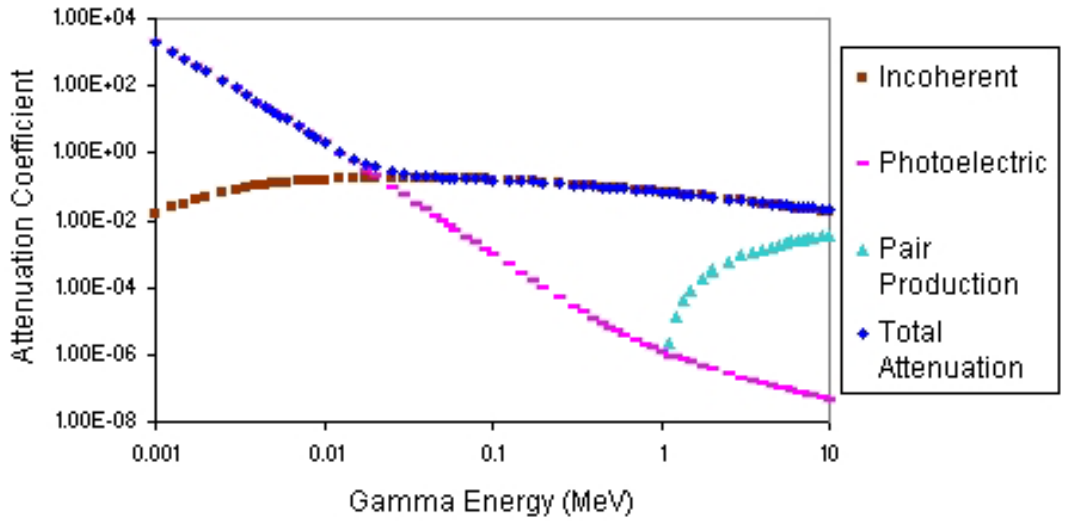

Figure 3.5: The mass attenuation coefficient μ/ρ (cm^2/g) [40]

For these gamma energies the main interactions are the photoelectric process which is the dominant interaction for $E_\gamma \leq 10$ keV (figure 3.5) and the incoherent (Compton) scattering which is the dominant interaction for 50 keV $\leq E_\gamma \leq 8$ MeV (figure 3.5).

In the incoherent (Compton) scattering process the incident gamma will scatter off the nearly free electrons inside the scintillator at some angle to their original trajectory (see Fig. 3.6):

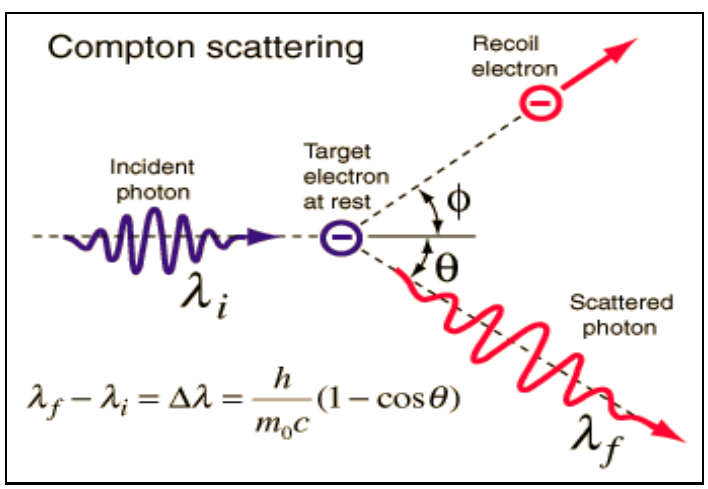

Figure 3.6: Compton scattering process [41]

The Compton effect occurs primarily in the scatter of high X-ray energy / gamma-rays and low atomic numbers. Both the scattered gamma and the electron may be deflected at an angle to the direction of the path of the incident gamma. The incident gamma having delivered part of its energy to the electron emerges at a lower energy.

The dependence of the scattered gamma's energy on the scattering angle θ is given by the Compton formula:

$$E' = \frac{E}{1 + (\frac{E}{m_e c^2})(1 - cos\theta)} \tag{3.25}$$

where E' is the scattered gamma's energy, E is its initial energy, $m_e c^2$ is the electron rest energy and θ is the scattering angle.
The angular distribution of the scattered γ-ray is described by the Klein-Nishina cross-section:

$$\frac{d\sigma}{d\Omega} = Zr_e{}^2 \left(\frac{1}{1 + \frac{h\nu}{m_e c^2}(1 - \cos\theta)} \right)^2 \left(\frac{1 + \cos^2\theta}{2} \right) \left(1 + \frac{(\frac{h\nu}{m_e c^2})^2 (1 - \cos\theta)^2}{(1 + \cos^2\theta)[1 + \alpha(1 - cos\theta)]} \right) \tag{3.26}$$

where r_e is the classical electron radius.

These possible gamma interactions result in an energy transfer from the gammas to the electrons inside the scintillator. The sum of the kinetic energies of these electrons released by the gamma interactions per unit mass is the dosimetric quantity kerma. The most natural way to define the mass energy-absorption coefficient is to introduce a third coefficient called the mass energy-transfer coefficient μ_{tr}/ρ defined from the dosimetric quantity kerma K. Kerma is an acronym for the sum of the kinetic energies of all the primary charged particles released by gammas per unit mass.

$$K = (\frac{\mu_{tr}}{\rho}) \times (\Phi E) \tag{3.27}$$

where Φ is the gamma fluence (number of gammas incident per unit area) and E is their energy.

Hence (μ_{tr}/ρ) is defined as:

$$\frac{\mu_{tr}}{\rho} = (f_{pe}\sigma_{pe} + f_{incoh}\sigma_{incoh} + f_{pair}\sigma_{pair})/uA \tag{3.28}$$

where f is a factor representing the average fraction of the gamma energy that is lost through the corresponding process (photoelectric for f_{pe}, etc). The coherent scattering has been omitted because of its negligible energy transfer associated with it.

The mass energy-transfer coefficient for homogeneous mixtures and compounds can be calculated analogously to the case of the (μ/ρ) coefficient:

$$\frac{\mu_{tr}}{\rho} = \sum_i w_i \left(\frac{\mu_{tr}}{\rho}\right)_i \tag{3.29}$$

We are interested in the total amount of energy deposited inside the scintillator by the gamma rays. The energy loss process consists of the transfer of energy by the incident gammas to the electrons inside the scintillator. The energy transferred from the gamma to the detector is given by the sum of the kinetic energies of the scattered electrons, which is just the kerma K. So the energy lost by the incident gammas can be calculated using the mass energy-transfer coefficient μ_{tr}/ρ. But this is not always the actual energy *deposited* inside the scintillator because the scattered electrons may lose part of their kinetic energy through radiative processes and this radiation may be lost.

In this way the energy deposited by the gammas inside the scintillator is only the fraction of the kinetic energy of the scattered electron which is lost in ionising processes, as these are causing the scintillations inside the detector.
This is given by the mass energy-absorption coefficient, defined as:

$$\frac{\mu_{en}}{\rho} = (1-g)\left(\frac{\mu_{tr}}{\rho}\right) \tag{3.30}$$

where g represents the fraction of the kinetic energy of the scattered electrons which is lost in radiative energy-loss processes.

The mass energy-absorption coefficients have been calculated for plastic scintillators for different gamma energies (figure 3.7).

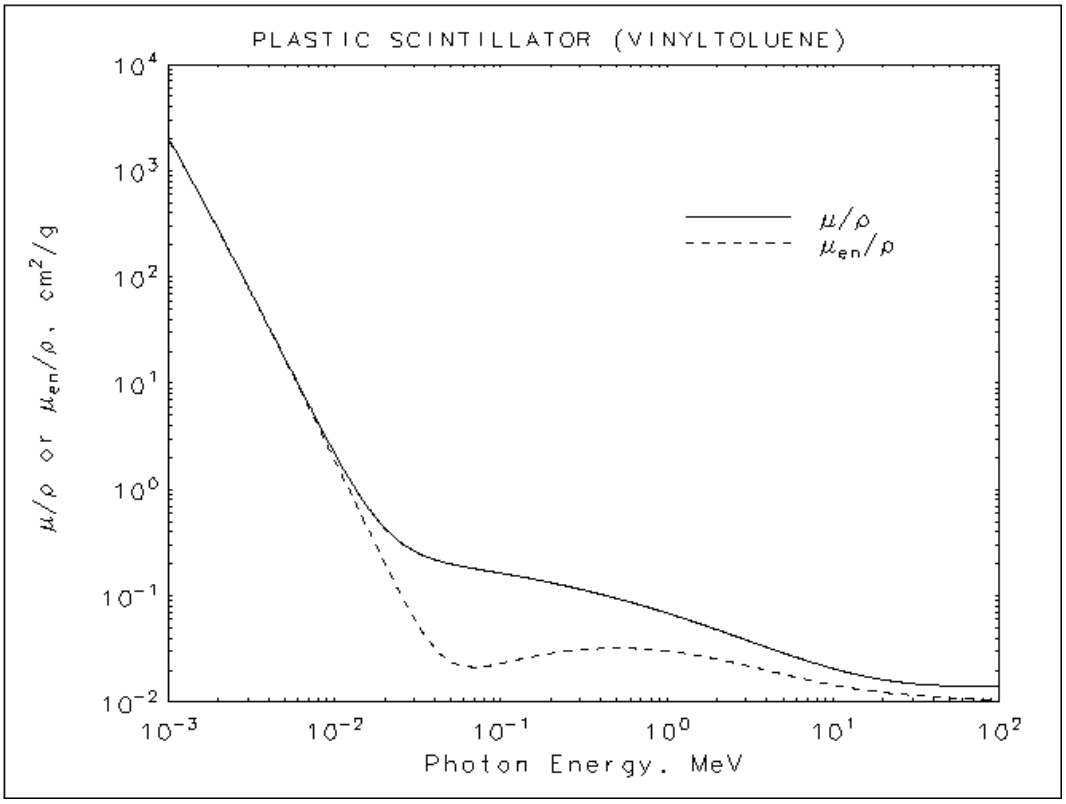

Figure 3.7: The mass attenuation and mass energy-absorption coefficients [42]

For the calibration of the detector one needs to know the energies deposited by the gamma rays inside the detector.

The deposited energies can be calculated using the mass energy-absorption coefficients. The average energy of the gamma rays after passing through a distance x inside the scintillator is given by:

$$< E > = E_0 \, exp[-(\frac{\mu_{en}}{\rho})\rho x] \tag{3.31}$$

where E_0 is the initial energy.

The values of the mass energy-absorption coefficient, μ_{en}/ρ, will be used to calculate the fraction of energy deposited by the gamma rays inside the organic plastic scin-

tillators used in this research. This information is needed for a better understanding of the energy calibration of the detector, which is performed using gamma sources of known energies in the range 0.6 - 4.4 MeV. The methods used are discussed in chapter 4.

Chapter 4

Tests of a Prototype Detector

4.1 Background Information on Operation of Scintillation Detectors

Due to their high detection efficiency scintillation detectors can be used to identify the presence of gamma rays [43].

The gamma interactions inside the scintillators result in an energy transfer to the electrons inside the scintillator. The possible gamma interactions inside the organic plastic scintillators have been described in section 3.2. An electron passing through the scintillator material will lose energy in ionisation processes, followed by the emission of visible light (scintillation photons). The detection mechanism is based on the collection of these photons by photomultiplier tubes and the efficiency of the detector depends on the fraction of photons reaching the photomultipliers that convert the light into a weak current of photoelectrons. The simplified structure of a photomultiplier is illustrated in Fig. 4.1. It consists of two major elements: a *photocathode* followed by an assembly of *dynodes*. The scintillation photon interacts within the photocathode, and it is this process which results in an ejection of a photoelectron via the photoelectric effect. An important parameter in scintillation counting is the quantum efficiency (QE) of the photocathode. The quantum efficiency is defined as:

$$QE = \frac{number\ of\ photoelectrons\ emitted}{number\ of\ incident\ photons} \tag{4.1}$$

For an ideal detector the quantum efficiency would be 100%. However practical photomultiplier tubes have typically quantum efficiencies of $\sim$ 20 - 30% [53].

Because the total electric charge produced is too small (only a few hundred photoelectrons may be involved in a typical pulse [53]), it does not provide a usable electrical signal.

The electron multiplier portion of a photomultiplier relies on the emission of secondary electrons as the electrons from the photocatode are accelerated and focussed to strike the surface of an electrode, called a *dynode*. The energy deposited by the incident photoelectron inside a dynode results in the emission of secondary electrons from that dynode surface.

The secondary electron yield from a dynode depends on the incident electron energy. A positive voltage of several hundred volts is applied to the first dynode, which will determine almost entirely the kinetic energy of the electrons on arrival at the first dynode, because this electrons leave the photocathode with a kinetic energy on the order of 1 eV or less [54].

The secondary electrons produced are then accelerated and focussed to further dynodes producing an avalanche of secondary electrons at the anode of the photomultiplier tube.

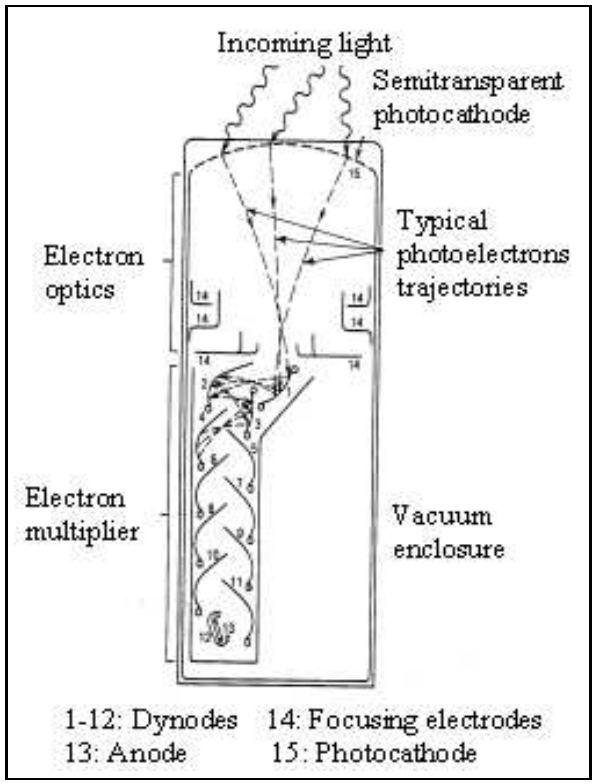

Figure 4.1: Schematic of a photomultiplier tube with succession of dynodes [44]

The overall multiplication factor δ for a single dynode is defined as:

$$\delta = \frac{number\ of\ secondary\ electrons\ emitted}{primary\ incident\ electron} \tag{4.2}$$

For interdynode voltages of a few hundred volts the overall multiplication factor is of order 4 - 6 per dynode [54]. First the electrons emitted from the photocathode strike the first dynode and produce δ electrons for each incident photoelectron, which again will have very low energies, typically a few eV [55]. The electrostatic field established between the first and the second dynode will guide these secondary electrons, which will strike the second dynode. Secondary electrons from each dynode are accelerated toward the following dynode, such that N stages in the multiplier section will provide an overall gain:

$$overall\ gain = \alpha\delta^N \tag{4.3}$$

where α is the fraction of photoelectrons collected by the multiplier structure. For well designed tubes $\alpha \approx 1$ and conventional dynodes are characterised by a typical value $\delta = 5$, which gives an overall tube gain of 5^{10}, i.e. about 10^7 [55].

The overall gain of a photomultiplier is a sensitive function of applied voltage V, being typically proportional to [55]:

$$overall\ gain \sim V^6\ to\ V^9 \tag{4.4}$$

This means that a small change in V will produce a large change in gain. Therefore voltage stability is crucial.

The electrons are collected at the anode, creating a pulse with an amplitude linearly related to the number of photoelectrons and consequently to the intensity of the scintillation light. The pulse is then analyzed by an electronic system as shown in Figure 4.2:

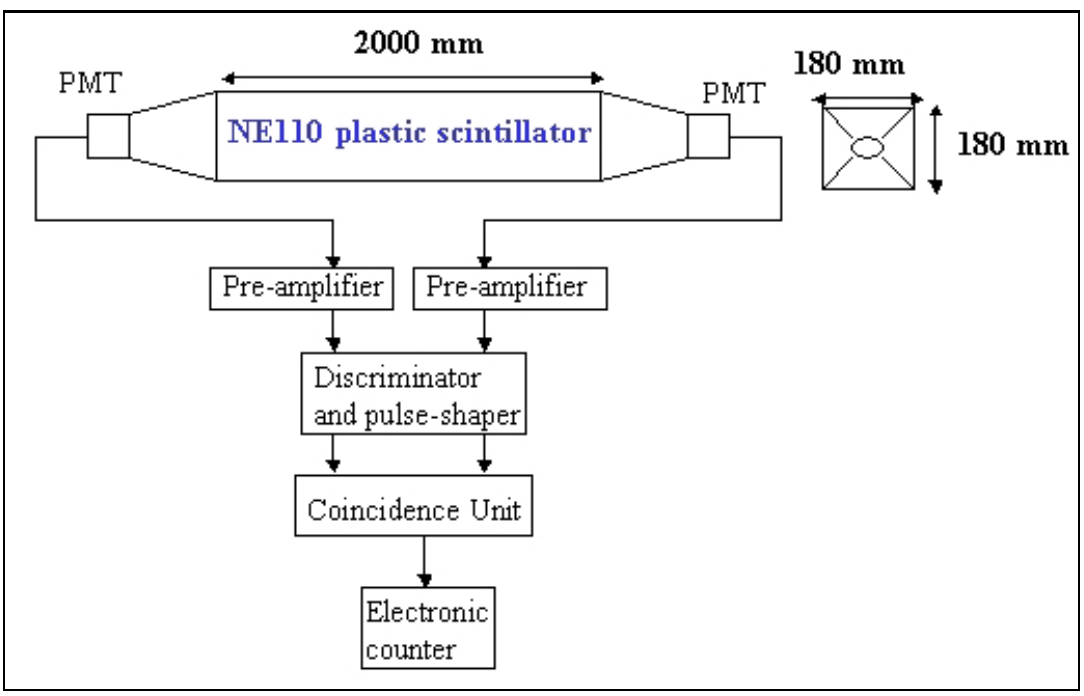

Figure 4.2: Schematic diagram of a scintillation detector

Several NE110 organic plastic scintillators were used and tested in this experiment (see Fig. 4.2) to see if they can be used for neutron detection in the OMNIS project. The neutron detection mechanism involves the use of Gd, due to the extremely high capture cross-section for thermal neutrons [56]. The neutron capture events must then be converted into a signal, and distinguished from background, and this will require relatively long time measurements (up to 50,000 seconds) of the gamma energy spectrum which is emitted following these events, in order to improve the statistics of the measurement. Therefore, it is very important to establish conditions under which the drifts in the voltage would have minimal influence on the measured counts.

The detectors were tested using both gamma sources of known enrgies and the background radiation. The number of scintillation photons produced in the detection process and hence the charge pulse from the photomultiplier tubes (PMT's) is proportional to the energy deposited.
The preamplifier converts the charge pulse from the PMT to a voltage pulse. If the voltage pulse is above the chosen threshold, it is then converted by the discriminator into a fast logic pulse, with a pulse width set to 20 ns. The coincidence unit will produce a logic output pulse if two input pulses occur within a time interval less than 40 ns.

When radiation detectors are operated in pulse mode, the signal pulses must exceed a given level H_d, called the discriminator level (threshold), in order to be registered by the counting circuit.
An operating point must be established that will provide maximum stability over long periods of time, because the gain of the photomultiplier is a sensitive function of the applied voltage (see Equation 4.4).
The region of minimum slope on the count rate as a function of voltage is called counting plateau and represents the region of operation in which the minimum sensitivity to drifts in voltage is achieved. Figure 4.3 shows a typical plot of the coincidence rate due to cosmic ray muons, measured as a function of voltage.

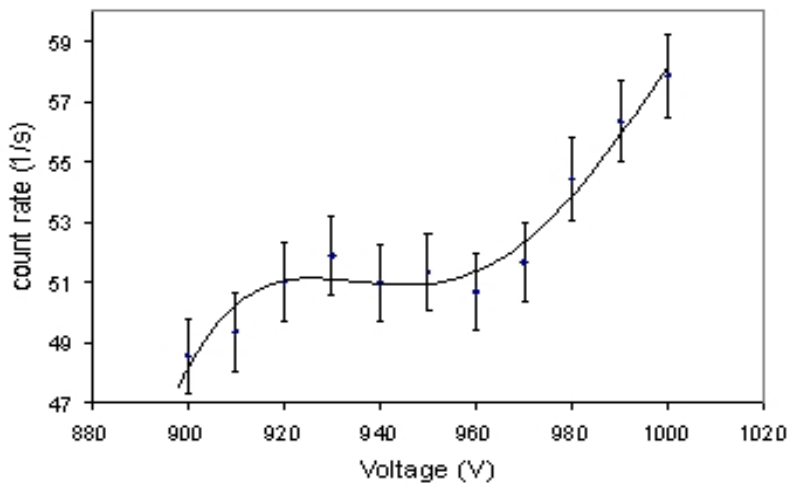

Figure 4.3: Coincidence Counting Rate as a function of PMT Voltage

A plateau region was found to be between 920 and 960V. Voltages in this range were applied to the PMT's in all measurements.

The neutron detection involves the measurement of the energy spectrum of the gammas emitted following the neutron capture on Gd. The response of the detector to gamma rays is analysed in Section 4.2.

4.2 The Detector Gamma Response

In order to test the linearity of the multichannel analyser (MCA), and to detect the gammas emitted in the neutron capture reactions, the following experimental arrangement has been used:

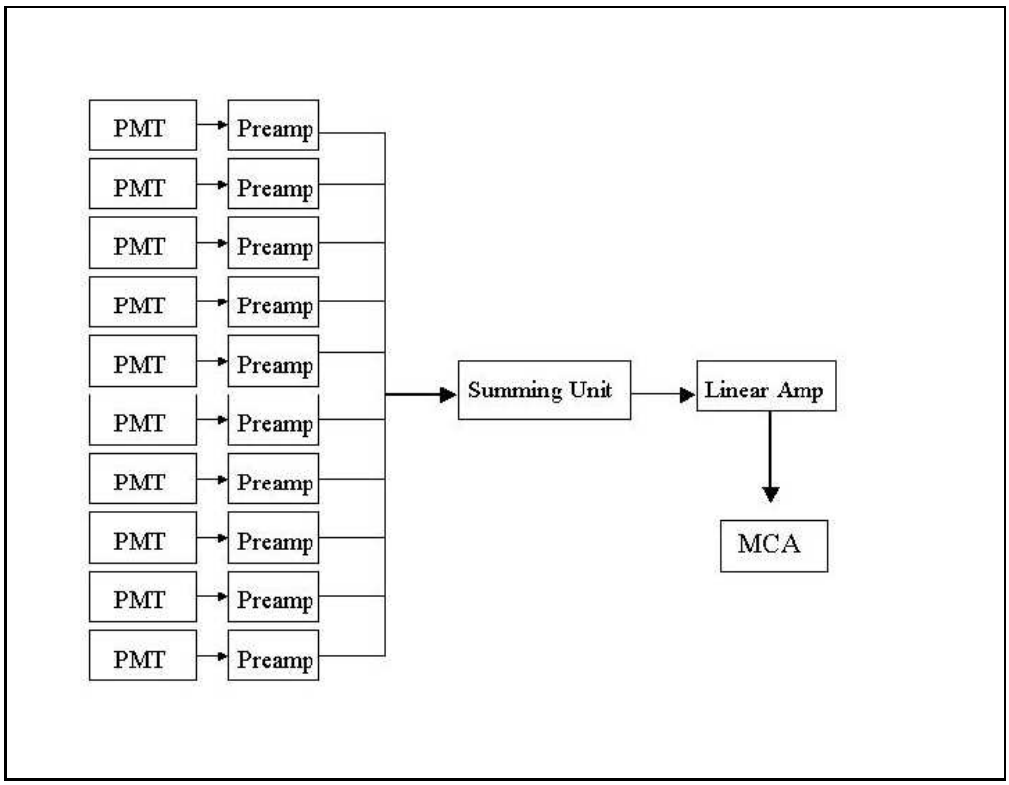

Figure 4.4: Experimental arrangement for the processing of the signal from PMTs

The signals from up to ten photomultiplier tubes attached to up to five blocks of plastic scintillators (two per block, one at each end) are added together using a summing unit.

The Compton electrons which are produced following the gamma interactions inside the scintillators will lose energy by ionisation in the scintillator and produce scintillation photons which provide the signal which is detected by the PMT's. The range of a 1 MeV electron inside the organic plastic scintillator is $R = 4\,mm$. The signal from the PMT's is analysed with a multichannel analyser (MCA). The pulse height given by the MCA is proportional to the energy deposited inside the scintillator by the incident gamma i.e. the scattered electron energies.

The radiative gammas emitted by Gd following neutron capture have energies in the range 50 keV $\leq E_\gamma \leq$ 8 MeV (Fig. 3.3). For these gamma energies the main interactions inside the organic plastic scintillators are the Compton (incoherent) scattering processes (see Fig. 3.5).

The energy deposited by the gamma rays inside the scintillator in one Compton scattering process is given by the energy of the recoiling electron:

$$E_e = E - E' = E - \frac{E}{1 + (\frac{E}{m_e c^2})(1 - cos\theta)} \tag{4.5}$$

where E' is the scattered gamma's energy, E is its initial energy, $m_e c^2$ is the electron rest energy and θ is the scattering angle.

The maximum and minimum values of the electron energy correspond to $\theta = \pi$ and $\theta = 0$ respectively. The maximum value is called the Compton edge energy. For a Compton scattering event generated by a gamma coming from ^{137}Cs source with an initial energy $E_\gamma = 662\, keV$, the recoil electron will lie within the energy region: $0 \leq E_\gamma \leq 478\, keV$:

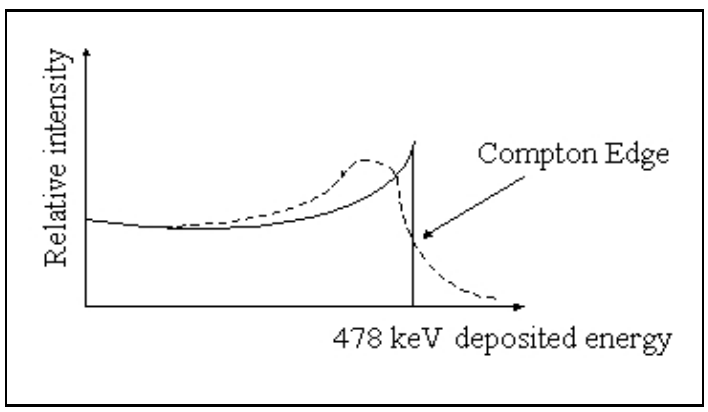

Figure 4.5: Compton continuum energy spectrum: *theoretical* (the continuous line) and *realistic* (the dot line)

Because the scattered electrons inside the scintillator are not truly free electrons and also because of the finite energy resolution of the scintillator, the Compton edge will have a slope "tail" (Fig. 4.5) rather than a step function drop to zero.

4.3 Energy Resolution of the Detector

4.3.1 Definition of the Energy Resolution

The detector gamma response can be examined by noting the detector response to a monoenergetic source.

The energy resolution of the detector can be defined as:

$$R_q = \frac{\overline{q^2} - \overline{q}^2}{\overline{q}^2} \tag{4.6}$$

where q is the collected electric charge at the photomultipliers following a scintillation event.

The advantage in using monoenergetic gamma sources is that the energy deposition inside the detector is better understood. However, due to statistical fluctuations there will be random fluctuations in the charge q which is generated in one event. These fluctuations will always be present in the detector signal even if exactly the same amount of energy is deposited in the detector for each event .

In the previous section it has been shown that the pulse amplitude H_0 is proportional to the number of collected electric charges $H_0 = kN$, where k is a proportionality constant.

Assuming that a total number N of charge carriers is generated on average and that the formation of each charge carrier is a Poisson process, one would expect a standard deviation $\sqrt{N}$ to characterize the inherent statistical fluctuations in the signal. The standard deviation σ of the peak in the pulse height spectrum (Fig. 4.6) is then $\sigma = k\sqrt{N}$. The response function of the detector should have a gaussian shape since N is typically a large number.

The $FWHM$ (Full Width at Half Maximum) for a gaussian is given by

$$FWHM = 2.35\sigma \tag{4.7}$$

so that the $FWHM = 2.35k\sqrt{N}$.

A formal definition of detector energy resolution is shown in (Fig. 4.6) with the assumption that only monoenergetic radiation is being recorded.

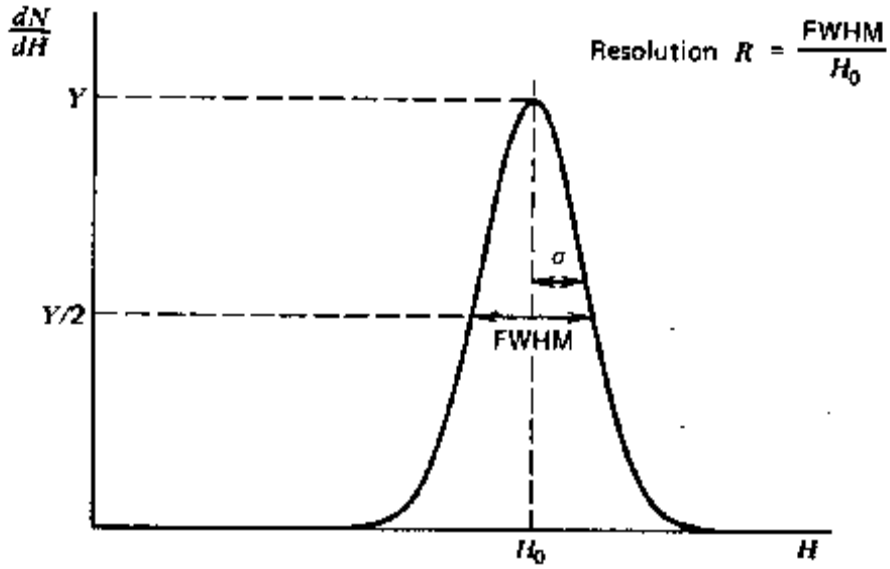

Figure 4.6: Definition of detector resolution for peaks whose shape is a Gaussian with standard deviation σ, the FWHM is given by 2.35σ

The energy resolution of the detector is defined as the $FWHM$ divided by the location of the peak centroid H_0. The energy resolution is thus a dimensionless fraction conventionally expressed as a percentage.

$$R_N = \frac{FWHM}{H_0} = \frac{2.35k\sqrt{N}}{kN} = \frac{2.35}{\sqrt{N}} \tag{4.8}$$

Since the number of charges collected after a detection event N is proportional to the energy deposited inside the scintillator the energy resolution can be also expressed as:

$$R_E = \frac{2.35k}{\sqrt{E}} \tag{4.9}$$

4.3.2 Energy Resolution Measurements

The energy resolution can be calculated using the assumption that the detector response to a single energy can be approximated to a gaussian (Fig. 4.6).

For a gaussian,

$$f(x) = \frac{1}{\sqrt{2\sigma^2\pi}} e^{-\frac{(x-x_0)^2}{2\sigma^2}} \tag{4.10}$$

The maximum value, $f(x_0)$, occurs for $x = x_0$ and it is equal to

$$f(x_0) = \frac{1}{\sqrt{2\sigma^2\pi}} \tag{4.11}$$

and the 90% of the maximum value is:

$$f(c_{90}) = 90\% f(x_0) = \frac{90}{100} \frac{1}{\sqrt{2\sigma^2\pi}} \tag{4.12}$$

The 50% and the 10% values are at $x = c_{50}$ and $x = c_{10}$ respectively:

$$f(c_{50}) = 50\% f(x_0) = \frac{50}{100} \frac{1}{\sqrt{2\sigma^2\pi}} \tag{4.13}$$

$$f(c_{10}) = 10\% f(x_0) = \frac{10}{100} \frac{1}{\sqrt{2\sigma^2\pi}} \tag{4.14}$$

From equations (4.11 - 4.14) one can calculate the x values at the 90%, 50%, and 10% respectively of the gaussian maximum:

$$c_{90} = x_0 + 0.459\sigma \tag{4.15}$$

$$c_{50} = x_0 + 1.1774\sigma \tag{4.16}$$

$$c_{10} = x_0 + 2.146\sigma \tag{4.17}$$

If the peak (Fig. 4.6) is superimposed with a continuum as shown in Figure 4.7,

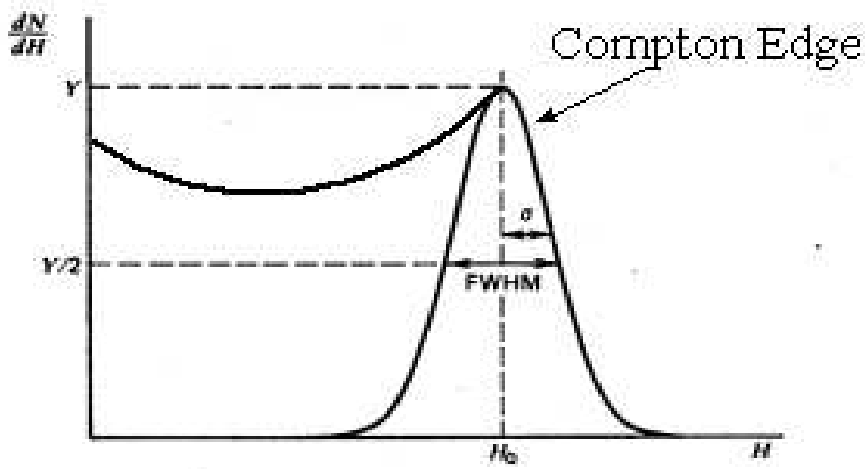

Figure 4.7: Compton continuum spectrum with a finite resolution

then the energy resolution of the detector can be defined as [57]:

$$R = \frac{\sigma}{c_{50}} \tag{4.18}$$

Using the values of the channel numbers for which the number of counts is 90%, 50% and 10% respectively of the maximum value (see Figures 4.8 - 4.11) one can compute the value of the energy resolution, using the Equation 4.18.

The procedure is not exact since the Compton edge is not exactly a Gaussian. But experience has shown that the approximation is a good one and this procedure gives consistent and reliable results.

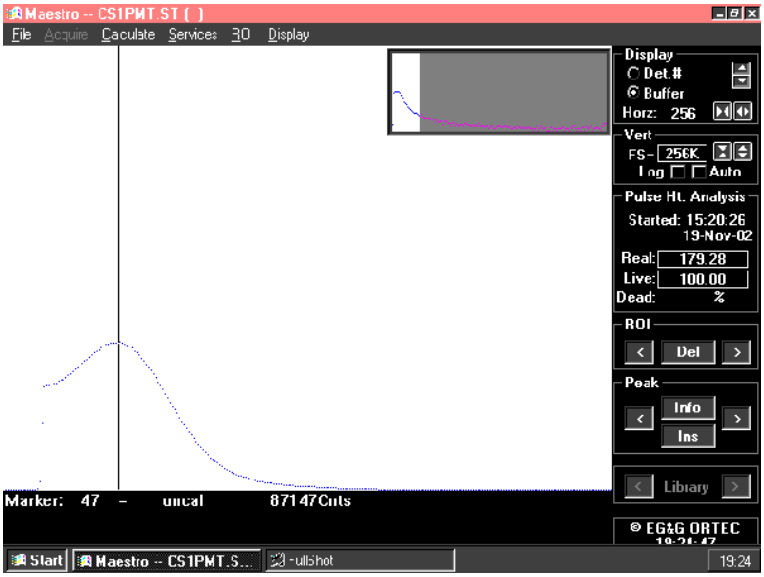

Figure 4.8: The channel number corresponding to the maximum no. of counts in the Compton continuum of the ^{137}Cs source measured with only one PMT

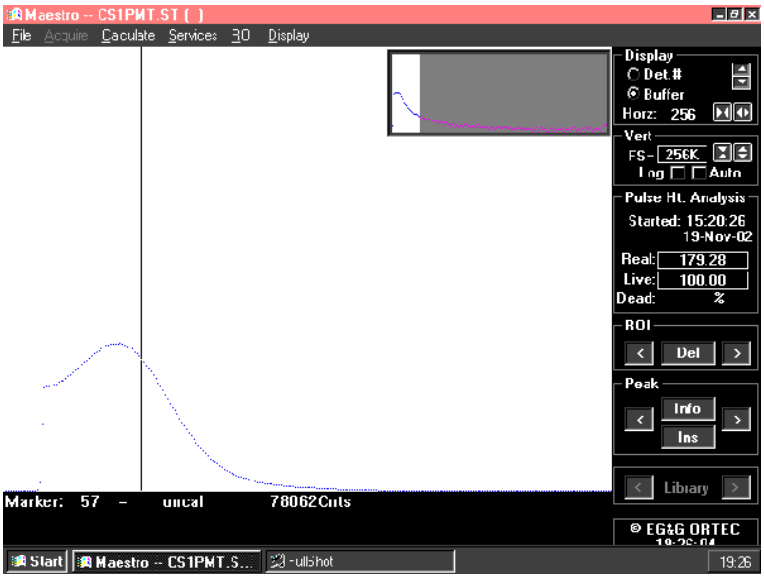

Figure 4.9: The channel number corresponding to the 90% of the maximum no. of counts in the Compton continuum of the ^{137}Cs source measured with only one PMT

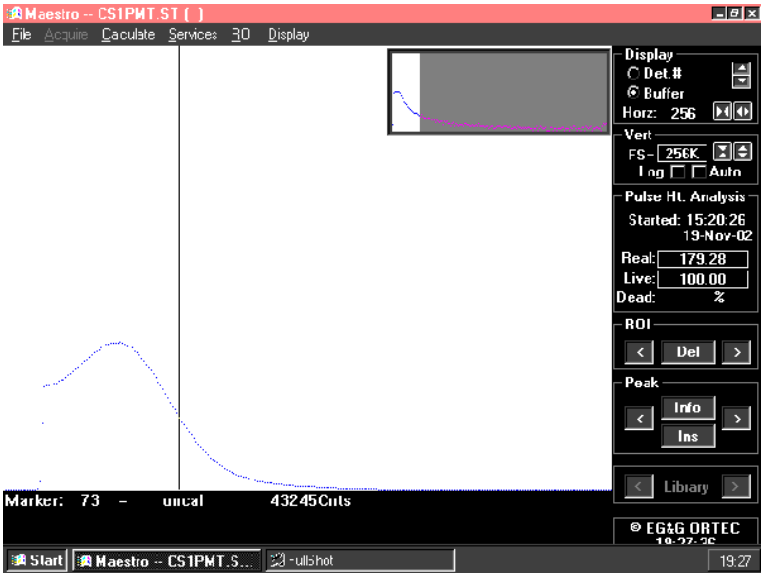

Figure 4.10: The channel number corresponding to the 50% of the maximum no. of counts in the Compton continuum of the ^{137}Cs source measured with only one PMT

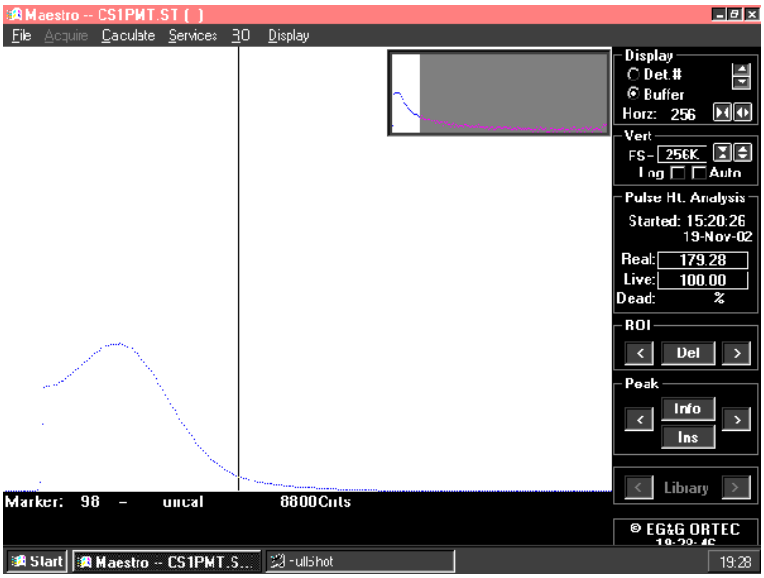

Figure 4.11: The channel number corresponding to the 10% of the maximum no. of counts in the Compton continuum of the ^{137}Cs source measured with only one PMT

In the case of the spectrum measured with only one photomultiplier from one scintillator with the source being centrally on top of the scintillator, the energy resolution is $R_{1PMT} = 30.7 \pm 2.6\%$.

When the 137-Cs source spectrum is measured with both PMT's from one scintillator block, with the source in the same position, the average number of charges collected in one detection event doubles, such that the expected resolution becomes (see equation 4.8):

$$R_{1scint} = \frac{R_{1PMT}}{\sqrt{2}} = 21.7\% \tag{4.19}$$

The experimental value which was actually measured with both PMT's is

$$R^{exp}_{1scint} = 23.2 \pm 1.6\% \tag{4.20}$$

The two resolutions, one obtained with a single PMT at one end and the other with a PMT at each end, are therefore consistent with each other. The numbers provide some confidence that the resolution can be understood.

4.4 Light Attenuation Measurement

An important criterion in selecting the scintillators (especially long scintillators) is the light attenuation length inside the scintillator.
The attenuation of light inside a scintillator is described by the exponential law :

$$I = I_0 \, e^{-\mu x} \tag{4.21}$$

where I is the light intensity after travelling through a distance x inside the scintillator, I_0 is the initial intensity and μ is the attenuation coefficient.

In order to determine the attenuation coefficient μ, a radioactive source was placed at different points along the plastic scintillator thus producing events within the scintillator at known distances from the photomultiplier tubes. The signal from the photomultiplier tube, which is proportional to the number of photons reaching the photomultiplier, was measured for each point. It is advantageous to choose monoenergetic gamma sources so that the amount of energy which is deposited is better understood. A ^{137}Cs source which produces 662 keV gamma rays was chosen. These gammas will deposit inside the scintillator an amount of energy which is converted into visible light, the number of the scintillation photons produced being proportional to the deposited energy. The number of scintillation photons which will reach the photomultipliers depends on the position of the source along the scintillator (see equation 4.21) and the light attenuation length λ which is defined as the inverse of the attenuation coefficient :

$$\lambda = \frac{1}{\mu} \tag{4.22}$$

The light attenuation length was measured by placing the ^{137}Cs source at different distances x_{middle} (mm) from the middle of the scintillator as illustrated in Figure 4.12 and by measuring the shift in the channel number associated with the Compton edge energy.

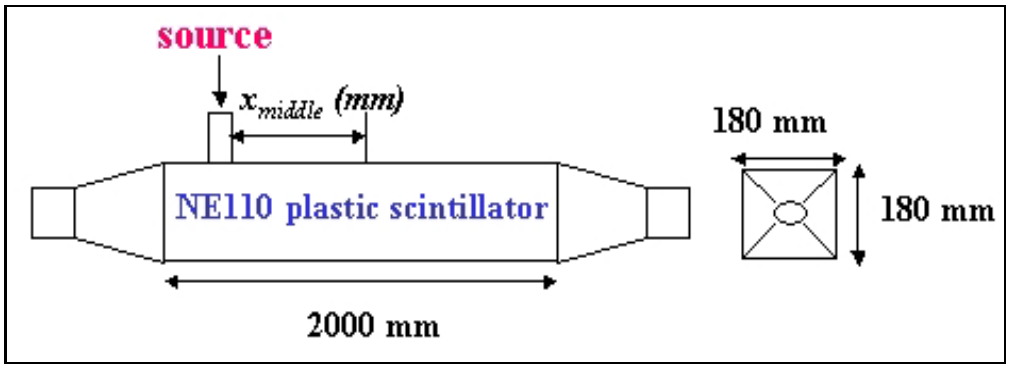

Figure 4.12: Light Attenuation Measurement

The figures (4.13 - 4.15) show the dependence of the signal measured with left and right photomultiplier respectively on the position of the source along the scintillator (the distances to the left with respect to the centre of the scintillators are chosen to be negative). Because the scintillation light suffers an exponential attenuation inside the scintillator, on a logarithmic scale the dependence of the signal on the distance should be linear :

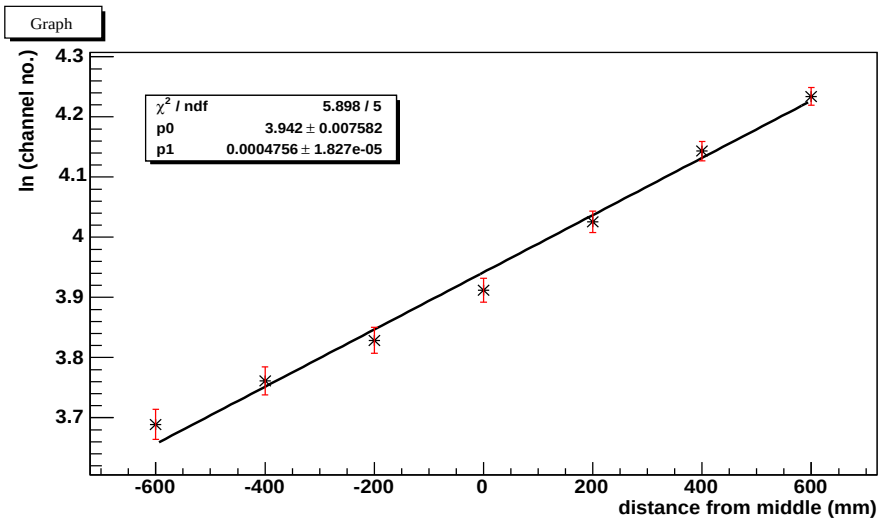

Figure 4.13: Light Attenuation Measurement with the 'Right' PMT

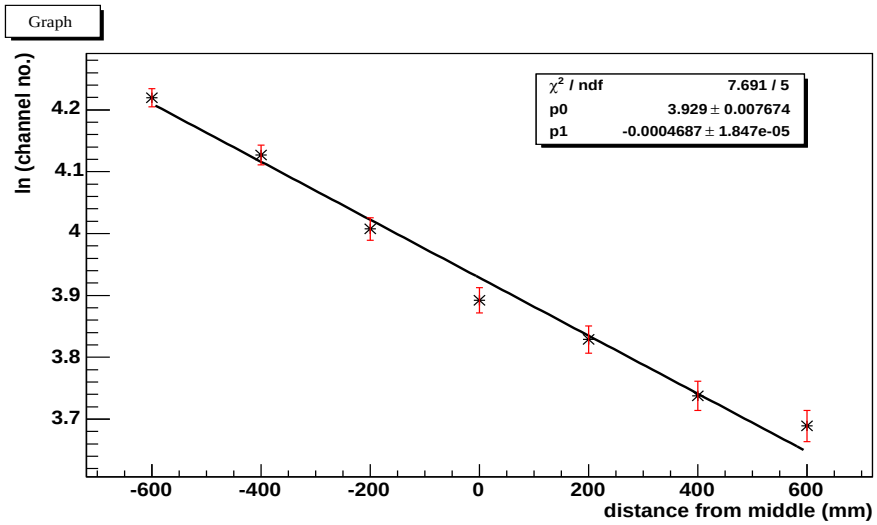

Figure 4.14: Light Attenuation Measurement with the 'Left' PMT

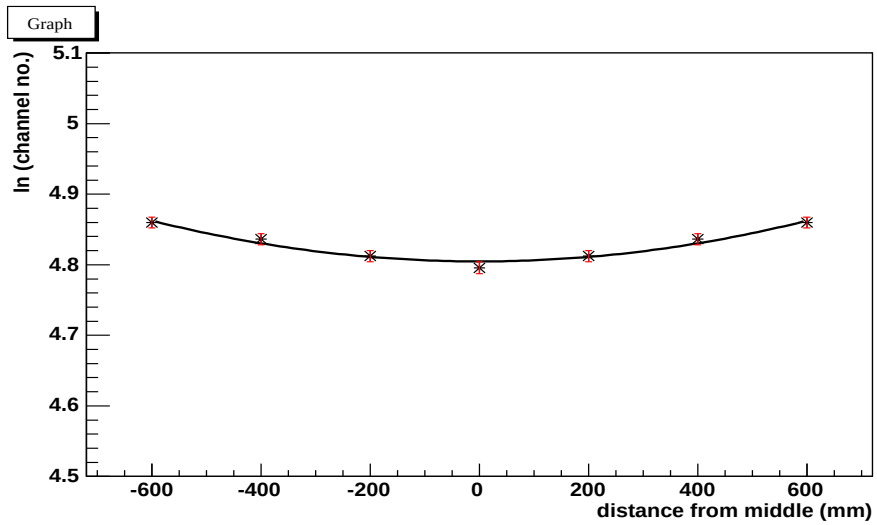

Figure 4.15: Light Attenuation Measurement with both PMT's

The attenuation coefficient μ is given by the average slope of the lines in figures 4.13 and 4.14, $\mu = 0.000472\,mm^{-1}$, which implies that the attenuation length inside this scintillator is $\lambda = \frac{1}{\mu} = 2119$ mm. Since the length of this scintillator is 2000 mm, it is suitable for use in the OMNIS project.

Figure 4.16 shows the position of the Compton edge of ^{137}Cs (in channel numbers) measured with both photomultiplier tubes as a function of the source position along

the scintillator. From the figure, there is a factor of only 1.066 variation in the energy scale between the centre and ends of the scintillator block. Therefore a rectangular distribution may be considered for the Compton edge position (with $y_{mean} = 125$ and $\sigma = \frac{y_{max}-y_{min}}{\sqrt{12}}$), where y represents the ADC channel associated with the Compton Edge:

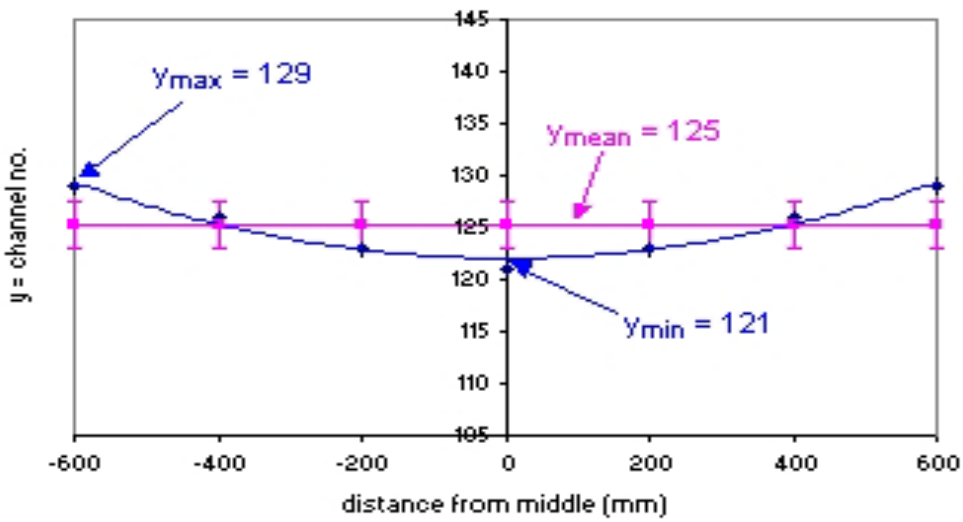

Figure 4.16: Light Attenuation Measurement with both PMT's

For one scintillator block the attenuation coefficient was measured to be $\mu = 0.001$ mm $^{-1}$ which corresponds to an attenuation length of $\lambda = 1000\,mm$. Thus for this scintillator the light attenuation length is half of its length and therefore it has been rejected. This difference in performance is probably due to history. The scintillators were used for a few years for an experiment at Daresbury Laboratory from 1967 onward. They were then used for cosmic ray studies by Leeds University before they were returned to The University of Manchester for this purpose. One scintillator had been unwrapped at the end for several years and this was the one with the short attenuation length. All the other blocks which remained wrapped have a longer attenuation length.

4.4.1 The Effect of Light Attenuation on the Energy Resolution

The light attenuation inside the scintillator will affect the number of scintillation photons reaching the PMT's. Therefore the number of scintillation photons reaching the PMT's will decrease exponentially with increasing distance and so will the average number of photoelectrons produced in one detection event. This will affect the value of the energy resolution of the detector (see equation 4.8).

The average value of the light attenuation coefficient for the four NE110 organic plastic scintillator block has been measured in the previous section to be $\overline{\mu} = 0.0005\, mm^{-1}$.

Hence, since the average number of charges collected at the PMT's can be expressed as

$$N(x) = N(0)\, e^{-\mu x} \tag{4.23}$$

and using equation 4.8 for the energy resolution of the detector, the dependence of the resolution on the distance the light travels inside the scintillator can be written as:

$$R(x) = R(0)\, e^{+\frac{\mu x}{2}} \tag{4.24}$$

where $R(0)$ is the energy resolution if there was no light attenuation inside the scintillator, and $R(x)$ is the real energy resolution which takes into account the light attenuation effects when the light travels the distance x inside the detector.

The energy resolution measured with the source in the middle is

$$R_{1PMT} = R(L/2) = 30.7 \pm 2.6\% \tag{4.25}$$

where L = 2000 mm is the length of the scintillator.

The energy resolution can be also expressed in terms the distance x_{middle} from the middle of the scintillator to the source (see Fig. 4.12):

$$R(x_{middle}) = R(L/2)\, e^{-\frac{\mu x_{middle}(mm)}{2}} \tag{4.26}$$

Using equation 4.26 one can predict the values of the energy resolution for different distances between the source and the middle of the detector:

$x_{middle}(mm)$	-600	-400	-200	0	200	400	600
R	35.0%	33.5%	32.1%	30.7%	29.4%	28.1%	26.9%

Table 4.1: Energy resolution calculated using the equation 4.26

The energy resolution values measured experimentally with the 'Right' PMT are shown in the following table:

$x_{middle}(mm)$	-600	-400	-200	0	200	400	600
R	30.3%	30.6%	30.9%	30.7%	28.3%	27.8%	27.1%
(Experimental Error)	±3.4%	±3.1%	±2.9%	±2.6%	±2.4%	±2.2%	±2.0%

Table 4.2: Energy resolution for one scintillator measured experimentally

The discrepancy which appears for the data measured with source placed at the 'far' end with respect to the photomultiplier is due to the fact that the standard assignment in Equation 4.18 of the 50% maximum point of the Compton continuum (Fig. 4.5) to the Compton edge is not correct. Previous Monte Carlo calculations [52] show that because of multiple Compton scattering, gammas frequently deposit energy beyond the Compton edge. This will fill in the region below the Compton edge, which results in the identification of the 90% maximum point of the Compton continuum with the backscatter energy.

A more accurate method of measuring the energy resolution of the detector is presented in chapter 6, using the comparison between the GEANT4 simulation of the detector response to the gamma interactions and the measured data.

4.5 The Energy Calibration of the Detector

An ideal MCA would perform a perfectly linear conversion of pulse height to channel number:

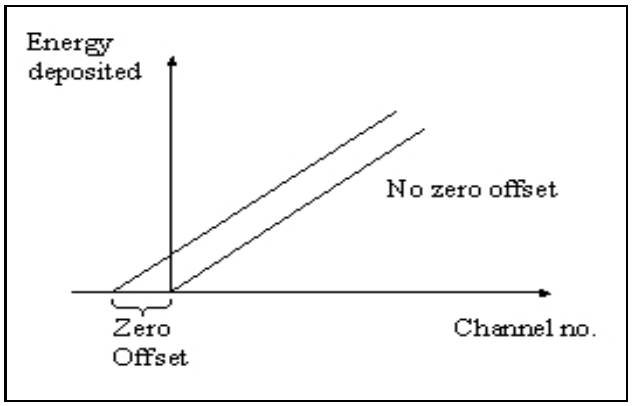

Figure 4.17: A typical MCA calibration plot

A nonzero amplitude required for storage in the first channel will introduce some zero offset shift to the origin.
Assuming the multichannel analyser is sufficiently linear, it is enough to determine the slope and the intercept of the calibration line (Fig. 4.17). However more gamma sources should be used to provide additional tests of the linearity of the MCA.

The first step of the calibration experiment was to match the gain of the PMT's at the two ends of each scintillator, by adjusting the high voltages independently using the Compton edge of a ^{137}Cs source (0.478 MeV) placed at the middle of the scintillator as a reference.
The easiest way to test the linearity of the MCA is to place sources of known energy on the detector and to measure the channel number into which the Compton edge of the spectrum falls. Three different well-known sources have been used: ^{137}Cs, ^{60}Co and ^{241}Am/Be.

The ^{60}Co source emits two gammas with 1.173 and 1.333 MeV which combine to produce a broad peak corresponding to an average energy of 1.25 MeV gamma signal.

The ^{241}Am/Be source emits 4.4 MeV gammas, as well as neutrons with energies between 2 and 10 MeV. The scintillator acts also as a neutron moderator, and the neutrons are thermalized and captured on hydrogen inside the detector. This process will give rise to a 2.2 MeV gamma.

The channel numbers corresponding to the Compton edges for the gammas emitted by these sources (see Fig. 4.18 - 4.21) are given in Table 4.3.

Source	Gamma Energy (MeV)	Compton Edge (MeV)	Channel No.
^{137}Cs	0.662	0.478	59
^{60}Co	1.25	1.038	137
^{241}Am/Be	2.2	1.971	274
^{241}Am/Be	4.4	4.159	578

Table 4.3: The Compton edge energies and channel numbers for the gamma sources

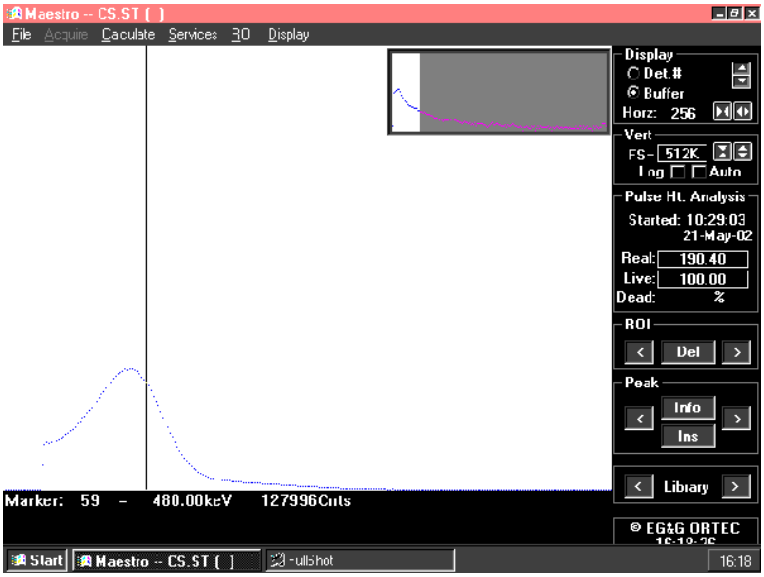

Figure 4.18: Energy spectrum of the ^{137}Cs source

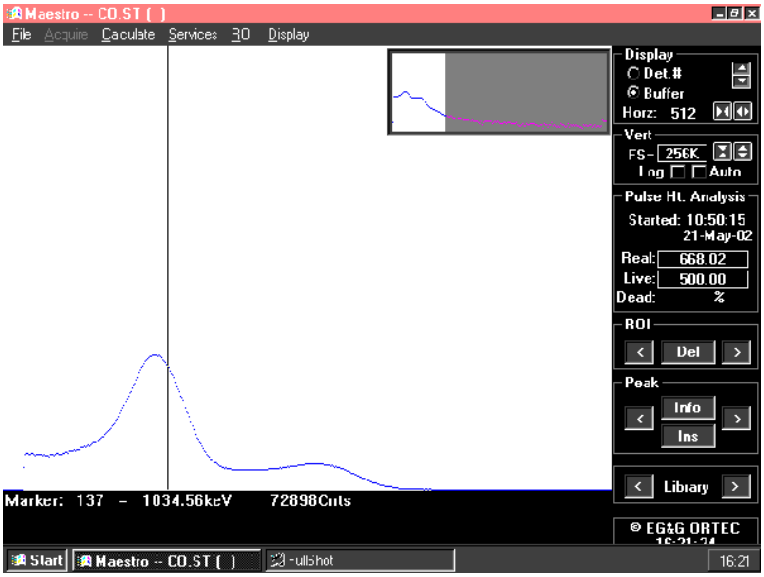

Figure 4.19: The energy spectrum of the ^{60}Co source

The second peak in Fig. 4.19 is caused by the coincidence of the two gammas emitted by the ^{60}Co source which leads to a deposited energy equal to the sum of the two deposited energies.

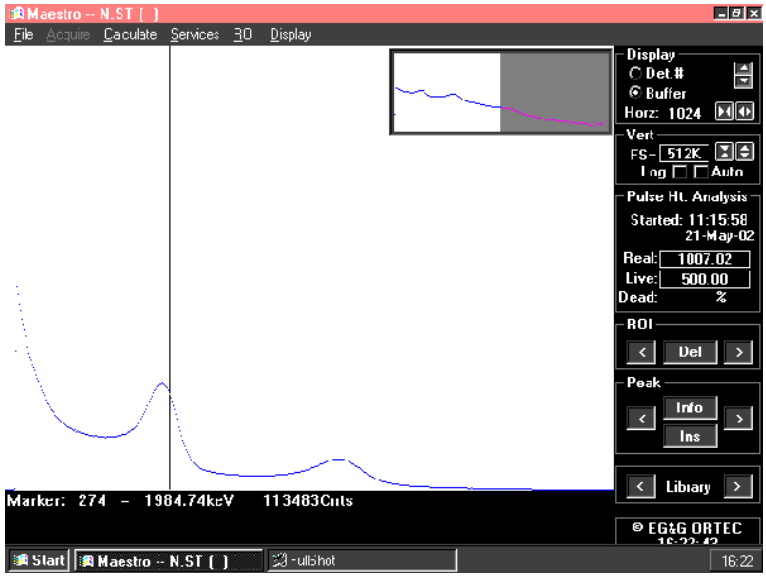

Figure 4.20: Energy spectrum of the ^{241}Am/Be source - the Compton Edge of the 2.2 MeV gammas from neutron capture on H inside the scintillators

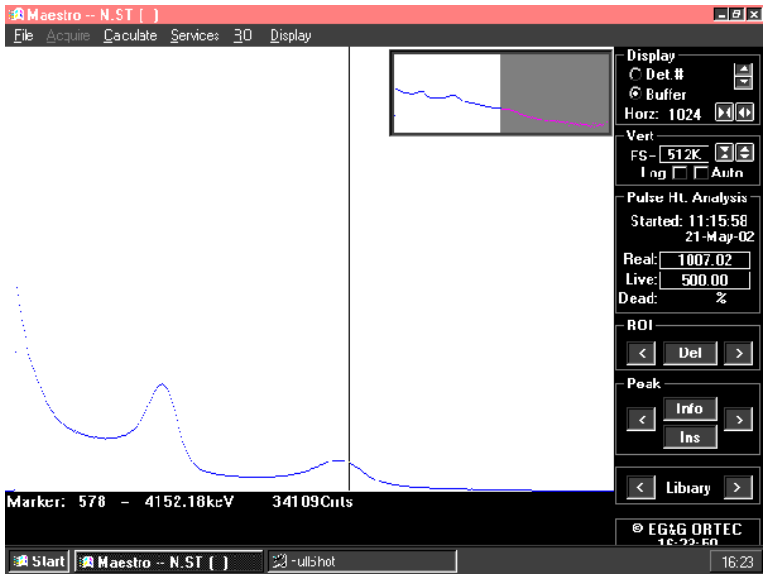

Figure 4.21: Energy spectrum of the ^{241}Am/Be source - the Compton Edge of the 4.4 MeV gammas emitted by the source

The values given in Table 4.3 were used for plotting the dependence of the ADC channel number on the energy deposited inside the detector. The following MCA calibration plot shows that there is a linear dependence between the energy deposited inside the detector and the channel number, over the energy range 500 - 4500 keV.

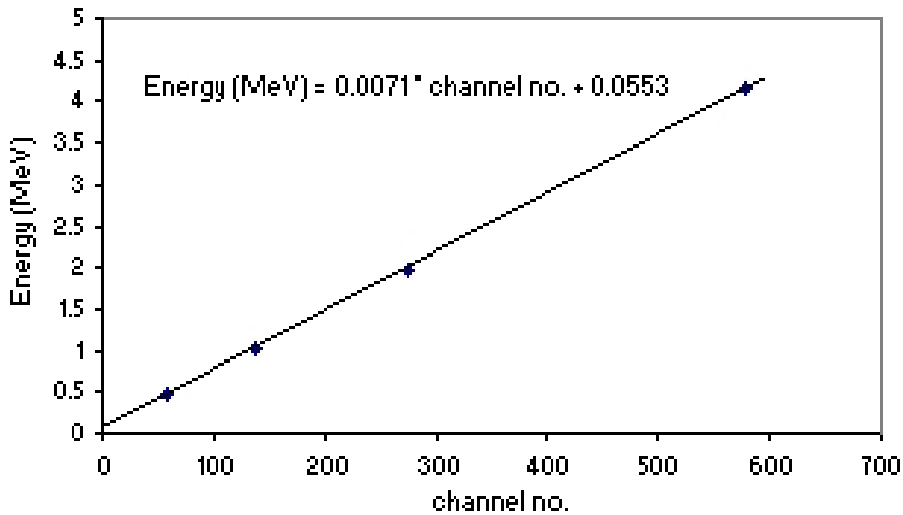

Figure 4.22: Energy Calibration of the MCA

This plot can be used to determine the energies of the gammas emitted in the neutron capture process.

The absorption length of the gammas inside the scintillator can be calculated using the mass energy-absorption coefficients introduced in section 3.2.2.
The values of the mass energy-absorption coefficient for the gamma energies used to perform the energy calibration of the plastic scintillators are given in table 4.4.

Source	Energy (MeV)	Mass Energy-Absorption Coefficient (cm^2/g)
^{137}Cs	0.662	3.175×10^{-2}
^{60}Co	1.173	2.94×10^{-2}
^{60}Co	1.332	2.85×10^{-2}
^{241}Am/Be	2.2	2.45×10^{-2}
^{241}Am/Be	4.4	1.91×10^{-2}

Table 4.4: The mass energy-absorption coefficients inside the NE110 plastic scintillators

Using these values one can compute the "mean free path" for energy loss (the absorption length), which represents the distance travelled inside the scintillator after which the gammas will have an average energy equal to 1/e (i.e. $\approx 36.8\%$) of their initial energy. These distances are shown in table 4.5.

Source	Energy (MeV)	Mean free path (mm)
^{137}Cs	0.662	305
^{60}Co	1.173	330
^{60}Co	1.332	340
^{241}Am/Be	2.2	396
^{241}Am/Be	4.4	507

Table 4.5: The energy loss process mean free path

Using the values of the mean free path for the energy loss process, it is possible to compute the fraction of the energy which is deposited inside the scintillator by these gammas.

The fractions of energy deposited by the gammas inside the scintillator described in Fig. 4.12 are shown in table 4.6.

Source	Energy (MeV)	Fraction of energy loss inside a $180 \times 180 \times 2000\, mm^3$ plastic scintillator (Fig. 4.12)
^{137}Cs	0.662	45%
^{60}Co	1.173	42%
^{60}Co	1.332	41%
^{241}Am/Be	2.2	37%
^{241}Am/Be	4.4	30%

Table 4.6: Fraction of energy deposited inside the scintillator

These values show that one scintillator block is not large enough for all the gammas to deposit their entire energy inside the detector and moreover, the fraction deposited is a strong function of energy.

The values of the fraction of energy deposited by the gamma-rays inside the detector can be computed in a similar way also for more blocks of scintillators.

Source	Energy (MeV)	Fraction of energy loss inside four $180 \times 180 \times 2000\, mm^3$ plastic scintillators
^{137}Cs	0.662	69%
^{60}Co	1.173	66%
^{60}Co	1.332	65%
^{241}Am/Be	2.2	60%
^{241}Am/Be	4.4	51%

Table 4.7: Fraction of energy deposited inside four scintillator blocks ($360 \times 360 \times 2000\, mm^3$)

As it can be seen in Table 4.7, for four blocks of scintillators, the average energy deposition inside the detector is higher than 50% for all the gamma energies in the

range 0.6 - 4.4 MeV, which were used in the calibration process. The detector must have more than one scintillator block in order to increase the fraction of energy deposited and thus to work better.

Chapter 5

Detection of Gammas from Neutron Capture

5.1 Configuration of the Detector

Five of the organic plastic scintillator blocks (NE 110) were selected on the basis of light attenuation length which had been measured to be in the range 2000 - 2500 mm. The scintillators have been tested for use in OMNIS project, each one being $180 \times 180 \times 2000\, mm^3$ in dimension. A table of their properties is given in the Appendix. Light guides were attached to each scintillator end and the whole then wrapped in PTFE tape. One (five inch) Hamamatsu type PMT was attached to the light guide at each end of the scintillator block, using optical grease. The scintillators and the light guides were wrapped in two layers of Al foil and black PVC tape in order to prevent external light entering the scintillators.

5.1.1 Gd paper on top of the five blocks of scintillators

To better understand neutron detection using Gd, the arrangement shown in figure 5.1 was set up in the lab. Different experimental arrangements can be used in order to thermalize the neutrons. As a neutron source an ^{241}Am/Be source with an activity $\Lambda = 100$ mCi was used. This source emits 2.2×10^5 neutrons per second, with energies from 2 MeV to 10 MeV, as shown in figure 5.2.

The γ-ray emission rate per neutron is 0.7 at 4.43 MeV. For each experimental arrangement lead was used to reduce the intensity of the 4.43 MeV gammas emitted by the source.

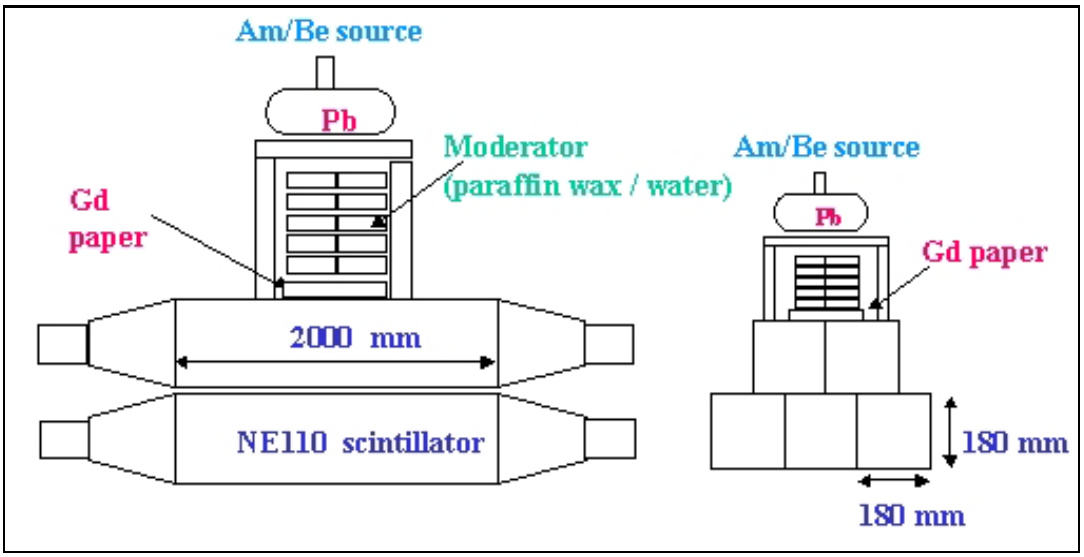

Figure 5.1: Gd paper on top of the 5 blocks of scintillator

The neutron detection process proceeds via the following stages [49]:

(i)Neutron slowing down is due to the neutron collisions with the hydrogen and carbon nuclei inside a hydrogenous moderator (e.g. water, paraffin wax or the scintillator itself).

These collisions include elastic collisions with the ^{1}H and ^{12}C and inelastic scattering with ^{12}C which are accompanied by the emission of at least one neutron in the final state. Below the threshold energy, $E_n = 4.813$ MeV, for the inelastic scattering to the first excited 4.443 MeV state in ^{12}C, only the elastic scattering contributes to the neutron slowing-down.

(ii) Radiative capture on ^{1}H followed by the emission of a single 2.224 MeV γ-ray or on ^{155}Gd (^{157}Gd) accompanied by the emission of a cascade of γ-rays with the summed energies of 8.536 (7.937 MeV, respectively). These γ's can be detected by large organic plastic scintillators.

(iii) Gamma-ray energy degradation due to consecutive Compton scattering from the electrons of H and C atoms of the scintillators. Ultimately, if the detector is large enough, the γ-ray energy is decreased to the level at which the photoelectric absorption in C terminates its history. Thereby nearly the entire energy (K-shell binding energy excluded) of the γ-ray cascade is converted into electron energy.

(iv) Electron energy loss by the excitation and ionisation of the medium molecules. Part of this energy (determined by the scintillation efficiency) is converted into visible light.

(v) Light transport to the photocathodes of the photomultipliers (PMTs) in optical contact with the plastic scintillators via multiple reflections on the diffusely reflecting surface of the scintillators.

The lab experimental arrangement chosen for neutron detection (Figure 5.1) consists of five NE110 plastic organic scintillators (each scintillator block is $180 \times 180 \times 2000\ mm^3$) and paraffin wax ($C_{25}H_{52}$) or light water ($H_2O$) between the Am/Be source and the scintillators to thermalize the neutrons before reaching the Gd paper.

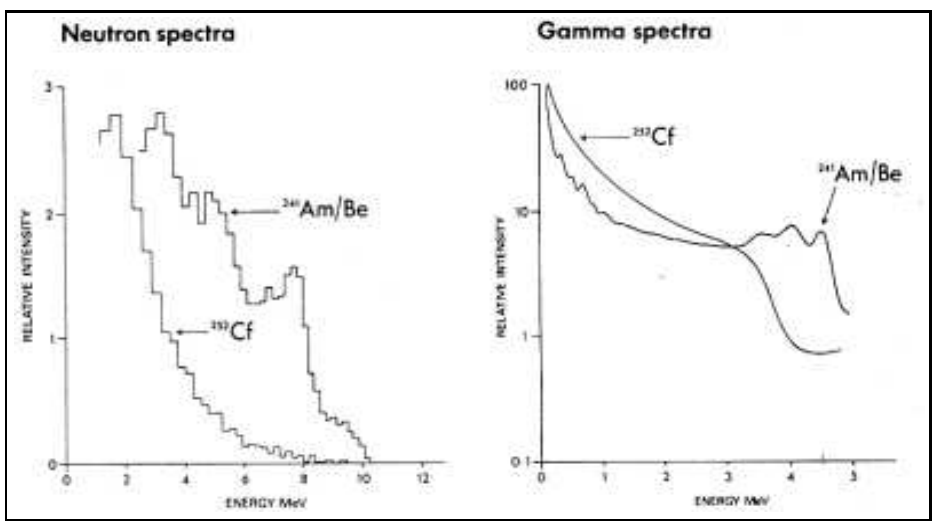

Figure 5.2: The neutron energy spectrum for the ^{241}Am/Be and the ^{252}Cf sources [60]

Ten blocks of paraffin wax were used with the average thickness of each block being 14 mm.

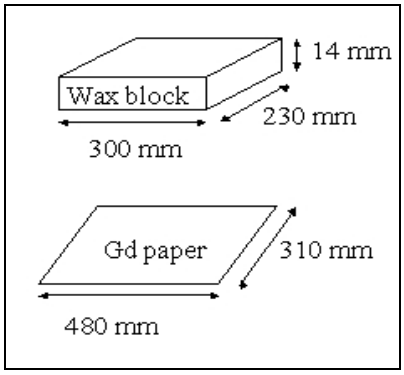

Figure 5.3: The size of the paraffin wax block and of the Gd paper

White paint was used in order to apply a uniform concentration of natural Gd on the paper. Different amounts of gadolinium oxide Gd_2O_3 have been carefully and thoroughly stirred into the paint; the amounts of gadolinium were chosen as percentages by weight of the total weight of ten blocks of moderator (7000g). The percentages chosen are given in table 5.1.1.

Gd concentration by weight (%)	Reference mass (g)
0.005	7000
0.01	7000
0.015	7000
0.02	7000
0.04	7000
0.1	7000

Table 5.1: Gd weight measured as percentage of the total weight of moderator

5.1.2 Gd paper between the top and bottom blocks of scintillator

In order to have a maximum detection efficiency, a "4π solid angle detector" can be approximated by surrounding the Gd paper with the five scintillator blocks as shown in figure 5.4.

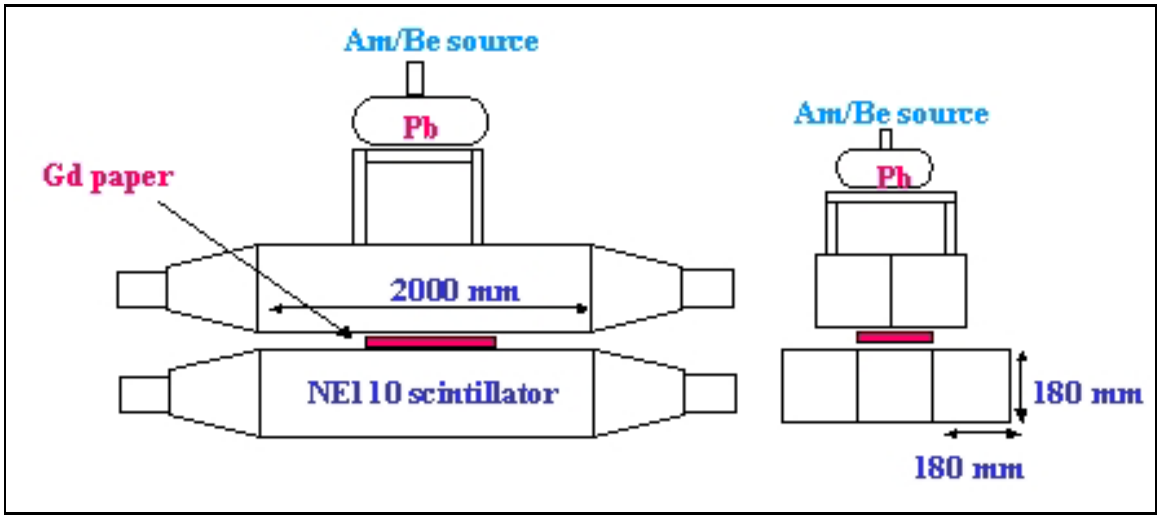

Figure 5.4: Gd paper surrounded by scintillator blocks

For this experimental arrangement the top scintillators can be used as neutron moderators, so there is no need for additional blocks of moderator to thermalize the neutrons emitted by the source before they will reach the Gd paper.

5.2 Analysis of the Depth of Moderator Needed to Thermalize the Neutrons

The neutrons produced by the neutrino interactions are expected to have initial energies of $\sim$ 1-2 MeV [21], hence moderation will primarily occur through elastic scattering off the protons inside the moderator. The amount of energy given up by the neutrons at each scattering site depends on the atomic number of the scattering nucleus. The energy absorbed by the recoil nuclei increases as the atomic number decreases. Hydrogenous (low Z), materials such as water and paraffin wax ($C_{25}H_{52}$) are therefore efficient as neutron moderators.

For the experimental arrangement in figure 5.1, the solid angle from the neutron source to the Gd paper is $\Omega = 0.36\ \pi$:

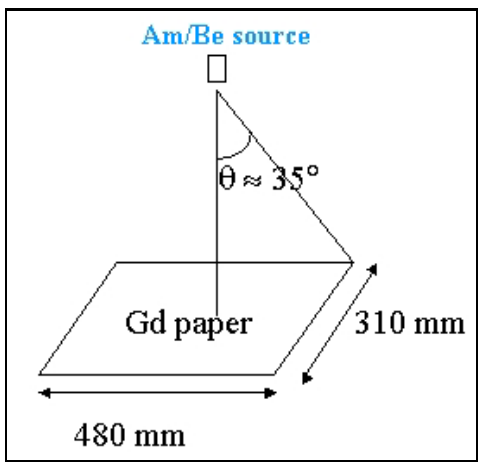

Figure 5.5: The solid angle from the Am/Be source to the Gd paper

The Am/Be source emits 2.2×10^6 neutrons/sec per 1 Ci activity. Since the source has an activity $\Lambda = 100$ mCi it will emit $N = 2.2 \times 10^5$ neutrons/sec. Taking into account the solid angle $\Omega = 0.36\pi$ from the source to the Gd paper and assuming that the neutrons are emitted isotropically, the total number of neutrons reaching the Gd paper in the absence of the neutron moderator is

$$N = (0.36\pi/4\pi) \times 2.2 \times 10^5\ n/sec = 1.98 \times 10^4\ neutrons/sec \qquad (5.1)$$

The neutron energy spectrum for the ^{241}Am/Be source shows that the neutron energies are in the range 2 - 10 MeV, with a mean neutron energy of 4.5 MeV (figure 5.2). The probabilities for the source to emit neutrons of a given energy E_n(MeV) are given by the relative intensities obtained after the normalisation of the neutron energy spectrum. The number of neutrons reaching the Gd paper per second with an energy E_n(MeV) within the energy spectrum of the source, in the absence of the neutron moderator, is computed by multiplying these probabilities with the total number of neutrons reaching the Gd paper per second (equation 5.1). These values are given in table 5.2:

Neutron Energy E_n(MeV)	Probability to emit a neutron with E_n(MeV)	Number of neutrons reaching the Gd paper
2.000	0.0521	1032
2.956	0.0480	951
3.912	0.0453	897
4.868	0.0333	660
5.824	0.0275	544
7.258	0.0315	624
8.214	0.0089	176
9.170	0.0072	143
10.126	0.0010	20

Table 5.2: The number of neutrons reaching the Gd paper per second, with the energy E_n (MeV)

The neutron scattering and capture cross-sections for the ^{157}Gd are shown in Figure 5.6. It can be seen that the radiative capture on Gd processes set in after the neutron has slowed down into the Gd resonance region ($E_n \leq 300\,eV$). The following analysis computes the number of neutrons slowed down to energies below this energy, because these are the neutrons that will be captured on Gd. These neutrons will be referred to as slow neutrons.

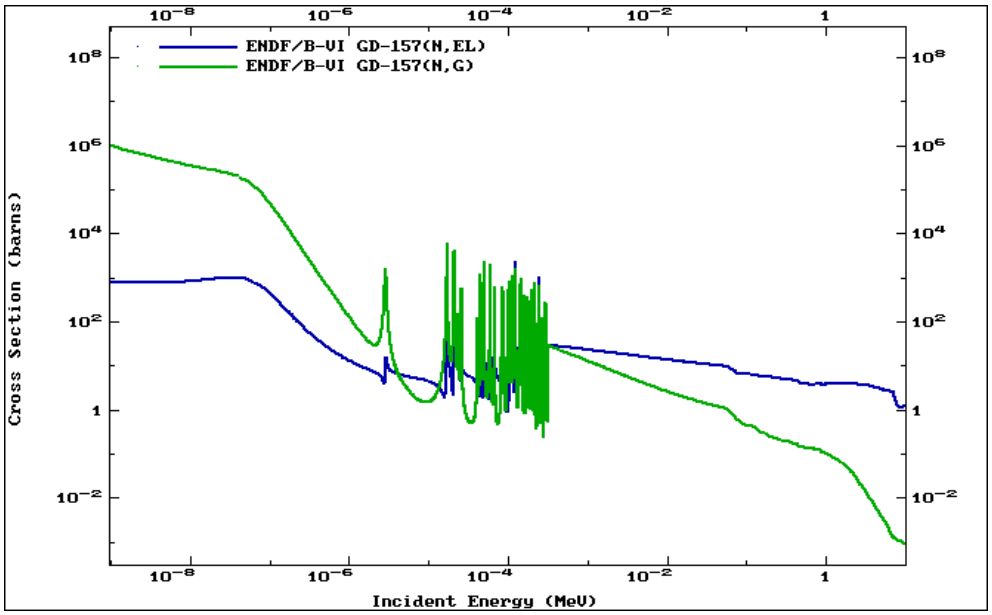

Figure 5.6: The neutron cross-sections for the radiative capture (green line) and scattering (blue line) processes on ^{157}Gd [59]

The probability for a neutron of a given initial energy E_n(MeV) to be moderated before reaching the Gd paper can be calculated using Equation 3.18 and the values of the coefficients given in Table 3.2.

The number of slow neutrons reaching the Gd paper per second can be calculated by multiplying this probability with the number of neutrons reaching the Gd paper in the absence of the moderator, having different initial energies in the range 2 - 10 MeV (table 5.2).

The numbers of slow neutrons reaching the Gd paper per second are shown in Figure 5.7 for different initial energies.

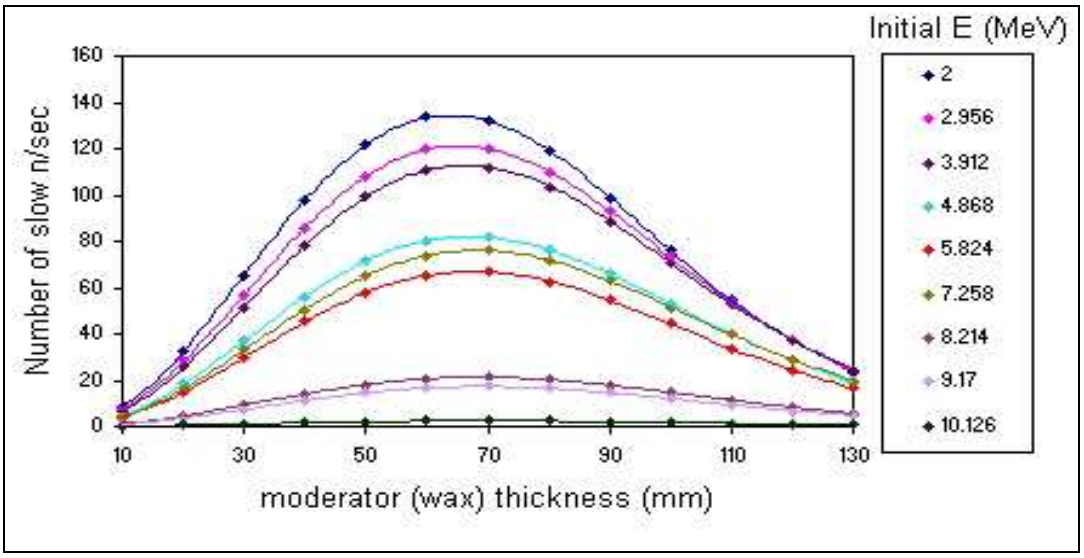

Figure 5.7: Number of slow neutrons reaching the Gd paper per second

It can be seen that the optimum depth of moderator is $\sim$ 60-70 mm.

Similarly, the probability to moderate the neutrons after passing through different depths of paraffin wax (equation 3.18) can be computed for each initial energy. The *total* number of slow neutrons reaching the Gd paper per second can be obtained integrating over the *whole* neutron source energy spectrum (figure 5.2). Fig. 5.8 shows the total number of slow neutrons reaching the Gd paper per second for different depths of the moderator (paraffin wax).

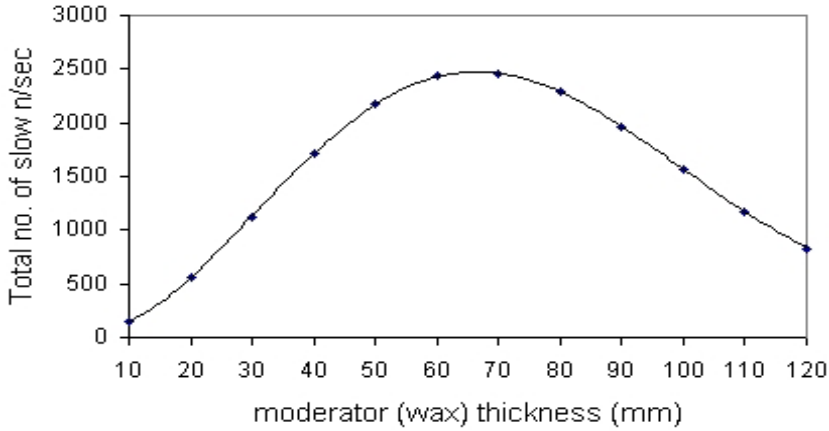

Figure 5.8: Total number of slow neutrons reaching the Gd paper per second for paraffin wax as neutron moderator

For 70 mm of paraffin wax $N = 2{,}462$ slow neutrons/sec.

A similar computation can be done for light water as a neutron moderator. Fig. 5.9 shows the total number of slow neutrons reaching the Gd paper per second as a function of the depth of the moderator (light water).

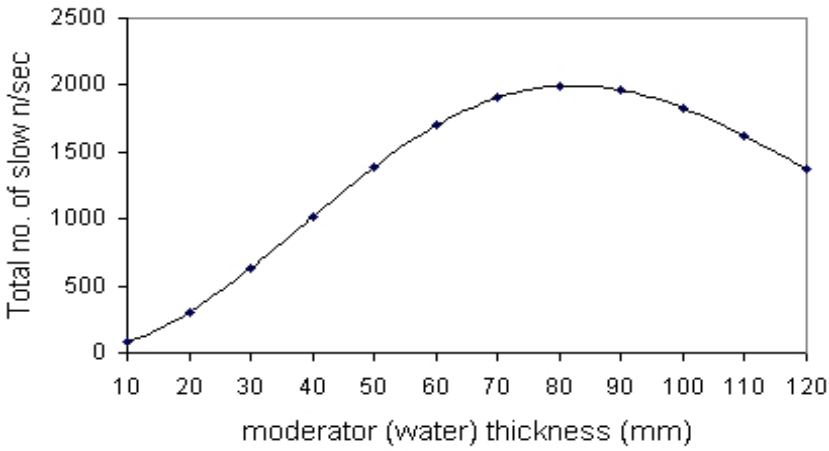

Figure 5.9: Total number of slow neutrons reaching the Gd paper per second for light water as neutron moderator

The optimum depth of light water is ~ 80 mm, for which the number of slow neutrons reaching the Gd paper per second is equal to $N = 1{,}993$ n/sec. Therefore the paraffin wax proves to be a more efficient neutron moderator than the light water.

Some of the slow neutrons will be captured on Gd, which results in the emission of a gamma cascade having the energy spectrum shown in Fig. 3.3.

5.3 Measurements of the Gamma Energy Spectrum from Neutron Capture on Gd

In the previous section the physical process which takes place in the thermalization of the neutrons has been considered and theoretical studies have been done to determine the optimum depth of moderator needed to thermalize the neutrons.

In Section 3.1.2 the analysis of the energy spectrum of the gammas emitted in the Gd decay showed that a $\sim$ 1 MeV gamma (transition 4 or 6) from the Gd decay is always preceded by a $\sim$ 2.7 MeV from the continuum (transition 3) or by a $\sim$ 5 MeV gamma (transition 5) respectively.
Two different experimental arrangements were presented in section 5.1 :

1. The Gd paper on top of the scintillators (Fig. 5.1)

The geometric efficiency for the detection which takes place only in half of the total solid angle (since any gammas emitted opposite to the direction of scintillators are not detected) is $\epsilon_{geom} = \frac{1}{2}$. So the probability to detect two gammas from the same Gd decay is the product of probabilities, $P = \frac{1}{4}$, assuming an intrinsic detection efficiency $\epsilon = 1$.

The probability to detect both the $\sim$ 1 MeV and the $\sim$ 5 MeV gammas from the Gd decay is further reduced by the intrinsic efficiency of the scintillator to detect the high energy gammas which have a higher mean free path and can escape undetected. Theoretical studies have been done to calculate the mean free path for gammas with different energies (see Table 4.5) and to determine the size of the scintillator blocks needed to detect a significant fraction of the total energy ($\sim$ 8 MeV) of the gammas from neutron capture on Gd.

So in the case of this experimental set up it is less likely to detect two or more gammas from the same neutron capture event. Both the 1 MeV gamma and the 2.7 MeV, or 5 MeV gamma respectively will be seen as two distinct events:

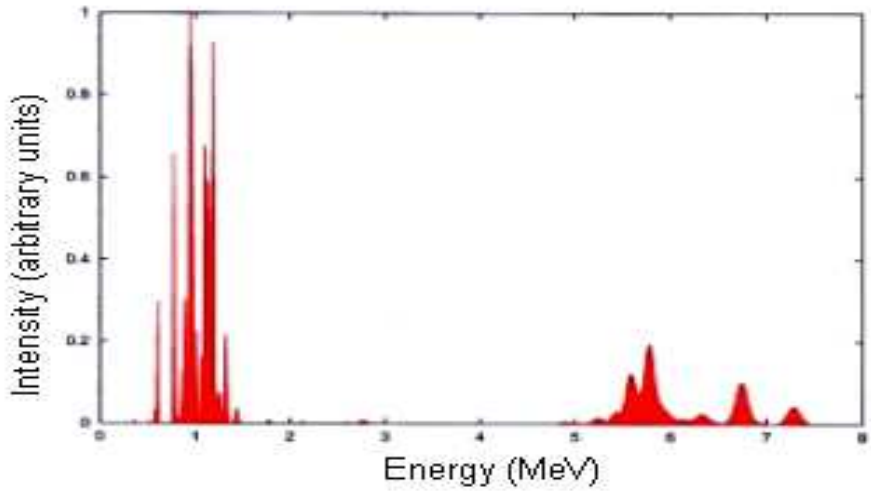

Figure 5.10: Gammas emitted in discrete levels - discrete levels transitions [72]

The spectrum should consist of two peaks: one due to the ~ 1 MeV gammas and the second peak corresponding to a gamma energy of 2.7 MeV. The high energy peak (~ 5 MeV) is not seen because the detector is not large enough for these gammas to deposit all their energy inside it (see subsection 3.2.2). These gammas escape undetected or Compton scatter few times thus adding to the continuum.
This is a very unsatisfactory situation.

The gamma energy spectrum emitted following neutron capture on Gd nuclei is obtained by subtracting the spectrum measured with the ^{241}Am/Be source without Gd (Fig. 4.20) from the spectrum measured with the ^{241}Am/Be source together with the Gd paper (experimental set up shown in Fig. 5.1). The thermal neutron capture spectrum on Gd thus obtained is shown in Fig. 5.11.

The gap between the two peaks, i.e. the dip, (Fig. 5.11) is centred around 1.971 MeV, the Compton edge corresponding to the 2.2 MeV gammas from neutron capture on hydrogen inside the scintillator. The presence of the gap is due to the fact that when Gd paper is used in the experiment, some of the neutrons are captured on Gd so fewer neutrons will enter the scintillator before being captured on hydrogen.

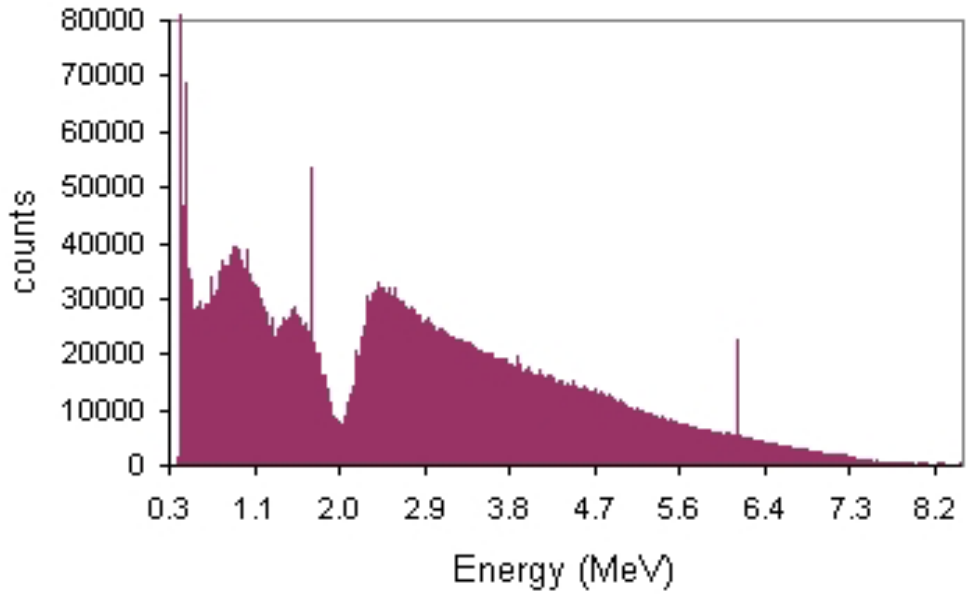

Figure 5.11: Neutron capture gamma spectrum measured with the Gd paper on top of the scintillator blocks

Hence when Gd paper is used there are fewer 2.2 MeV gammas than in the case when the spectrum is measured without Gd, and this will create, after the spectrum subtraction, a gap at the Compton edge of these 2.2 MeV gammas.

Different Gd papers were used for this experimental arrangement (Fig. 5.1). The Gd concentration varies from 0.005% to 0.1% by weight from 1400g (the average weight of two blocks on paraffin wax). The number of capture events increases with Gd concentration until a saturation point is reached around 0.1% (Fig. 5.12).

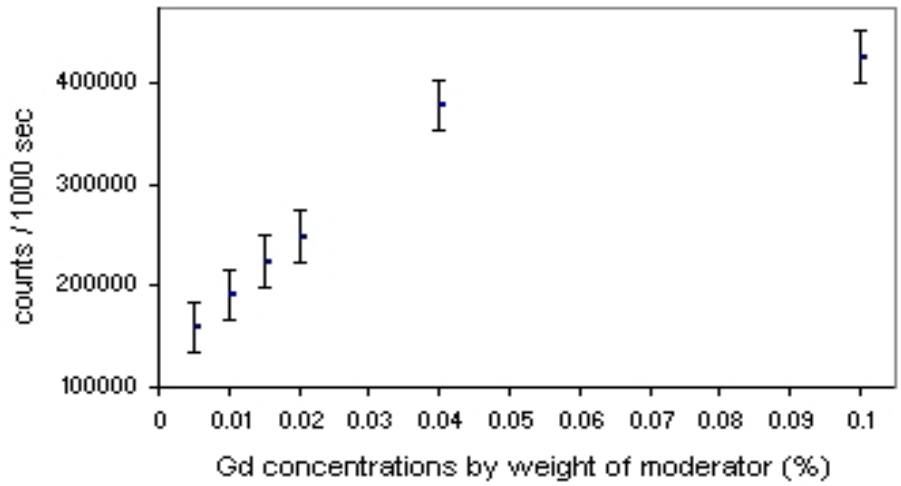

Figure 5.12: Gd capture events for different Gd concentrations

The statistical errors are negligible compared to the systematic errors in distributing the mass of the Gd into the paint and applying it to the paper. In order to determine the errors, counts were repeated using different sheets of the same Gd concentration.

Tests have also been done to determine from the experiment the optimum depth of moderator required to thermalize the neutrons. The results are shown in Fig. 5.13 for different depths of paraffin wax as neutron moderator.

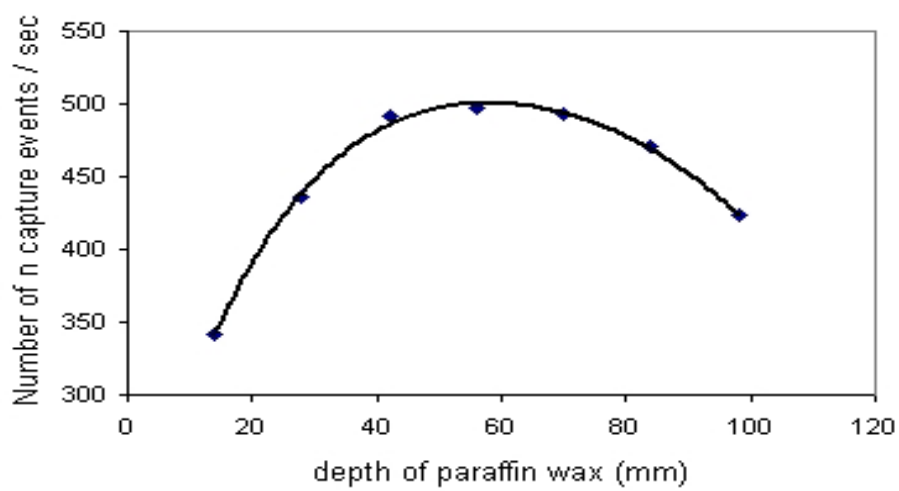

Figure 5.13: Gd capture events for different depths of paraffin wax as neutron moderator

The optimum depth of paraffin wax has been measured to be $\sim$ 60 mm, in good agreement with the calculated value of 60-70 mm (see Fig. 5.8).

Similar measurements were done for light water, showing that a depth of $\sim$ 70-80 mm is the optimum configuration for this moderator. The results are shown in Figure 5.14:

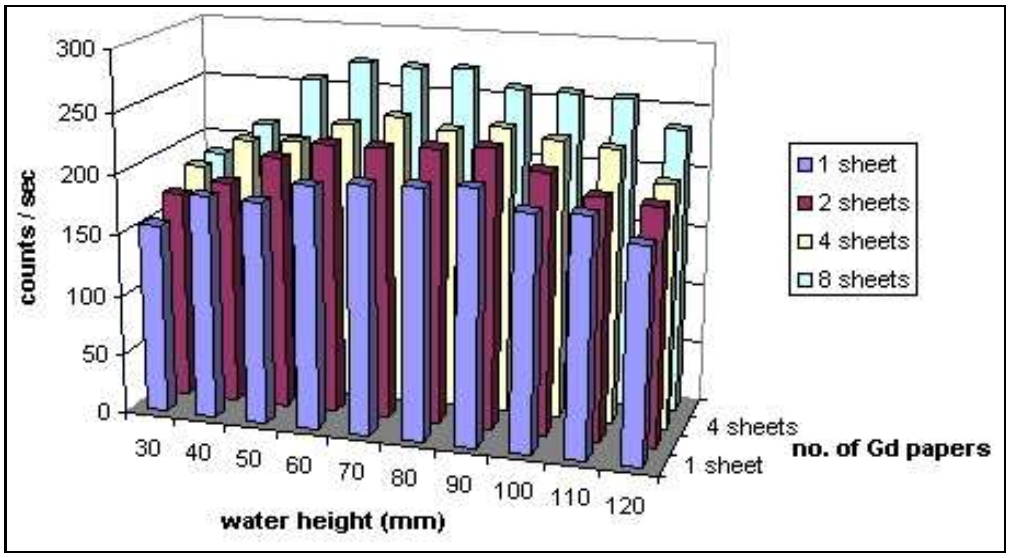

Figure 5.14: Gd capture events for different depths of light water as neutron moderator

2. The Gd paper surrounded by scintillator blocks (Fig. 5.4)

For this experimental arrangement when the Gd paper is completely surrounded by scintillators, the detection takes place in almost the whole solid angle $\Omega = 4\pi$, so the geometric efficiency is $\epsilon_{geom} = 1$. The probability to detect all the gammas emitted in the same Gd decay is P = 1, assuming an intrinsic efficiency for the detector $\epsilon = 1$, and they will be 'seen' by the detector as one $\sim$ 8 MeV gamma (the sum of all the energies).

In reality, for this experiment the intrinsic efficiency for the scintillator blocks is less than one, and it will decrease with increasing gamma energy. This is because there is a finite probability for gamma to escape without detection.

However, the probability to detect the $E \sim 1$ MeV gamma simultaneously with the

- ~ 2.7 MeV gamma (transitions 3 and 4 from Fig. 3.4),

  or the

- ~ 5 MeV gamma (transitions 5 and 6 from Fig. 3.4);

is four times higher than in the previous experimental arrangement and both gammas will be 'seen' by the detector as one higher energy gamma.
This is a much more satisfactory situation.

Therefore for this experimental arrangement the peak due to the 1 MeV gammas from Gd decay is reduced considerably.

Figure 5.15 shows the neutron capture spectrum measured with the experimental arrangement described in Fig. 5.4. The spectrum is obtained using the same procedure as before, namely by subtracting the spectrum measured with the ^{241}Am/Be source without Gd from the spectrum measured with the ^{241}Am/Be together with the Gd paper.

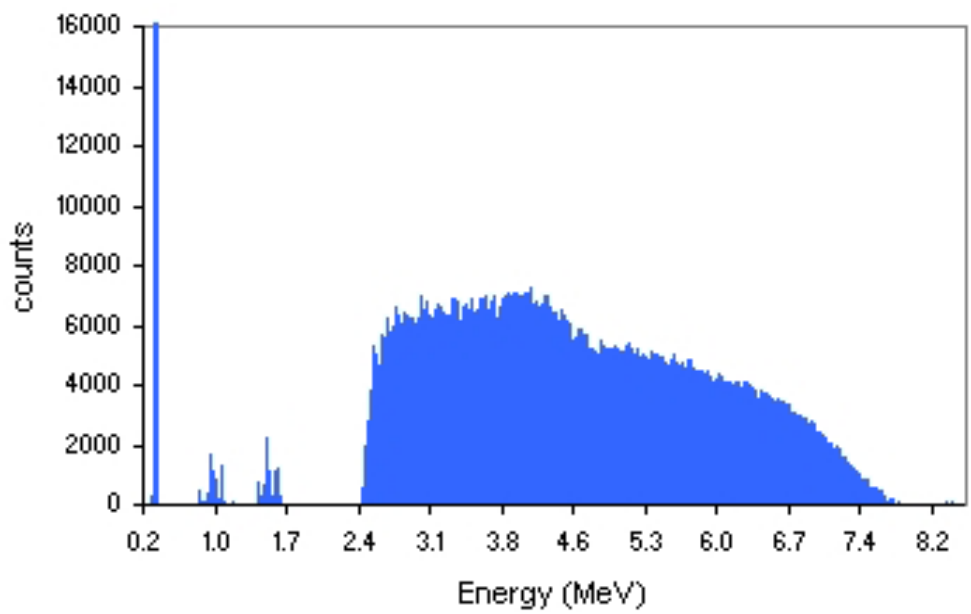

Figure 5.15: Neutron capture gamma spectrum measured with the Gd paper surrounded by the scintillator blocks

This gamma energy spectrum (Fig. 5.15), consists in a continuum from 2.4 MeV to 4.6 MeV, which is due to the gammas inside the continuum region of the spectrum measured by Groshev (Fig. 3.3) which are detected simultaneously with the ~ 1 MeV gammas from Gd.

A second continuum from 5 MeV to 8 MeV is due to the detection in coincidence of the ~ 5 MeV and the ~ 1 MeV gammas from Gd decay.

The two small peaks at ~ 1 MeV and ~ 1.6 MeV are due to the fact that even though the probability of detecting the $E \sim 1$ MeV gamma simultaneously with the ~ 2.7 or 5 MeV gamma is four times higher for this configuration of the detector, there is still a finite probability for the higher energy gamma to escape undetected and therefore only the ~ 1 MeV gamma to be observed in the Gd decay event.

Similarly, for a very large Gd loaded scintillator block the intrinsic efficiency will be maximum and the gammas will be *all* detected simultaneously. If the detector is large enough the gammas will deposit all their energy inside it and the neutron capture gamma spectrum would be reduced in this case to a photopeak corresponding to an 8 MeV gamma signal.

5.4 Conclusion

Large organic plastic scintillators have been tested in order to determine if they are suitable to be used in the OMNIS project.

Measurements of the light attenuation length have shown that the scintillators are suitable to be used in the OMNIS project and also that there was no significant degradation in their performance over the last $\sim$ 30 years.

The energy calibration of the detector showed that there is a linear relation between the pulse height and the energy deposited inside the detector over the energy range 0.5 - 4.5 MeV.

In order to determine the size of the detector which is needed to detect the total gamma energy ($\sim$ 8 MeV) from the neutron capture on gadolinium, a computation of the "gamma mean free path" for energy loss processes using the measured mass energy-absorption coefficient has been done. The conclusion was that approximately 600 mm of scintillator are needed in order to detect a significant fraction of the energy from the Gd (n,γ) reaction.

The energy spectrum of the gammas emitted following the neutron capture on Gd is analysed in some detail, for different configurations of the detector. The result was that the best configuration with respect to maximising the energy deposition inside the detector was the one having the Gd paper surrounded by scintillator blocks.

However for this experimental set up (Fig. 5.4) there are fewer neutron capture on Gd events than in the configuration with the Gd paper on top of the five scintillator blocks (Fig. 5.1). This is due to the fact that, in the first case, most of the neutrons are captured inside the top two blocks of scintillators (180 mm thick) and therefore will not reach the Gd paper.

Theoretical computations of the optimum size of the moderator needed to thermalize the neutrons are in good agreement with the experimental results which show that the optimum depth of moderator is $\sim$ 60 mm. A compromise between the optimum thickness of moderator needed to thermalize the neutrons and the depth

of scintillator required to detect the high energy gammas emitted in the Gd decay has been found.

To summarise, the scintillators were tested and it has been shown that they are suitable for use as neutron detectors in the OMNIS project. Both the 2.2 MeV gammas from neutron capture on protons inside the scintillators and the gammas emitted following the neutron capture on Gd are clearly seen and provide a clean signature for neutrons.

Chapter 6

Full Detector Simulation Using GEANT4

6.1 Introduction

The GEANT4 [61] simulation package was adapted to carry out a full simulation of the gamma and neutron interactions inside the detector and to model the detector response to incoming radiation.

Although GEANT4 is normally considered to be a tool to simulate large detectors, it is also suitable for simulating more simple configurations like this detector. Previous studies within our group have modelled the production of supernova neutrinos, the transport of neutrinos to Earth and the production of neutrons on various nuclear targets. The aim is to use GEANT4 to model the remainder of the chain, right up to the pulses emerging from the photomultipliers. These have been backed up when possible by measurement.

The neutrons were tracked from the source to the target cell scintillator and in the detector itself, for different size and geometry of the detector, in order to determine the optimum configuration of the detector with respect to neutron detection efficiency.

6.2 General Parameters of the Simulation

6.2.1 The Detector Geometry

The geometry of the neutron detector has been modelled in detail. Five target cells are individually placed in order to reproduce the experimental arrangement shown in Fig. 5.1. The cells were then 'filled' with vinyltoluene (91.6% C and 8.4% H by weight), with a density $\rho = 1.032\, g/cm^3$ (see Appendix). The volume of each cell was defined to be $0.18 \times 0.18 \times 2m^3$, allowing a gap of 6 mm between the 'top' two and the 'bottom' three cells.

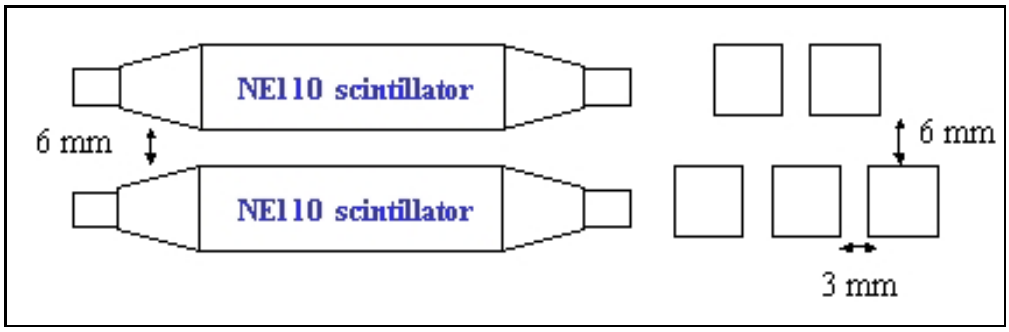

Figure 6.1: The detector geometry used in the simulation (the figure is not to scale)

6.2.2 The Tracking

GEANT4 performs the tracking of charged particles and simulates the electromagnetic interactions inside the detector and the hadronic interactions and the tracking of neutrons.

The cross-section data for the hadronic processes are contained in a separate component, G4NDL3.7, which is based on a number of Evaluated Nuclear Data Libraries. Interaction cross-sections are tabulated and calculated within GEANT4 and G4NDL3.7 for the materials defined by the user. In GEANT4, several standard materials are defined. However the user can define his/her own materials to be used in the simulation, by specifying their chemical makeup, like, in this case the scintillator itself, water and paraffin wax.

GEANT4 allows the tracking of gammas and charged particles down to a threshold energy of 10 keV, at which point the particle is considered to have deposited all its energy inside the detector and is then discarded. On the other hand, G4NDL3.7 allows the tracking of neutrons from 20 MeV down to thermal, an obvious requirement since these are neutrons in which we are most interested.

6.2.3 The Physics List

A novice example (number 3) is provided by GEANT4 to simulate the interactions of any particle inside a simple calorimeter, by calculating the energy deposited by the particle inside the detector. This code was modified in order to reproduce the detector in Fig. 5.1 and to simulate the interactions of gamma rays inside the scintillator.

The electromagnetic interactions of leptons, gammas, hadrons and ions are managed by GEANT4 electromagnetic package, organised as a set of class categories [62]:

- *standard*, handling basic processes for electron, positron, gamma and hadron interactions;
- *low energy*, providing alternative models extended down to lower energies than the standard category;
- *muons*, handling muon interactions;
- $X - rays$, providing specific code for x-ray physics;
- *optical*, providing specific code for optical photons;
- *utils*, collecting utility classes used by the other categories.

The only class category which was included in the physics list of the simulation code is the class of *standard* physics processes, which produces the energy loss due to electromagnetic processes for any particle inside any type of material. It also handles the hadronic processes inside the detector and the tracking of the neutrons.

6.3 The Simulated Gamma Response of the Detector

6.3.1 The Deposited Energy inside the Detector

In all simulations, 10^5 gammas were tracked, measuring the energy deposited by each gamma inside the detector. The gamma energies were chosen to match those used to calibrate the detector(see Table 4.3).

The energy scale of the detector response spectrum was calibrated using the Compton edges of different known gamma sources.
A detailed description of this calibration method, including the procedure of assigning energy values to features of the Compton spectrum, is described in Section 4.4.
The detector would normally be calibrated once or twice a month during the running of the experiment, using the gamma sources described in Table 4.3. Since these gammas are relatively low energy and are not very penetrating (see Table 4.5), they will often deposit all their energy inside the detector.

For the scintillator block described in Fig. 4.12 the gammas will frequently undergo multiple Compton scattering, thus depositing a significant amount of energy beyond the Compton edge of 0.478 MeV, as shown in Fig. 6.2.

The first peak at 0.478 MeV represents the Compton edge of the gammas emitted by the ^{137}Cs source. The scintillator block is thick enough for the gammas to suffer multiple Compton scattering processes, in which case the sum of the energy loss in each scattering will produce the second broader peak.
Approximately 2% of the gammas entering the scintillator will multiple scatter until their whole energy is deposited, process leading to the final photoabsorption. These events will produce the photo-peak, at an energy equal to the gamma energy. This is the spike at 0.662 MeV in Figure 6.2.

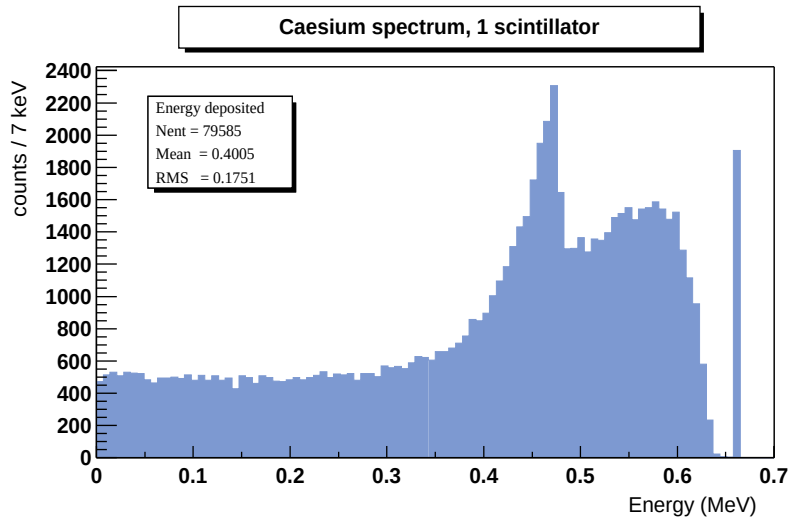

Figure 6.2: The energy deposited inside 1 scintillator (Fig. 4.12) by the gammas from the ^{137}Cs source for a perfect energy resolution

However the energy spectrum of the gammas emitted by the ^{137}Cs source has been measured (see Fig. 4.18), and shows only one broad peak. This is due to the finite energy resolution of the detector, caused by the statistical fluctuations in the number of photoelectrons produced following the deposition of energy inside the detector.

It was the aim of this investigation to simulate the resolution due to the statistics so that the spectrum in Fig. 6.2 resembled that shown in Fig. 4.18. If this can be done, then we will have demonstrated that the resolution for single gammas is understood. This will allow us to understand and determine the resolution and hence detection efficiency for multiple gamma collection.

In Section 4.5.2 the energy resolution for one scintillator block was measured to be $R^{exp}_{1scint} = 23.2 \pm 1.6\%$ (see Equation 4.20), for a deposited energy corresponding to the Compton edge of the gammas emitted by the ^{137}Cs source, i.e. $E_{deposit} = 0.478 MeV$.

Therefore, using Equation 4.9, for a deposited energy equal to the energy of one gamma $E_\gamma = 0.662 MeV$, the energy resolution will be equal to:

$$R(E_\gamma) \approx 19.7\% \tag{6.1}$$

For each deposited energy calculated in the simulation, $E_{deposit}$, fluctuations were applied, approximated by a Gaussian with standard deviation:

$$\sigma = \frac{R(E_\gamma)(\%)}{235}\sqrt{E_{deposit}\,E_\gamma} \tag{6.2}$$

After the gaussian convolution of the energy spectrum in Fig. 6.2 has been performed, the result showed that the three peaks combined to produce a single broad peak (Fig. 6.3).

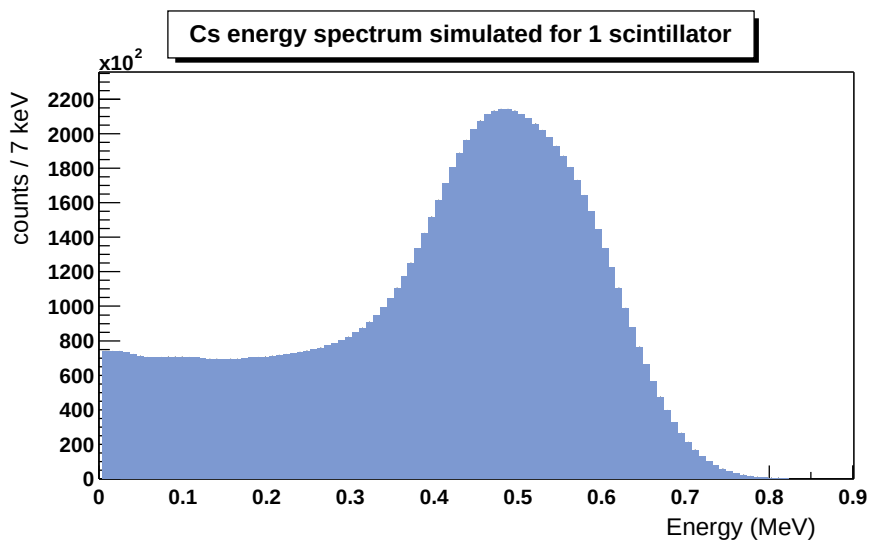

Figure 6.3: The simulated energy spectrum of the ^{137}Cs source

This result is significant. Without GEANT4, the measured peak in Fig. 6.3 was always associated with a single Compton Edge. Instead, it corresponds to the complex structure in Fig. 6.2. Furthermore, the complexity of the spectrum shown in Fig. 6.2 depends strongly on the thickness of the scintillator. GEANT4 is therefore a critical tool in the simulation process.

6.3.2 The Detector Energy Resolution

As the number the scintillator blocks used is increased, the signal pulse amplitude will depend on the position of the radiation interaction throughout the detector due to nonuniformities in the light collection. These nonuniformities are caused by the fact that each scintillator has its own light yield for a given deposited energy. Thus, as the number the scintillator blocks used is increased, the energy resolution of the detector becomes worse than 23.2%, the value that was obtained for one scintillator (see Eq. 4.20).

Because of differences in the length of scintillator traversed and the solid angle to the phototubes, the amount of light collected by the PMT's for a given deposited energy will depend on the position of the interaction of the gamma ray in the cell. This position dependence will result in an additional energy smearing when the energies deposited everywhere in the large detector are integrated at the photomultiplier tubes.

The dependence of the Compton edge position on the distance from the centre of the detector is shown in Fig. 4.15.

The detector geometries which will be considered are five scintillators - two blocks on top of three (see Fig. 6.1) and four scintillators - two blocks, as before, on top of another two. The reason for this choice is that it was possible to construct these geometries with the available number of scintillator blocks. They are sufficiently different that if the simulation agrees with the measurement for both cases, then this will give confidence that the simulation package can be used to predict more complex arrangements, rather than go to the effort and expense of making them. We shall then be able to converge on a working detector using GEANT4.

The Energy Resolution for Four Scintillators

For more scintillator blocks one would expect an increase in the number of gammas which will deposit all their energy through multiple Compton scattering, compared

with the value of 2% obtained in the case of only one scintillator (see Fig. 6.2). The energy deposited by the 0.662 MeV gammas inside four scintillator blocks is shown in the histogram in Fig. 6.4.

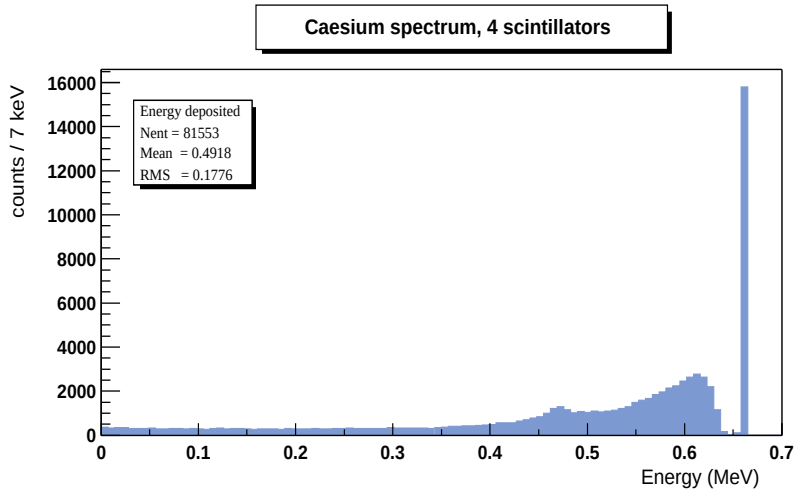

Figure 6.4: The energy deposited inside 4 scintillators by the gammas from the ^{137}Cs source for a perfect energy resolution

In this case, the simulation showed that approximately 15.9% of the gammas entering the scintillators deposit all their energy inside the detector, i.e. the spike at 0.662 MeV.

The method used to determine the energy resolution of the detector for four and five scintillators respectively, was to compare the experimental measurement of the energy spectra of the gamma sources with the ones predicted by the simulation. Gaussian convolutions of the simulated spectra were performed for different values of standard deviations in order to determine what value results in the best fit.

For four scintillator blocks the best fit between simulated (Fig. 6.4) and experimental data was found (see Fig. 6.5) for an energy resolution of:

$$R_{4scint} \approx 28\% \tag{6.3}$$

for a deposited energy $E_{deposit} = 0.662MeV$.

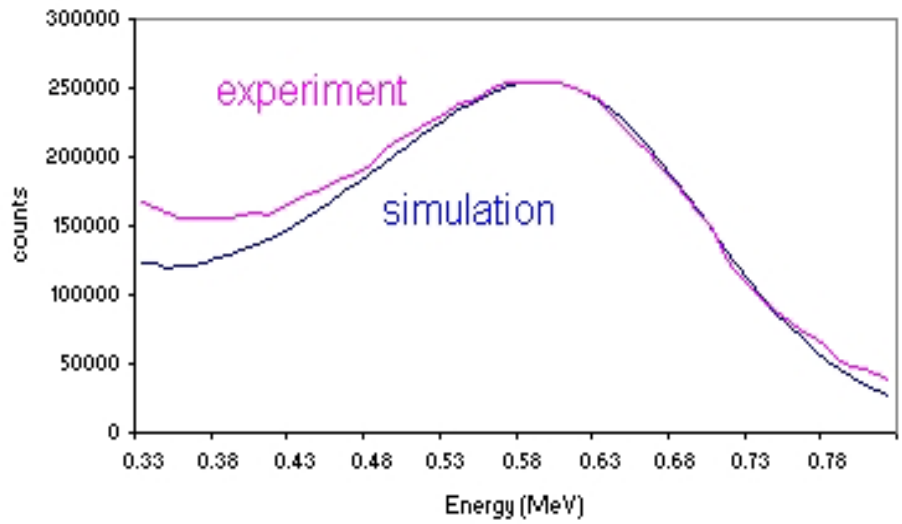

Figure 6.5: Comparison between simulation and experimental measurement of the response of the four scintillators to the ^{137}Cs source, for an energy resolution $R = 28\%$, with background included

The discrepancy at low energies is due to the fact that the gamma sources will cause additional contribution to spectra which will not be subtracted during the background subtraction. In order to analyse this effect, the background measured experimentally (see Fig. 6.6) was split into two parts (Fig. 6.7): the signal from the ^{40}K contained in the glass of the PMT's and the 'electronic noise'.

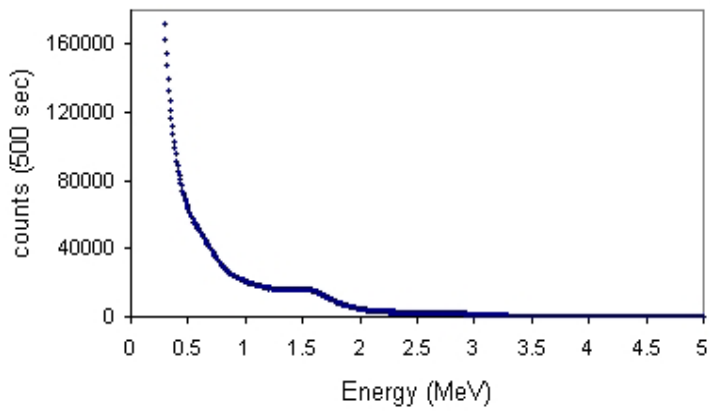

Figure 6.6: Background measurement

This signal due to the ^{40}K is not affected by the presence of the external gamma source. It is only the 'electronic noise' component of the background which will be higher when the gamma source is used.

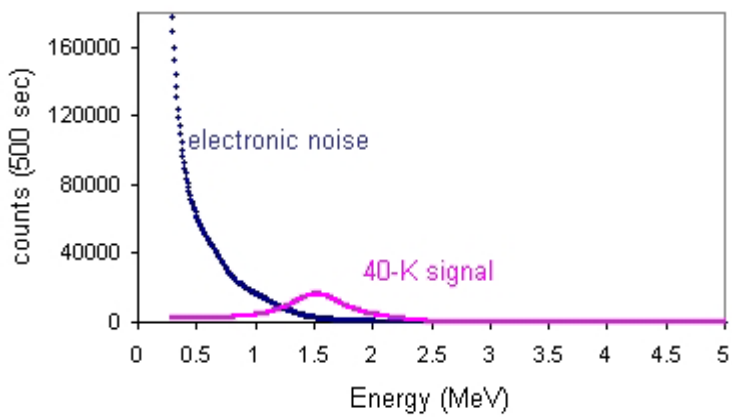

Figure 6.7: Measured background split into ^{40}K signal and 'electronic noise'

The peak due to the ^{40}K is clearly seen in Figure 6.7.

For the ^{137}Cs source spectrum measurement the MCA dead time (which is composed of the processing time of the ADC and the memory storage time [58]) is equal to ~45%. From the experimental data it was found that, when an external gamma source is used, the 'electronic noise' component of the background is increased by a

factor f given by following formula:

$$f = \frac{1}{1 - \frac{dt}{100}} \tag{6.4}$$

where dt is the MCA dead time (percentage). For the ^{137}Cs spectrum measurement $f = 1.81$.

Therefore in all the simulations some additional background (noise) has been added to reproduce the experimental data, proportional to the parameter f defined in Equation 6.4.

The following figure shows the comparison between the simulated and the experimentally measured ^{137}Cs energy spectrum, after the additional background (noise) has been added to the simulation.

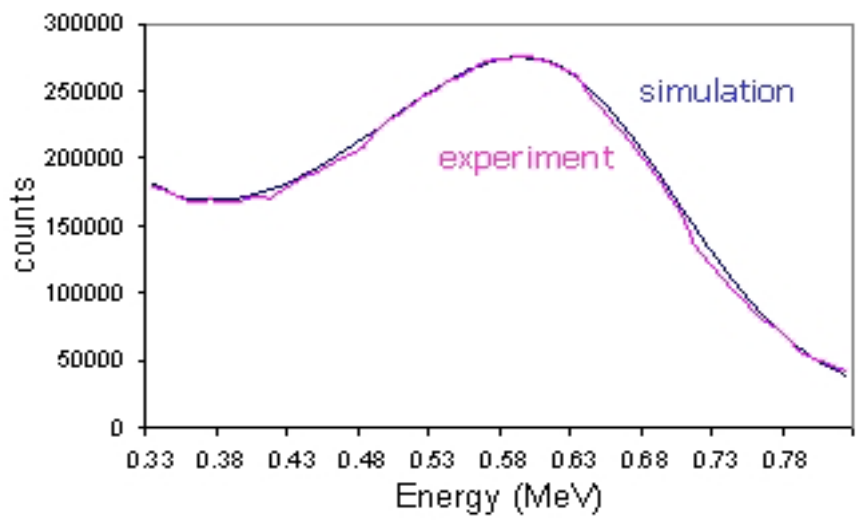

Figure 6.8: Comparison between simulation and experimental measurement of the ^{137}Cs energy spectrum, for an energy resolution $R = 28\%$, with additional background (noise) included in the simulated spectrum

The simulation thus gives a good overall description of the data when the 28% energy resolution parameter is used.

The same energy resolution of 28% was considered for the gaussian convolution of the energy deposition spectrum of the ^{60}Co source, which emits 1.173 and 1.332 MeV gammas (see Table 4.4).

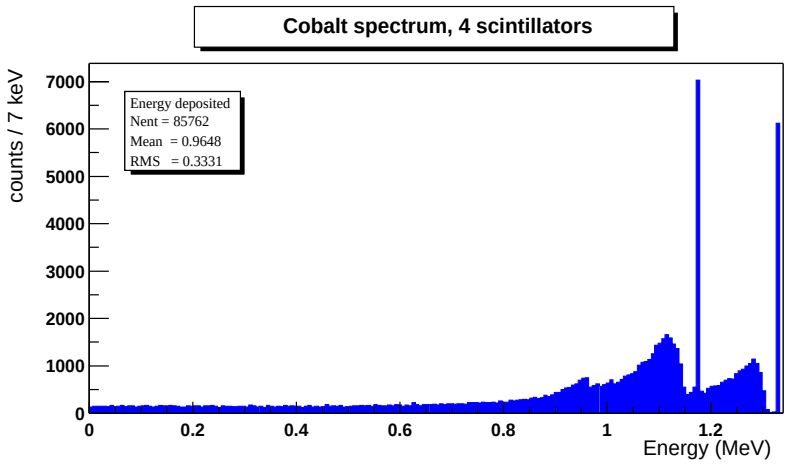

Figure 6.9: The energy deposited inside 4 scintillators by the gammas from the ^{60}Co source for a perfect energy resolution

After the gaussian convolution of the simulated prediction of the detector response to the ^{60}Co source, the result proved to be in good agreement with the experimental measured spectrum (see Fig. 6.10).

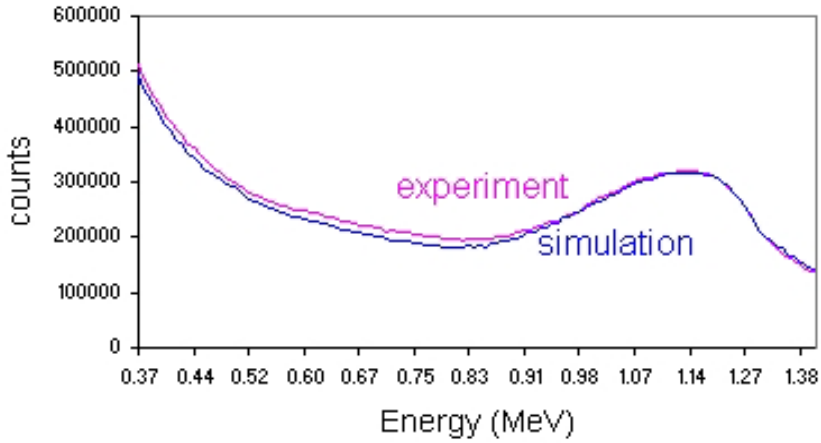

Figure 6.10: Comparison between the simulated and experimental data for four scintillators, of the detector response to the ^{60}Co source, for an energy resolution R = 28%, with background included

Following the same procedure as before additional background (noise) has to be added to the simulated spectrum. However due to the fact that for the ^{60}Co source spectrum measurement the MCA dead time was equal to only $\sim$ 14% compared to $\sim$ 45% for the ^{137}Cs source spectrum measurement, the factor f defined in Equation 6.4 is equal in this case to 1.16.

The following figure shows the comparison between the simulated and the experimentally measured ^{60}Co energy spectrum, after the additional background (noise) has been added to the simulation.

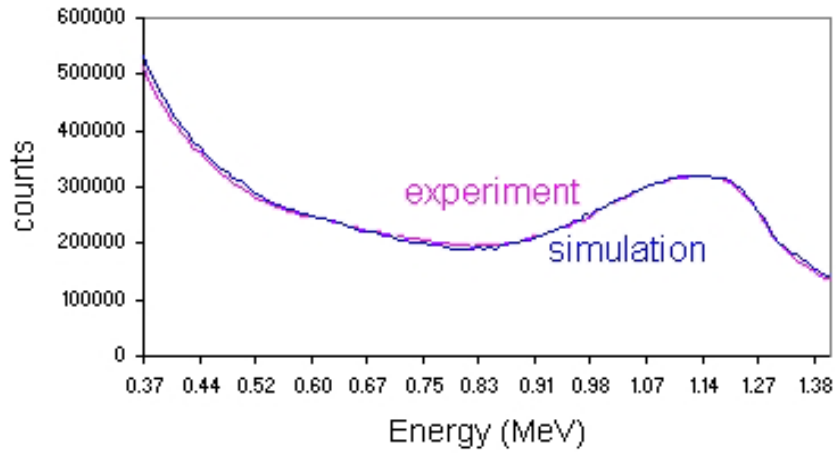

Figure 6.11: Comparison between the simulated and experimental data for four scintillators, of the detector response to the ^{60}Co source, for an energy resolution R = 28%, with additional background (noise) included in the simulated spectrum

It is worth mentioning here that due to the increase in the fraction of events in the photo-peak for this number of blocks, the peak position in Figures 6.8 and 6.11 *has exceeded* the Compton edge energy of 0.478 MeV and 1.038 MeV respectively. Therefore, the assignment of the Compton edge to the 90% of the maximum value which used for the energy calibration of one scintillator (see Fig. 4.18 - 4.21) is no longer correct for more than one scintillator. The GEANT4 simulation was used to calculate the energy associated with the maximum point of the Compton continuum for each gamma source used in the calibration process, which is needed for a correct re-calibration of the detector. This is a much safer procedure.

The following figures (6.12 - 6.17) show the simulated and measured spectra for the three gamma sources used for the calibration of the detector.

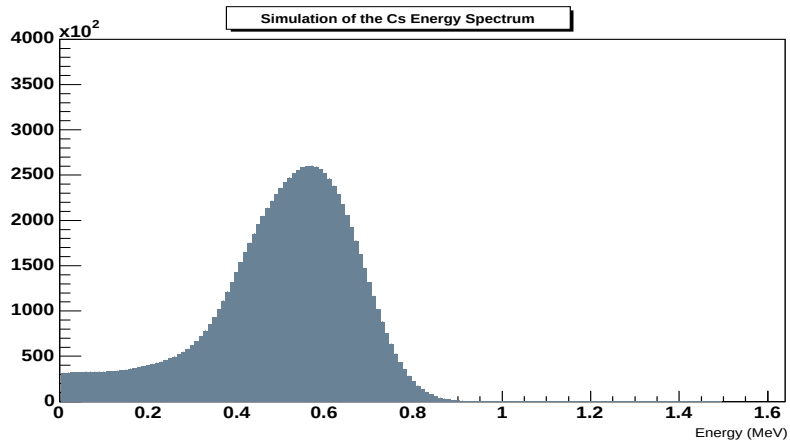

Figure 6.12: The energy spectrum of the ^{137}Cs source simulated for 4 scintillators (maximum at 0.588 MeV)

Figure 6.13: Energy spectrum of the ^{137}Cs source measured with the 4 scintillators

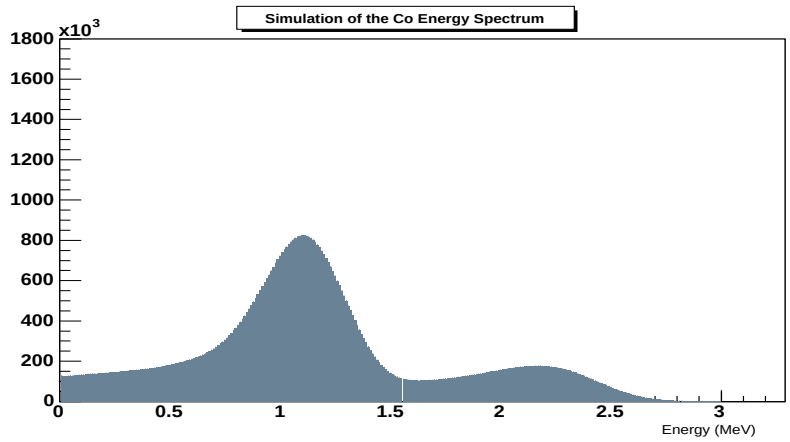

Figure 6.14: The energy spectrum of the ^{60}Co source simulated for 4 scintillators (maximum at 1.139 MeV)

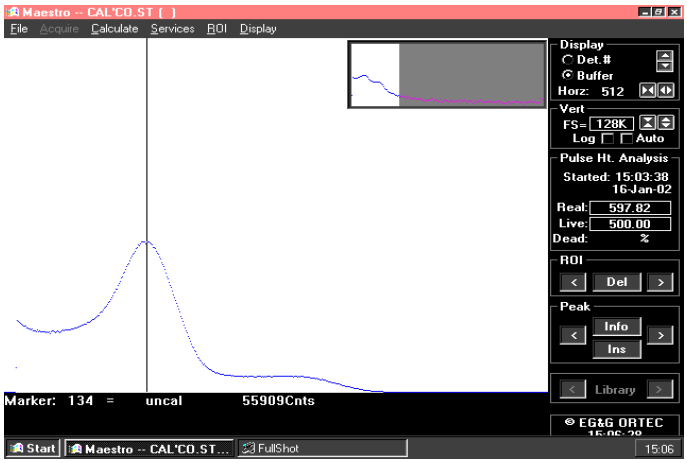

Figure 6.15: The energy spectrum of the ^{60}Co source measured with the 4 scintillators

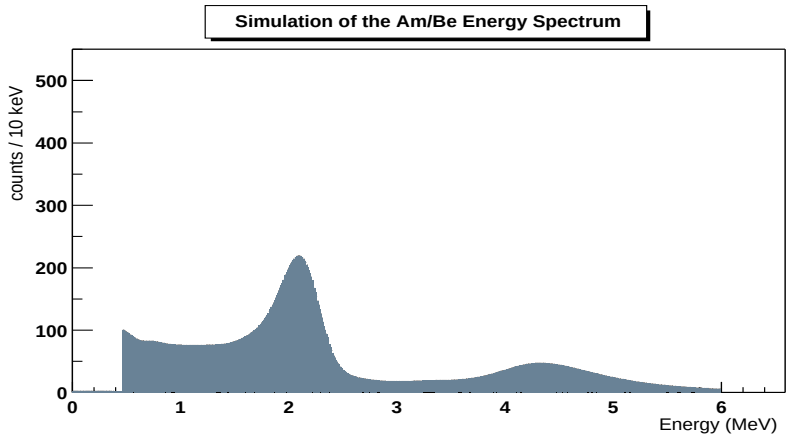

Figure 6.16: The energy spectrum of the ^{241}Am/Be source simulated for 4 scintillators (maximum at 2.1 MeV and 4.25 MeV respectively)

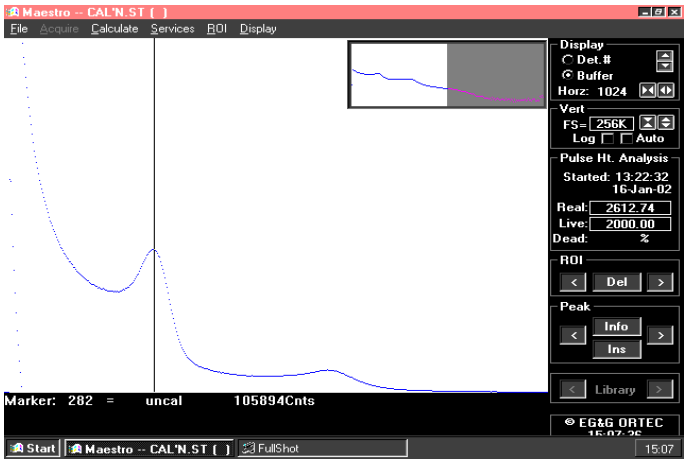

Figure 6.17: The energy spectrum of the ^{241}Am/Be source measured with the 4 scintillators

The Energy Resolution for Five Scintillators

The investigation was now extended to five scintillators. The simulation of the interactions of the 0.662 MeV gammas inside the five scintillator blocks resulted in the energy spectrum shown in Fig. 6.18.

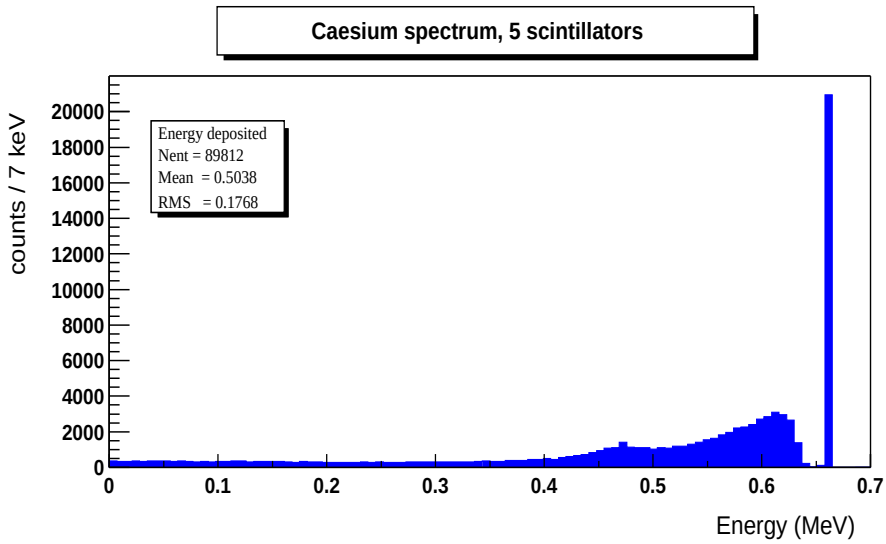

Figure 6.18: The energy deposited inside 5 scintillators (Fig. 5.1) by the gammas from the ^{137}Cs source for a perfect energy resolution

In this case approximately 20% of the gammas entering the scintillator will deposit all their energy inside the detector.

The best fit with the experimental data was obtained for an energy resolution

$$R_{5scint} \approx 35\% \tag{6.5}$$

as shown in the following figure:

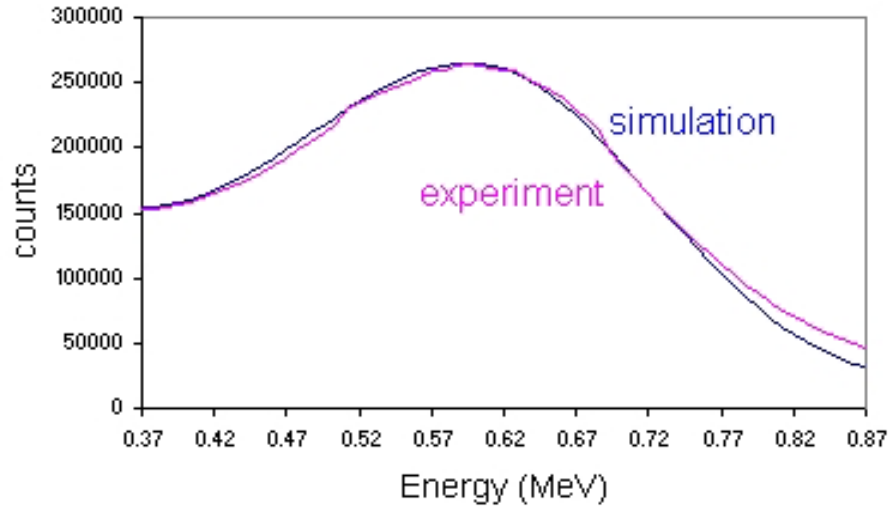

Figure 6.19: Comparison between simulation and experimental measurement of the response of the five scintillators to the ^{137}Cs source, for an energy resolution R = 35%, with background included

The 35% energy resolution corresponding to a deposited energy of 0.662 MeV is much worse than the 28% value obtained for the four scintillator blocks. As mentioned before, this is due to the nonuniformities in the light collection from different scintillator blocks. These nonuniformities were caused by the differences between the light output versus deposited energy for the different scintillators. Even though the high voltage on each photomultiplier tube was adjusted such that the measured position of the maximum of the Compton continuum in the ^{137}Cs source spectrum was the same when measured with each scintillator, the response of the different scintillators will be the same only for this particular chosen deposited energy. For example the maximum of the Compton continuum in the ^{60}Co (or ^{241}Am/Be) spectrum will still differ from scintillator to scintillator.

Therefore adding one more scintillator block will increase the fraction of deposited energy but it will also affect the energy resolution of the detector. A compromise between the detector size, i.e. the number of scintillator blocks, and the energy resolution is therefore required.

The simulated spectra were independently normalised to the activity of the gamma

sources. With this adjustment, the simulated response of the detector to gammas and spectral shape agree well with the measured values.

The gamma detection efficiency varied from 79.6% for one scintillator to 93.9% for five scintillators. Here the detection efficiency is defined as those gammas which are detected expressed as a fraction of all those entering the scintillators.

6.4 Calibration of Neutron Detection Efficiency

The GEANT4 simulation package [61] was also used to model the interaction of neutrons in the proposed prototype detector for the OMNIS experiment.

When GEANT4 was first used, it was evident that when neutrons are sent into Gadolinium, a single gamma of about 8 MeV is produced (see Fig. 6.20), whereas there should be several gammas with a total energy equal to the neutron binding energy inside the resulting Gd isotope. In other words, the package did not contain the actual (extremely complex) gadolinium decay scheme.

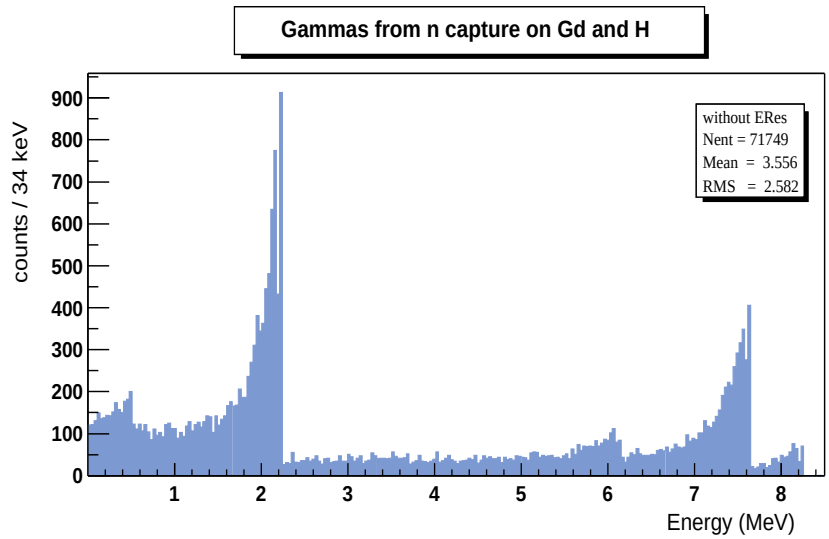

Figure 6.20: The simulation of deposited gamma energies from neutron capture on Gd and H

The data which are available in GEANT4 seem to be only cross-section information [63], as the level scheme of ^{158}Gd, the isotope with the highest neutron capture cross-section, is not completely catalogued, and many of the emitted gamma rays are unresolved (see Fig. 3.4).

Therefore, in order to gain experience only the capture on hydrogen was considered initially in the simulation process. The neutron thermalizes inside the scintillator

and either escapes the detector volume or is captured on hydrogen in the scintillator. The capture on hydrogen results in the emission of a single 2.2 MeV gamma. The production and detection of this single gamma should be easier to understand.

The probability of neutron detection, ϵ_n, can be expressed as a product of two factors:

$$\epsilon_n = \epsilon_c \cdot \epsilon_\gamma \tag{6.6}$$

where ϵ_c is the neutron containment efficiency, i.e. the probability that the neutron will not leak out of the detector volume, and ϵ_γ is the detection probability of the 2.2 MeV gamma.

Different numbers of target cells described in Fig. 4.12 and different geometries were considered in order to determine the optimum configuration of the neutron detector. The neutrons were tracked through the detector and in the case of neutron capture, the deposited energy of the 2.2 MeV gamma was measured.

Figure 6.21 shows a schematic diagram of a proposed neutron detector which could be installed at the Boulby Mine.

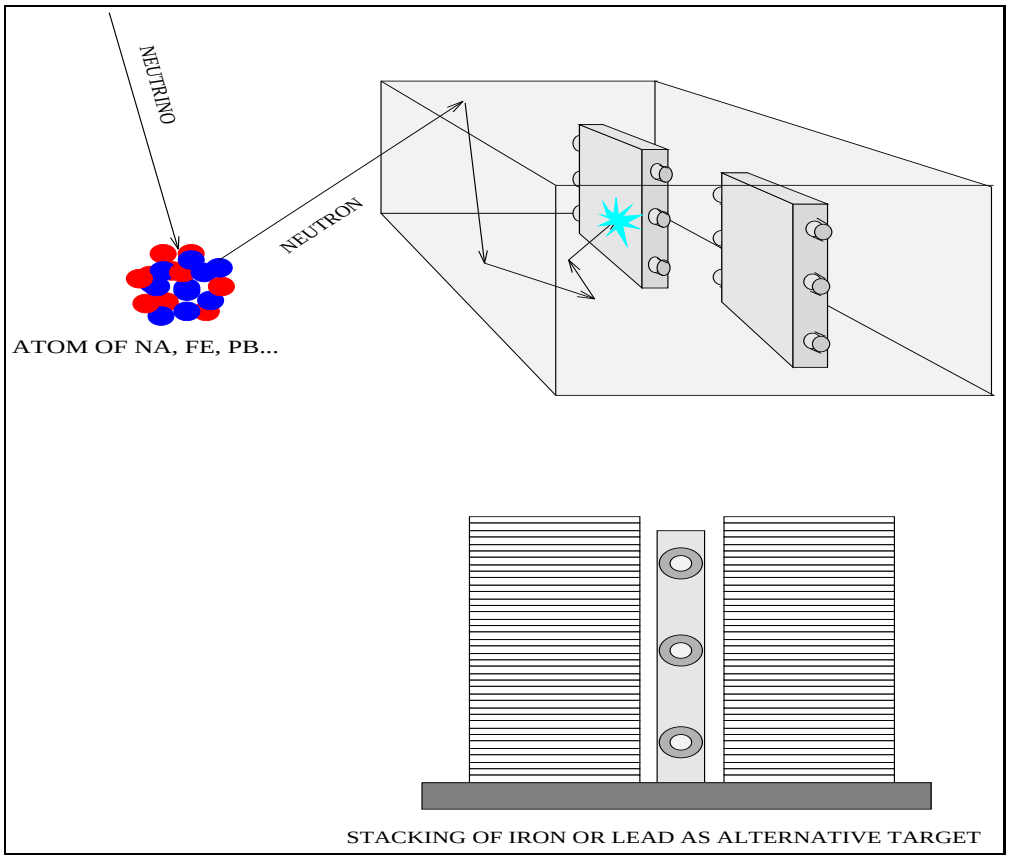

Figure 6.21: Schematic diagram of the proposed OMNIS detector

In the simulation program, the neutrons were generated towards the detector from a source positioned randomly on a sphere with a radius of 10 metres, with the detector at the centre of the sphere. Up to 16 scintillator blocks were considered in this simulation.

The neutron detection efficiency increased with the number of cells in the detector, from 7.5% for one scintillator cell to 30.7% for 16 cells, as shown in Fig. 6.22 and 6.23. These figures show the energy deposited in the scintillators from a total of 100,000 generated neutrons.

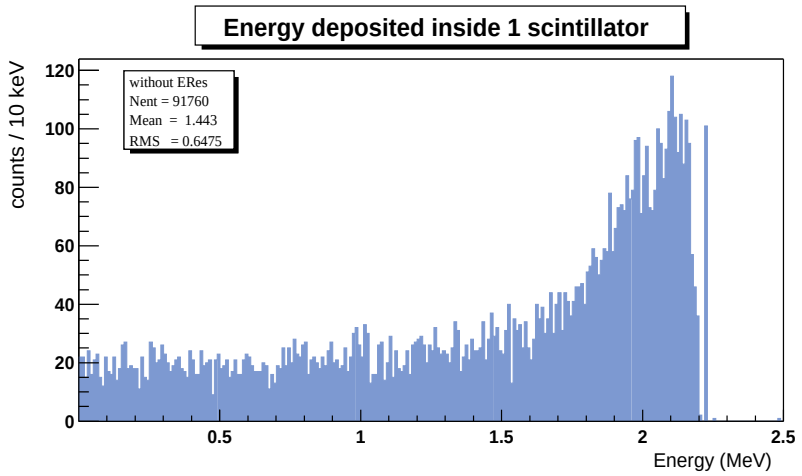

Figure 6.22: Energy deposited by the 2.2 MeV gamma from neutron capture on hydrogen inside one scintillator

From the 100,000 neutrons entering the scintillator, only 7,504 will deposit energy which will result in a detection signal. When 16 scintillators are simulated, the number of neutrons that are detected increases from 7,504 (for 1 scintillator) to 30,687, as shown in Figure 6.23.

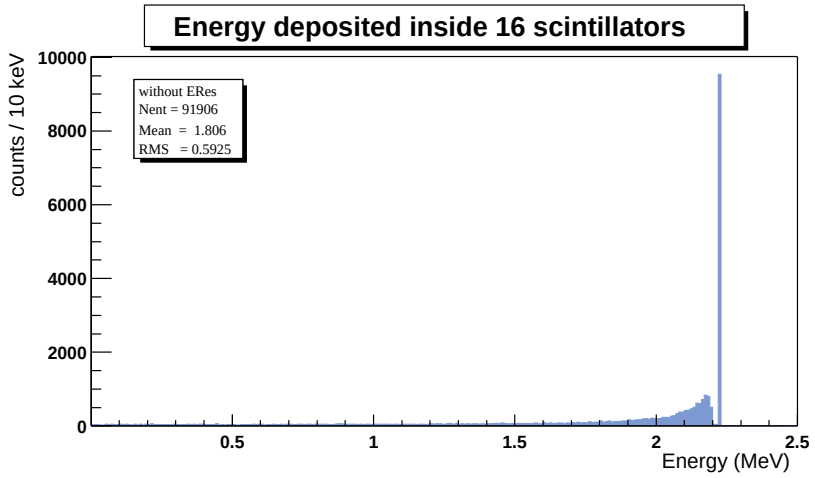

Figure 6.23: Energy deposited by the 2.2 MeV gamma from neutron capture on hydrogen inside sixteen scintillators

These plots have no detector resolution built in and if one would normally measure with an energy threshold, the 7.5% efficiency will certainly decrease whereas the

30.7% may well be unaffected.

As expected, the 2.2 MeV gammas which are produced following the neutron capture on hydrogen also deposit more energy inside the bigger detector, increasing from $\sim$ 1.3% gammas depositing all their energy inside one scintillator to 30.9% events in the photopeak for 16 scintillators.

The dependence of the neutron detection efficiency on the number of cells in the detector and the corresponding geometries is shown in Fig. 6.24.

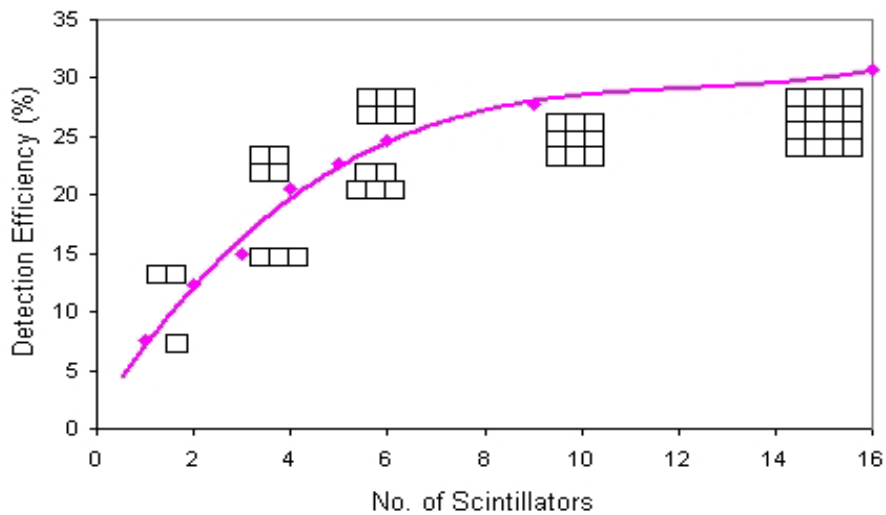

Figure 6.24: Neutron efficiency as a function of geometry and number of cells

It can be seen that there is a saturation point in the detection efficiency at $\sim$ 28%, for a number of nine cells, which proves to be the optimum configuration of the neutron detector.

Even by removing the central cell from the 9 scintillators array, the neutron efficiency does not change by more than 2% (Fig. 6.25), which is due to the fact that the neutrons are thermalized and captured in the first 60-80 mm of scintillator(see Section 5.2), the scintillator being also a neutron moderator with a neutron mean free path $\lambda = 28$ mm, which was calculated using the ratio of the number of H atoms per cm^3 inside the scintillator and another moderator, for which the neutron mean

free path is known (e.g. light water). This provides a means to make optimal use of the scintillator blocks. With a 3×3 array, 11% of the scintillator is wasted.

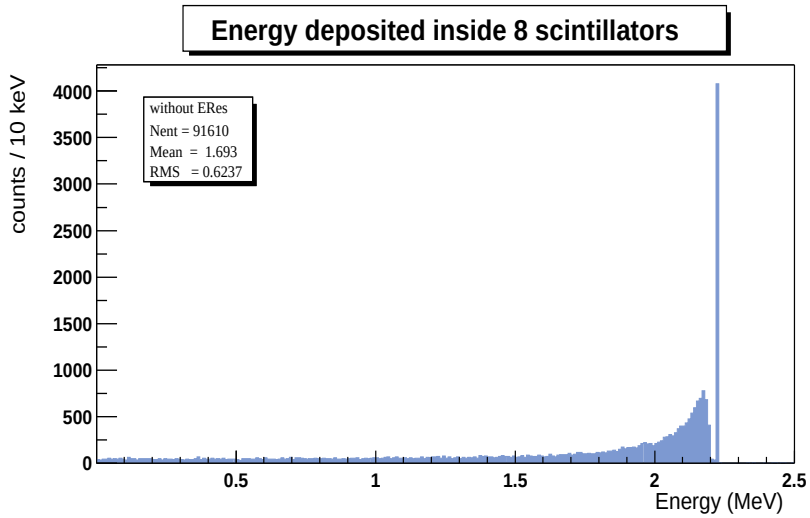

Figure 6.25: The neutron detection efficiency for the optimum geometry configuration, without the central cell: 26,077 neutrons detected from 100,000 entering the scintillator

The neutron detection efficiency was calculated for the 9 cell detector geometry, also for the case where gadolinium is loaded into the scintillators.
The neutron capture probability depends on the capture cross-section and the gadolinium and hydrogen number densities in the plastic scintillator. The following table summarises the composition of the Gd-loaded scintillators used in the simulation.

Element	Atomic Weight	Mass Fraction	Number Density (cm^{-3})
C	12.001	91.55%	4.74×10^{22}
H	1.0079	8.35%	5.19×10^{22}
Gd	157.25	0.1%	3.95×10^{18}

Table 6.1: Composition of Gd-loaded Scintillator

The thermal neutron capture cross-section on gadolinium is 49,700 barns, on hy-

drogen 0.328 barns, and on carbon, a negligible 3×10^{-3} barns. Multiplying the cross-section with the number densities yields the macroscopic capture cross-sections for this Gd loaded scintillator: for capture on Gd, $\Sigma_{Gd} = 0.196\,cm^{-1}$, and on protons, $\Sigma_H = 0.017\,cm^{-1}$. This immediately gives the probability that the neutron to be captured on gadolinum, rather than on a proton: $\epsilon_{Gd} = 92\%$.

However, adding Gd to the scintillator does not affect the neutron detection efficiency, as shown in the following figure. Only the energies of the resulting gammas, following the neutron capture will differ, the detection efficiency being equal to 26.9%.

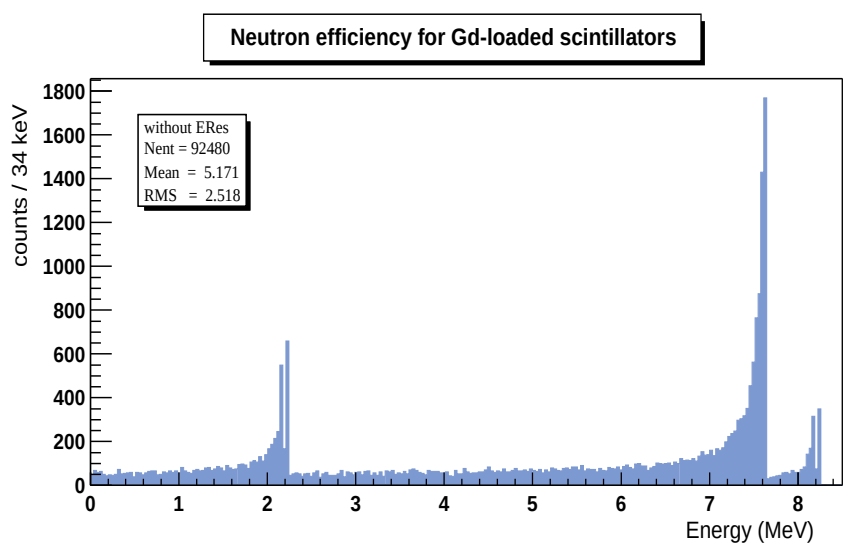

Figure 6.26: The neutron detection efficiency for Gd-loaded scintillators: 26,863 neutrons detected from 100,000 entering the scintillator

When only organic plastic scintillators without Gd are used, $\sim 27\%$ of the neutrons entering the scintillators will be thermalized and captured on protons. In the case of Gd loaded scintillators the same fraction of neutrons will be thermalized but then, from the 27% of thermalized neutrons, 92% will be captured on Gd and only 8% on protons.

6.5 Implementation of Previous Parametrisations of the Gd Spectrum into the GEANT Simulation

Even today the most useful measurement of the gamma energy spectrum from natural Gd is still the relatively old work of Groshev et al. [64], using a magnetic Compton spectrometer. This is the only measurement that provides the relative intensities of both the resolved gamma energy lines to the low-lying levels and to the unresolved continuum of the final nuclei (see Fig. 3.4). The measured energy spectrum published by Groshev et al. is displayed in Fig. 3.3.
In the more recent works, e.g. Refs. [65, 66, 67] for ^{156}Gd and Refs. [68, 69] for ^{158}Gd, performed with Ge(Li) and/or crystal diffraction spectrometers, there is no information on transitions from capture state to continuum [49].

Using the relative intensities of the γ-ray lines, Trzcinski et al. [49] have parametrised the transitions from the capture state directly to the discrete states. Above the energy denoted E_{cut} the data is partly or completely missing. Therefore the Gilbert-Cameron level-density formula [70] has been used by Trzcinski et al. to obtain the continuous distribution of energy levels.

Efficiency corrections to the measured data were required, taking into account the energy-dependent efficiency of the Compton spectrometer which was used, which made the experiment less sensitive to the lower energy gammas.
The efficiency-corrected gamma energy spectrum from ^{158}Gd, published by Trzcinski et al., is shown in figure 6.27. The ^{158}Gd isotope was selected because this is the isotope that is produced in the thermal radiative capture in ^{157}Gd, the isotope with the highest thermal neutron capture cross-section (see Table 3.3).

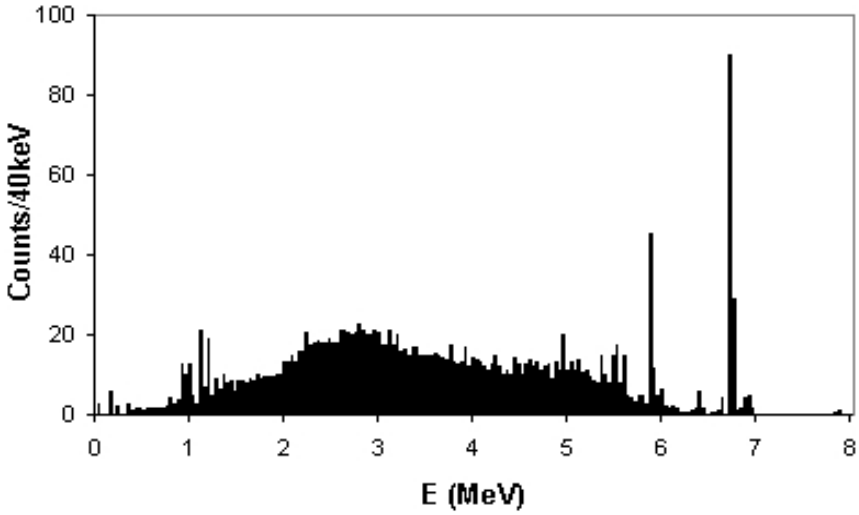

Figure 6.27: The efficiency-corrected calculated thermal neutron capture γ-ray spectrum from ^{158}Gd [49]

This calculated energy spectrum results in the following multiplicity distribution for γ-rays emitted by ^{158}Gd:

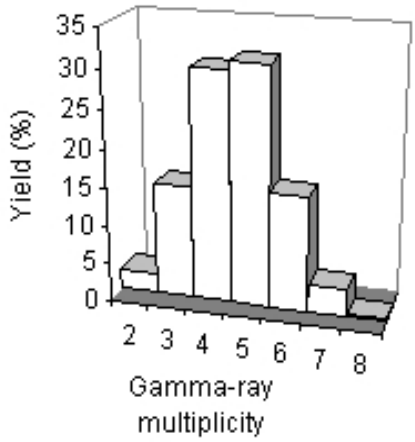

Figure 6.28: The calculated γ-ray multiplicity spectrum from ^{158}Gd [49]

The γ-ray multiplicity distribution predicts an average multiplicity of 4.5 quanta. This is an important characteristic of the capture spectrum, since the ratio of neutron binding energy to the most probable multiplicity gives the average γ-ray energy interacting with the scintillator.

The predicted average multiplicity of 4.5 gammas reflects the fact that, in this parametrisation of the Gd spectrum, the transitions from the capture state to the unresolved continuum exhaust nearly the entire transition strength.

In order to reproduce these decay characteristics and the experimental measured spectrum from Gd (Fig. 5.11) with the GEANT4 simulation, the geometry of the detector used in the experiment, consisting of five scintillators (see Fig. 5.1), was included into the simulation code (Fig. 6.1).
The parametrisation of the Gd spectrum in Fig. 6.27 was used to generate gammas, which were picked randomly from the above distribution until the sum energy reached or exceeded the excitation energy. At this point the last gamma energy was truncated such that the total energy in the cascade was 7.94 MeV. The results from the simulation of 100,000 Gd decays for this model of the gadolinium decay spectrum are shown in Figure 6.29. In this figure, the total energy deposited inside the scintillators in each Gd decay by the gammas entering the detector is shown, using an energy bin size of 10 keV.

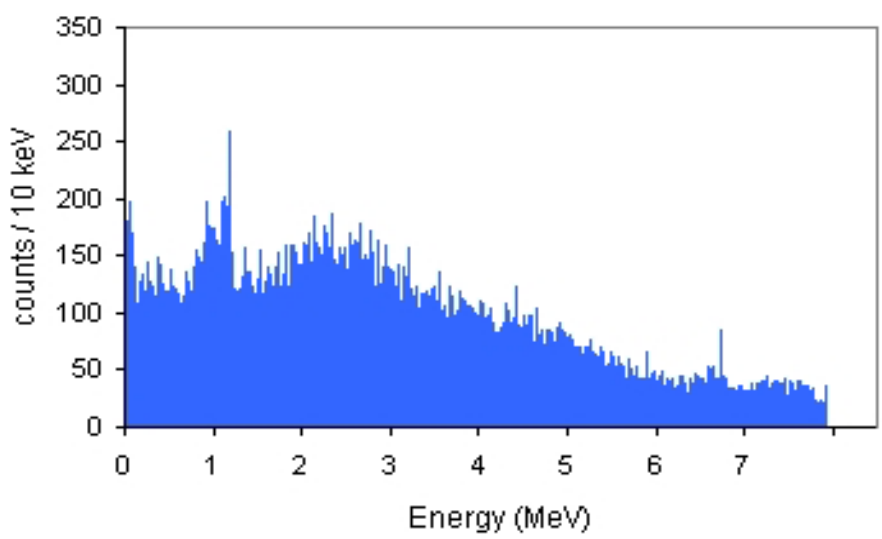

Figure 6.29: Simulation of the energy deposited by the gammas from neutron capture on gadolinium, using the parametrisation in Fig. 6.27.

In the real Gd data, there is a gap in the spectrum at $\sim$ 2 MeV (see Fig. 5.11),

that appears after the measurement without Gd is subtracted from the one with Gd. This is due to the fact that fewer neutrons will enter the scintillator when Gd is used, and this means that fewer 2.2 MeV gammas will be detected.

For each Gd decay a neutron is removed from the flux, which otherwise would have entered the scintillator, interacted and possibly have been captured on hydrogen.

Therefore, an independent simulation was carried out, in which 100,000 neutrons with energies of 100 keV were sent into the detector. The energy deposited for each event was then recorded to show the spectrum in Figure 6.30:

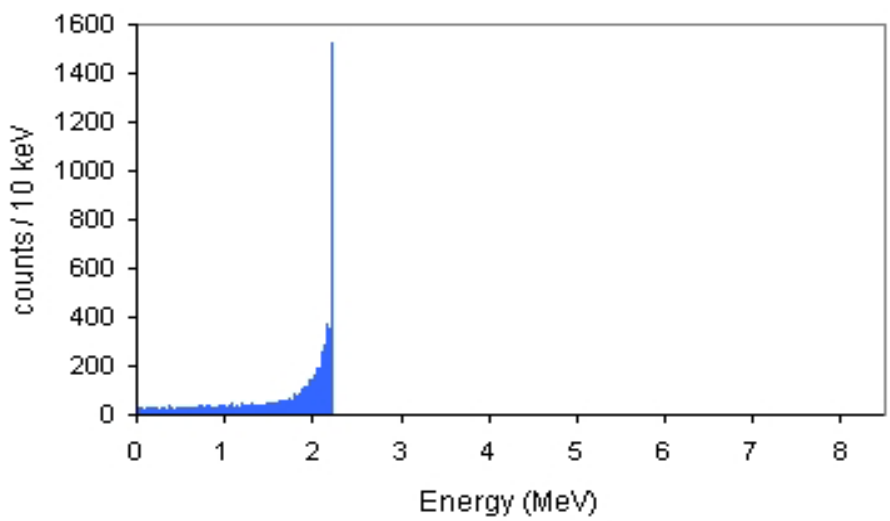

Figure 6.30: Energy deposited by the neutrons which were captured on Gd if they had entered the detector

If the thermal neutrons are captured by hydrogen nuclei, they produce deuterium by the reaction:

$$n + p \rightarrow d + \gamma$$

The binding energy of the deuteron is released in the form of a single 2.2 MeV γ ray. The energy deposited inside the detector by these gammas is shown in Figure 6.30. The energy spectrum consists of the photopeak, i.e. the spike at 2.2 MeV, and a bit of Compton Edge.

Fig. 6.31 shows the energy spectrum obtained after the signal produced by the

'surplus' of the 2.2 MeV gammas has been removed from the signal produced by the gammas emitted in Gd decay.

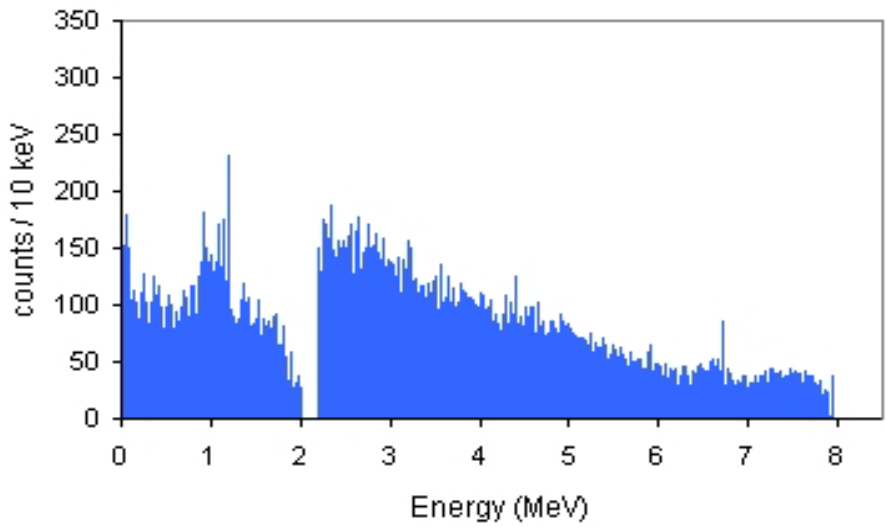

Figure 6.31: Simulated gamma energy spectrum from neutron capture on gadolinium, obtained using the parametrisation in Fig. 6.27.

An energy resolution of 35% at 0.662 MeV energy deposit was then applied, the result of this being shown in Fig. 6.32. The gap is now smeared out.

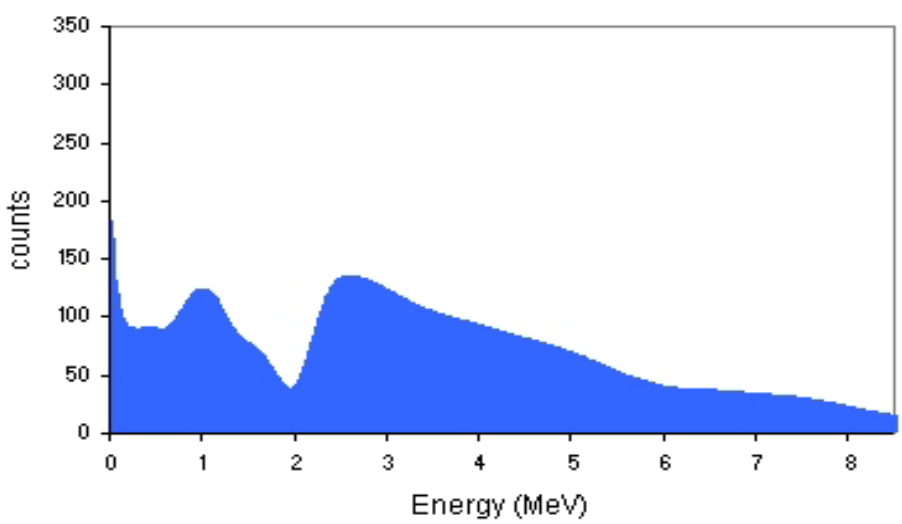

Figure 6.32: Simulated gamma energy spectrum from neutron capture on gadolinium, using the parametrisation in Fig. 6.27.

The simulated energy spectrum from neutron capture on gadolinium agrees only to some extent with the experimental measured spectrum from Gd (Fig. 5.11). This is due to the fact that this parametrisation is based on the gadolinium data measured by Groshev [64] which is characterised by a decrease in the detection efficiency with decreasing gamma energy, and this leads to efficiency corrections applied for the 1 MeV gammas which can be as high as $\sim 100\%$.
This makes the relative intensities in Fig. 6.27 unreliable for gamma energies of the order of 1 MeV.

A second parametrisation of the energy spectrum from neutron capture on gadolinium was used. This is based on a statistical model that generates gamma energies and multiplicities based on the energy and spin of the excited state (Fig. 3.4) [71]. The simulation of 2,500 decays resulted in the gamma spectrum tabulated below.

^{158}Gd decay from 7.94 MeV excited state	
Gamma Energy (MeV)	Population
0 - 1	39%
1 - 2	28%
2 - 3	20%
3 - 4	8.1%
4 - 5	3.8%
5 - 6	1.1%
6 - 7	0.1%

Table 6.2: Energies and multiplicities of gammas from neutron capture on gadolinium

This parametrisation of the Gd spectrum results in an average cascade multiplicity of 5.1 gammas, which indicates an average gamma energy of 1.56 MeV.

Following the same procedure as before, gammas were picked randomly from the above population distribution until the total energy reached or exceeded the neutron

binding energy. The last gamma energy in the cascade was truncated such that the sum energy was 7.94 MeV.

The best fit between the simulation and the real data was obtained by choosing the gamma energies to be equal to the maximum value in each energy interval in Table 6.2, allowing small random energy fluctuations around these values. This was done using a Gaussian distribution with standard deviation $\sigma = 0.2\,MeV$.

A simulation of 100,000 neutron captures on ^{158}Gd is performed, measuring the energy deposit in each event. The detector spectrum resulting from this cascade model is shown in Figure 6.33. This spectrum can be compared with Fig. 6.29 which was obtained using the Trzcinski parametrisation.

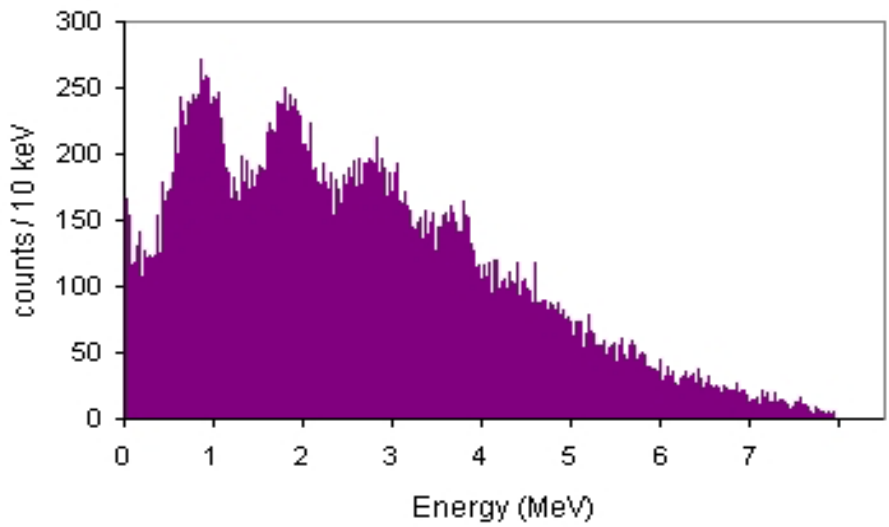

Figure 6.33: Simulation of the energy deposit by the gammas from neutron capture on gadolinium, using the parametrisation in Table 6.2.

The 'surplus' in the 2.2 MeV gamma signal in the energy deposit spectrum (see Fig. 6.30) was then subtracted as before, resulting in the energy spectrum shown in Figure 6.34:

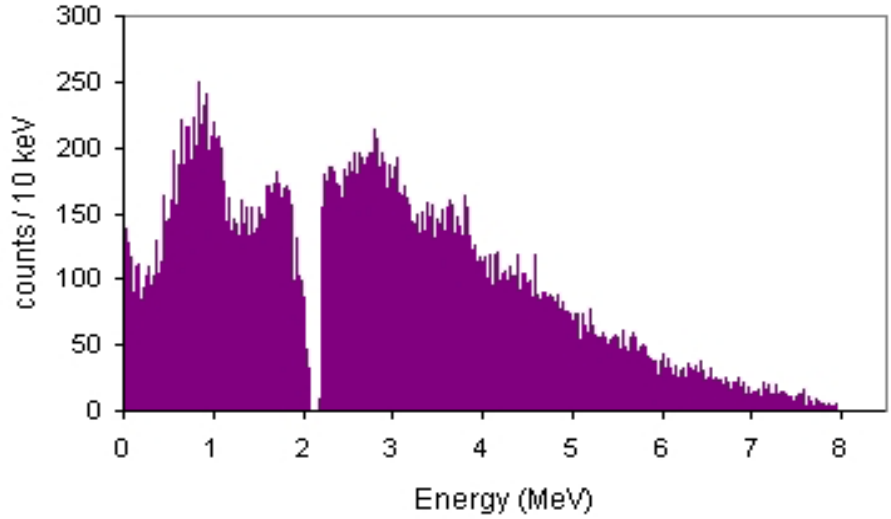

Figure 6.34: Simulated gamma energy spectrum from neutron capture on gadolinium, obtained using the parametrisation in Table 6.2

To attempt to reproduce the experimental measured spectrum, an energy resolution of 35% at 0.662 MeV was also applied to each of the energy bins in Fig. 6.34. This can be compared with the results of the smeared Trzcinski parametrisation of Fig. 6.32 and our measurement of Fig. 5.11.

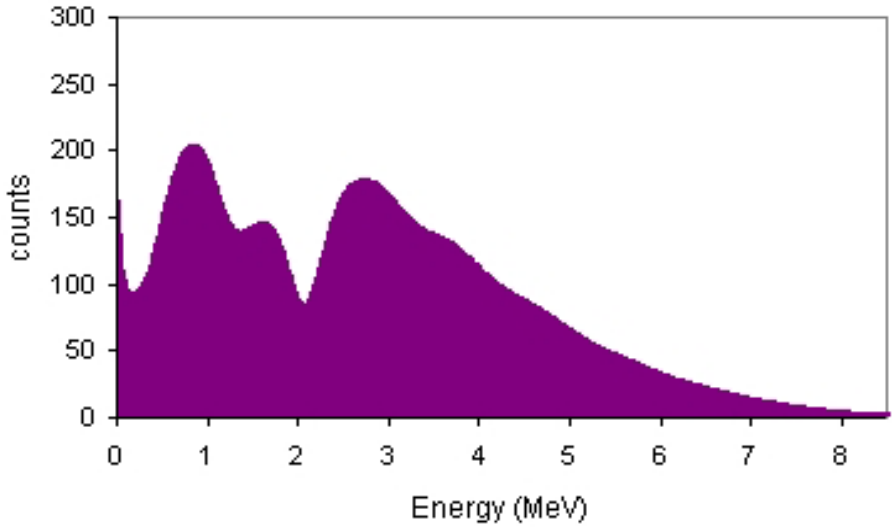

Figure 6.35: Simulation of the smeared energy deposit by the gammas from neutron capture on gadolinium

This simulated gamma energy spectrum from thermal neutron capture on gadolinium, using the statistical model of Gavron [71], agrees well with the measured spectrum (see Fig. 5.11). It can be emphasised that the failure of the Trzcinski parametrisation to reproduce the data can be ascribed to the badly known efficiency corrections in the 1 MeV region.

Chapter 7

Optimisation of Detector Dimensions

In this chapter the experimental results from tests on the prototype detector and the power of the simulation are compared to investigate possible realistic designs. It has been demonstrated that the simulation can be trusted and so various designs can be tried without having to build them and hence converge on the optimum.

7.1 Previous Design Proposals for the OMNIS Detector

The parametrisation of the Gd decay spectrum can be used for the optimisation of the design of the OMNIS detector with respect to neutron detection efficiency. A background cut on the energy deposited in the detector might be required due to the natural background in the Boulby mine in North Yorkshire, where it has been proposed that the neutron detector could be installed [17]. A 2.614 MeV gamma produced by thorium decay in the rock in the mine is the highest energy background source. Therefore, if the background cut of 3 MeV is applied, only the events resulting in an energy deposition above the background cut can be used for neutron detection. Thus the 2.2 MeV gamma signal from neutron capture on hydrogen cannot be used to identify the neutrons. This should be investigated further by making

real background measurements down the mine since the background levels in the mine are not easily simulated.

Initially it had been proposed [17] to use a configuration of the detector involving separate moderator, absorber and scintillator detector, as shown in Figure 7.1.

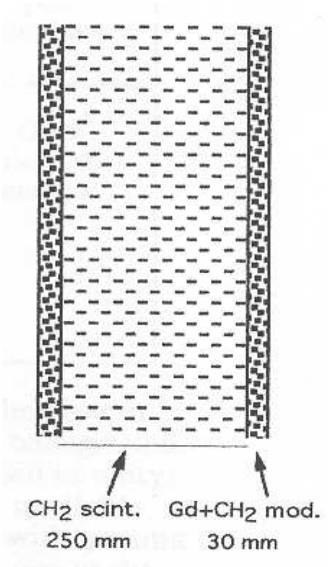

Figure 7.1: Proposed type of low energy neutron detector [17]

Separating the neutron moderator/absorber from scintillator, in place of Gd-loaded scintillator, provides a more secure long-term optical stability. This is due to the fact that in the case of Gd-loaded scintillators the uniformity of loading might not have long term stability and this could give rise to a reduction in transparency over a period of many years [73]. The use of Gd-loaded scintillators may also cause difficulties with the material containing the scintillators, due to the chemical aggressiveness of the Gd-loaded liquid scintillators.

The neutrons emerging from lead and iron targets were considered to thermalize in about 30 mm of hydrogenous material. The thermalized neutrons will then be captured by either an H or Gd nucleus. It was also believed that a thickness of $\sim$ 250 mm of scintillator would be required to convert a sufficient fraction of the

gamma energy by Compton scattering to distinguish the event unambiguously from the gamma background.

7.1.1 The proposed detector geometry for OMNIS

Figure 7.2 shows the generic principle which has been adopted for the detector design. In this detector design a bed of reprocessed lead is covered by a further 15 cm layer of new low background lead. There follows a 3 cm thick sheet of solid hydrocarbon (e.g. paraffin wax) loaded with 1% by weight Gd_2O_3 powder. The gammas emitted following the neutron capture could then be detected in so-called MACRO tanks (from the Palo Verde experiment) filled with liquid scintillator.

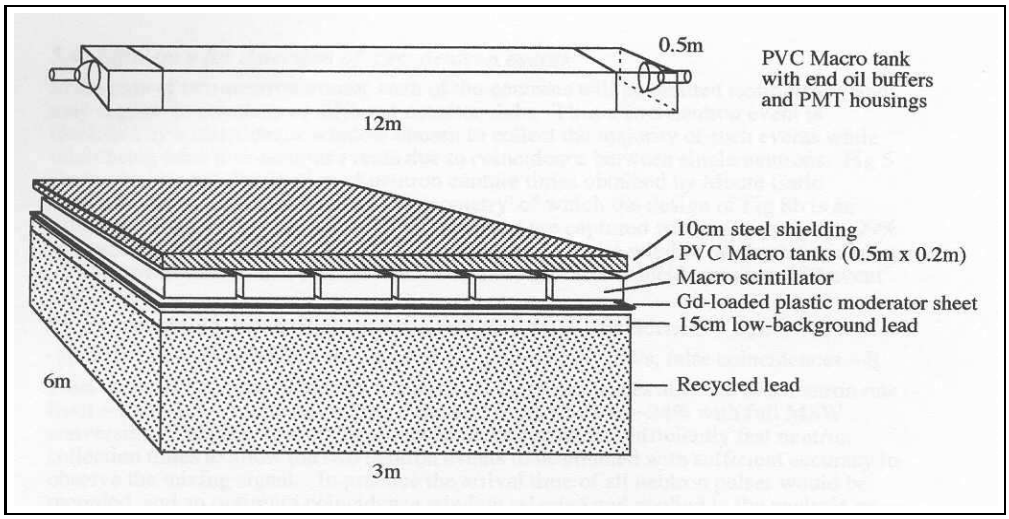

Figure 7.2: Principle of the proposed OMNIS module. Target formed from blocks of reprocessed lead shielding with gamma activity attenuated by 15 cm of new lead. Signal neutrons from target are thermalized and captured in 3 cm Gd-loaded moderator sheet, releasing gammas detected by scintillator tanks [17]

Previous Monte Carlo simulations showed that the simple 'one-dimensional' configuration (Fig. 7.2) has a neutron collection efficiency of only $\sim 20\%$. Simulations based on more efficient 'sandwich' configurations led to the design shown in Fig. 7.3 which was calculated to have a neutron collection efficiency of approximately 40% [17].

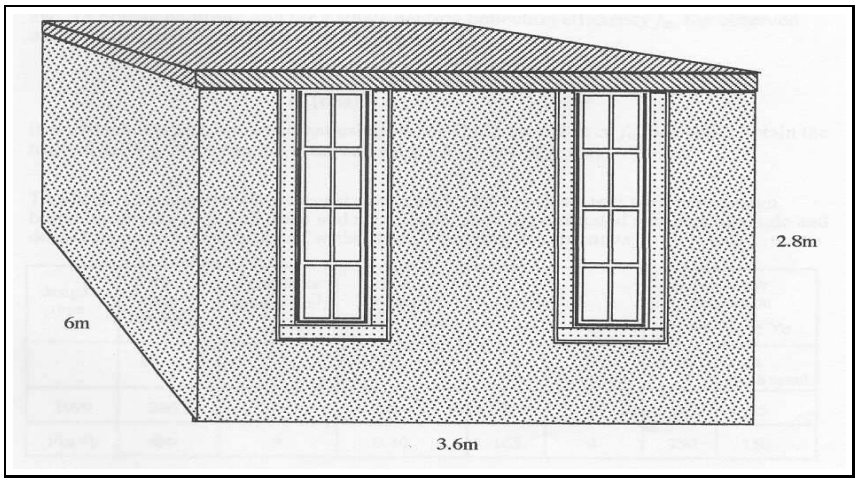

Figure 7.3: Configuration based on the principles shown in Fig. 7.2 but reshaped to give higher overall neutron detection efficiency [17]

The improvement in the neutron detection efficiency from 20% to 40% is due to a much better geometry of the detector.

It has been shown in [17] that about half of the gamma energy following the neutron capture events is lost from the scintillator boundaries, still leaving an average of 3 - 5 MeV deposited inside the detector. This deposited energy is above the gamma background (which extends to $\sim$ 2.6 MeV from Th) and therefore it can be used to identify the neutron events.

However this can now be investigated in more detail using the correct parametrisation of the Gd decay spectrum (see Section 6.5), to see if the proposed design of the detector (Fig. 7.3) can be used for neutron detection.

7.1.2 The Gd-gamma signal measured with the proposed detector design

The detector geometry described in Fig. 7.3 has been introduced into the Geant4 simulation and was used to simulate the neutron detection efficiency by generating neutrons randomly inside the target (lead) volume. The previous estimation of 40% neutron detection efficiency proved to be optimistic. The neutron detection efficiency for this detector arrangement (Fig. 7.3) has been simulated to be equal to only 22%. The energy spectrum obtained by simulating 100,000 neutron signal events is shown in Fig. 7.4.

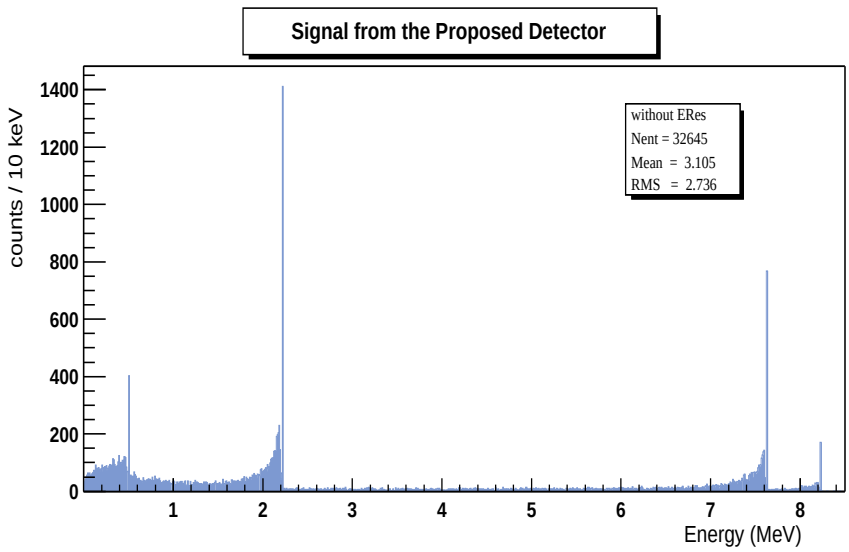

Figure 7.4: The signal produced by the neutrons generated inside the proposed detector (see Fig. 7.3)

From the 100,000 simulated events events 13.8% result in neutron capture on protons inside the liquid scintillators and only 8.2% result in neutron capture on gadolinium. As shown in Section 6.4 the presence of Gd does not affect the neutron containment efficiency and therefore this is not the reason why the neutron detection efficiency is equal to only 22%. The neutron detection efficiency is determined by the fraction of the neutrons which are thermalized inside the moderator (paraffin wax or scin-

tillator). Once thermalized the neutrons may be captured on Gd or protons, and different values of the Gd concentration will only affect the ratio of the number of events resulting in neutron capture on Gd and those resulting in neutron capture on protons inside the scintillators.

So far, the effect of the background cut on the neutron detection efficiency has been ignored. As mentioned above, only the Gd-decay gammas can be used for neutron identification, if a background cut at 3 MeV is applied to the measured spectra. The same detector geometry (Fig. 7.3) was used to simulate the response of this detector to the Gd-decay gammas. The gammas emitted in the Gd-decay were generated randomly at the detector boundaries, using the same procedure as in Section 6.5. The energy deposited inside the detector was measured for each event, resulting in the energy spectrum shown in Figure 7.5.

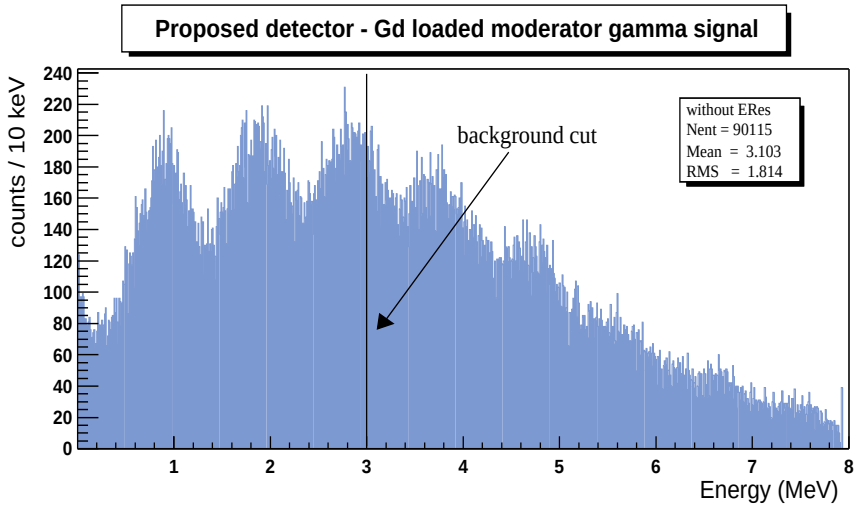

Figure 7.5: The energy deposited by the Gd gammas inside the proposed neutron detector

From the 100,000 simulated events 8.2% resulted in neutron capture on Gd. Only approximately 43.5% of these events result in an energy deposition above the background cut at 3 MeV.

Therefore the overall neutron detection efficiency for this detector design (Fig. 7.3) is equal to only 3.6%.

As most of the neutrons leave the detector via the outer surface of the lead layer, it has been also proposed [72] 'to turn the detector inside out', i.e. to use a lead centred detector.

A 1.5 m thick scintillator surrounding 1 m^3 of lead (see Fig. 7.6) has been considered in order to determine the neutron detection efficiency for this new proposal.

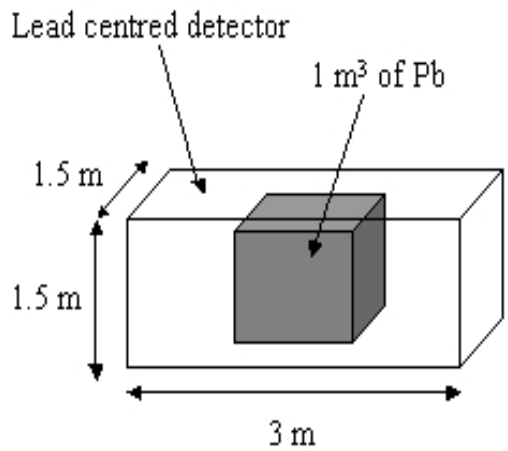

Figure 7.6: Lead centred scintillator detector

Again 100,000 neutrons were generated randomly inside the lead target, resulting in the following expected energy spectrum shown in Fig. 7.7.

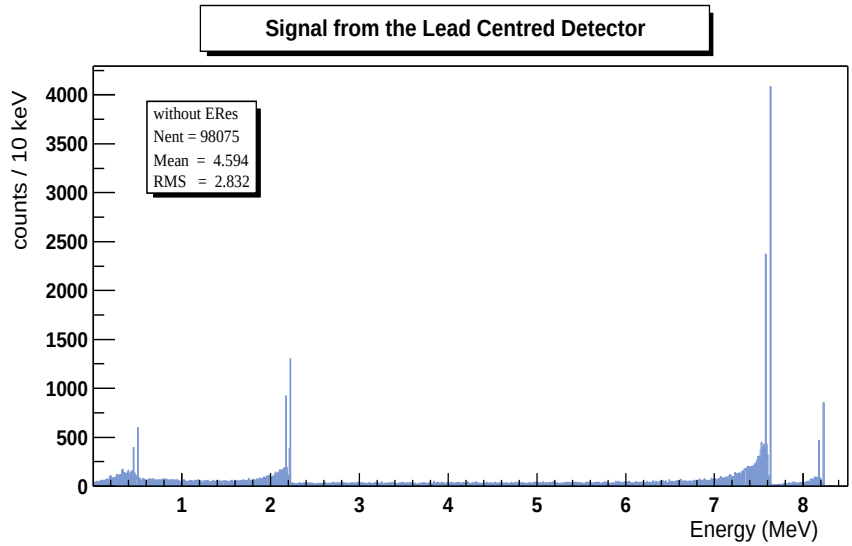

Figure 7.7: The signal produced by the neutrons generated inside the lead centred detector

As mentioned above, the presence of Gd inside the scintillator does not affect the neutron containment efficiency, but only the energies of the gamma rays emitted following the neutron capture processes. Therefore, for simplicity, the Gd was uniformly distributed inside the scintillator, with 0.1% Gd by weight.

For this detector geometry the neutron detection efficiency has increased to 57% (no background cut being applied).

However the disadvantage for this detector design is that it requires up to 5.75 m^3 of scintillator for 1 m^3 of lead. As the number of events produced by the neutrino-nucleus interactions is proportional to the volume of lead target, the number of neutron signal events is proportional to the product between the neutron detection efficiency ϵ_n and the lead target volume V_t:

$$N_{events} \propto \epsilon_n \times V_t \tag{7.1}$$

Therefore this detector arrangement (Fig. 7.6) would require at least three times

more scintillator material than it was initially proposed (see Fig. 7.3), to detect the same number of events as detected with the initial detector design.

In the following section the possibility of a better detector design with respect to the neutron detection efficiency is analysed taking into account the background cut at 3 MeV deposited energy.

7.2 Optimisation of Detector Size and Geometry

Different detector dimensions have been considered in order to determine the optimum configuration that would increase the fraction of energy from Gd-decay that is deposited inside the detector and therefore would allow the signal to be distinguished unambiguously from the gamma background.

The gammas from Gd decay were generated at the detector boundaries, using the same procedure as in Section 6.5. The detector size was modified from $20 \times 20 \times 600\,cm^3$ to $100 \times 100 \times 600\,cm^3$. The energy deposition spectra simulated for these detector sizes are shown in Fig. 7.8 - 7.12:

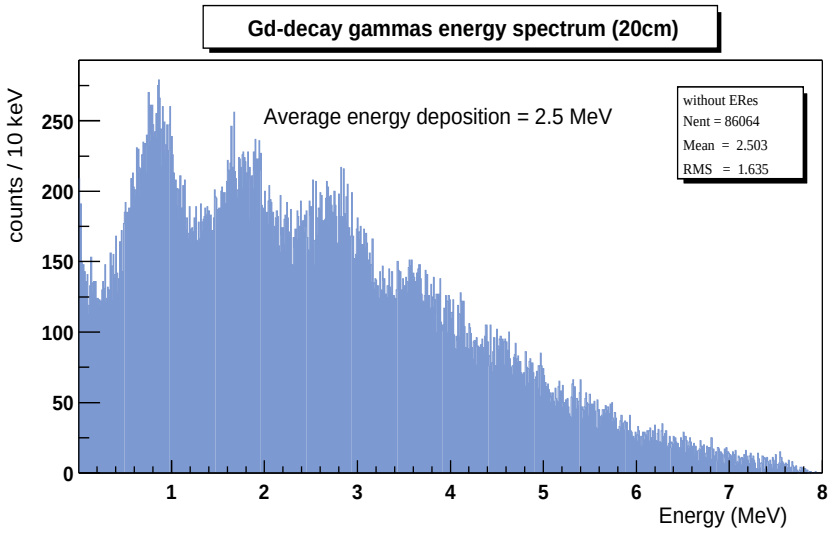

Figure 7.8: Energy spectrum produced by gammas from Gd-decay, measured with a 20 cm thick scintillator (average energy deposition = 2.5 MeV)

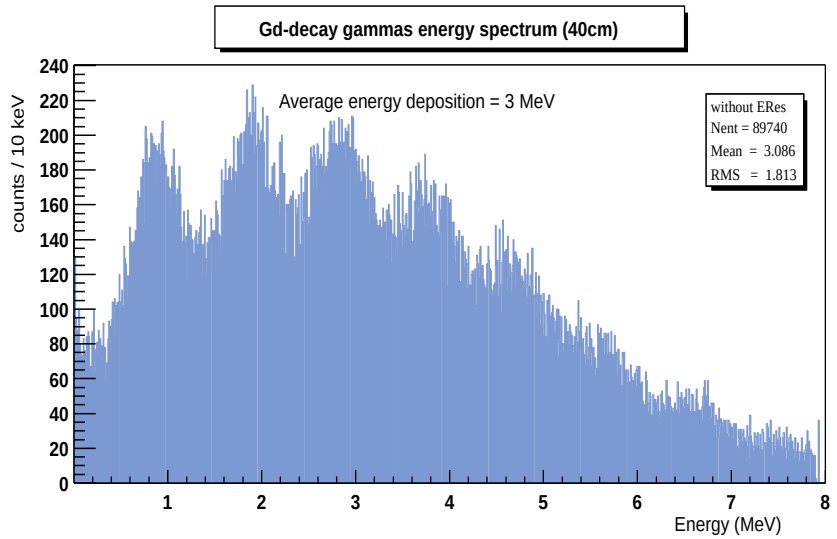

Figure 7.9: Energy spectrum produced by gammas from Gd-decay, measured with a 40 cm thick scintillator (average energy deposition = 3 MeV)

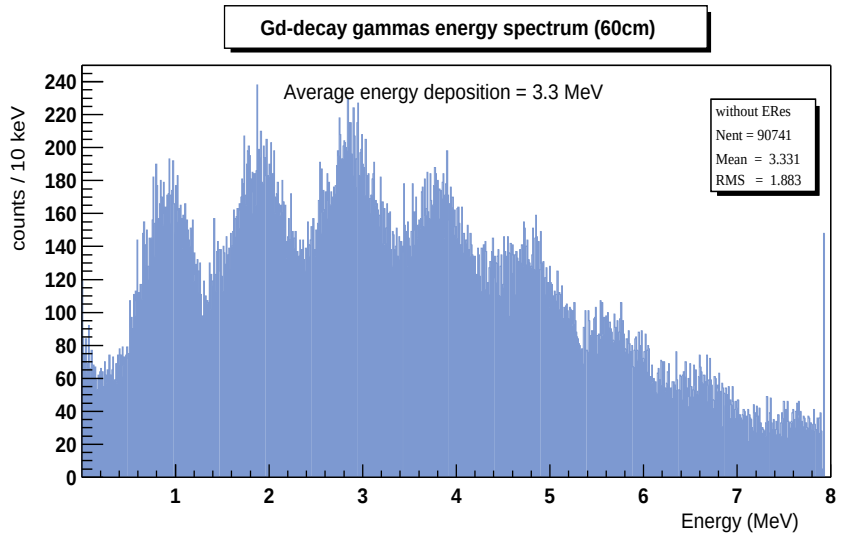

Figure 7.10: Energy spectrum produced by gammas from Gd-decay, measured with a 60 cm thick scintillator (average energy deposition = 3.3 MeV)

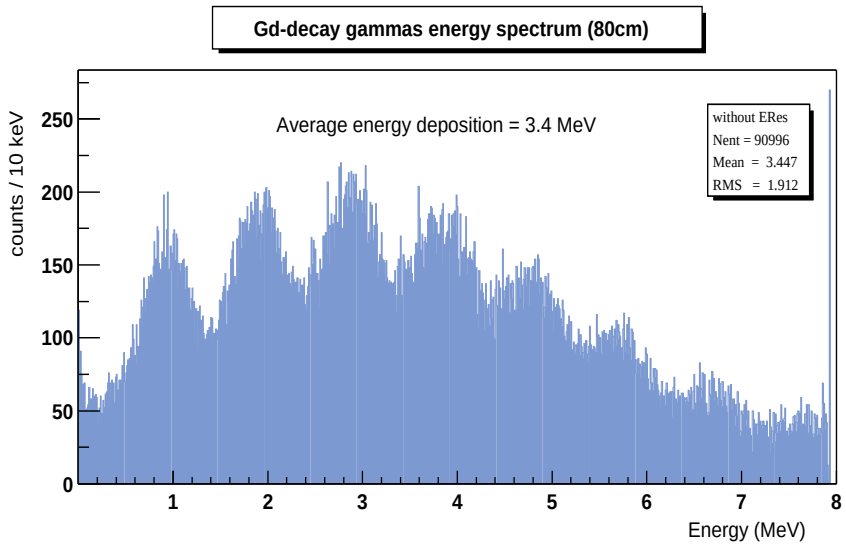

Figure 7.11: Energy spectrum produced by gammas from Gd-decay, measured with an 80 cm thick scintillator (average energy deposition = 3.4 MeV)

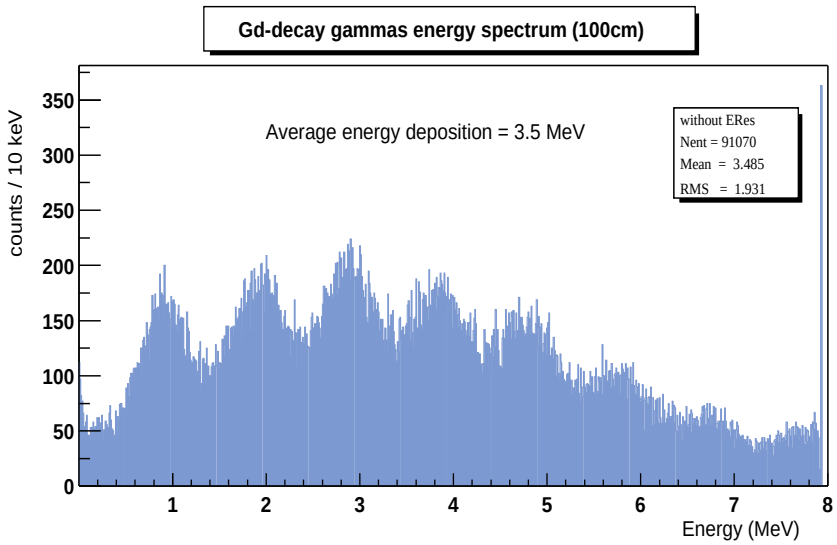

Figure 7.12: Energy spectrum produced by gammas from Gd-decay, measured with a 1 m thick scintillator (average energy deposition = 3.49 MeV)

The average energy deposition increases from 2.5 MeV (for a 20 cm thick scintillator) to ∼3.5 MeV (for a 100 cm thick scintillator). However there is no significant increase in the average energy deposition for a scintillator thickness greater than 60 cm.

Again the same 'Macro tanks' filled with liquid scintillator described in Fig. 7.2 and 7.3 were used to simulate a new detector set up shown in Fig. 7.13.

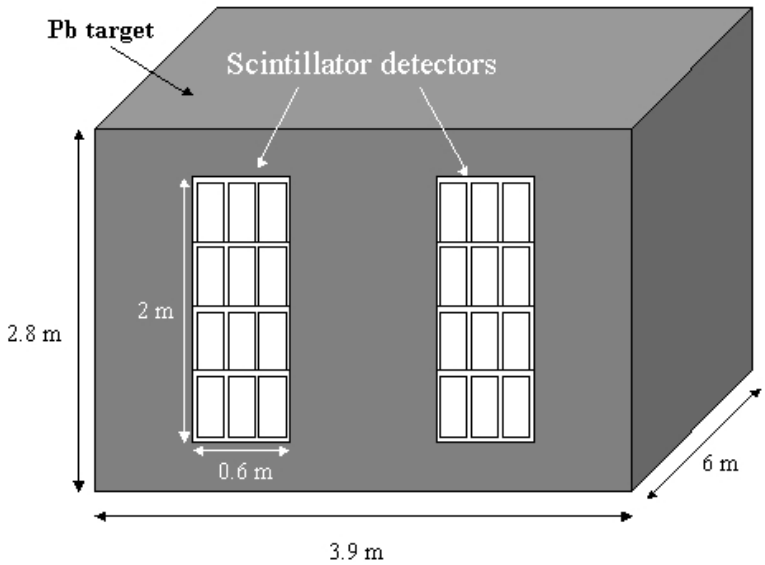

Figure 7.13: The optimum detector size and geometry as scintillator blocks surrounded by lead target

The energy spectrum obtained for this experimental set up is shown in Fig. 7.14.

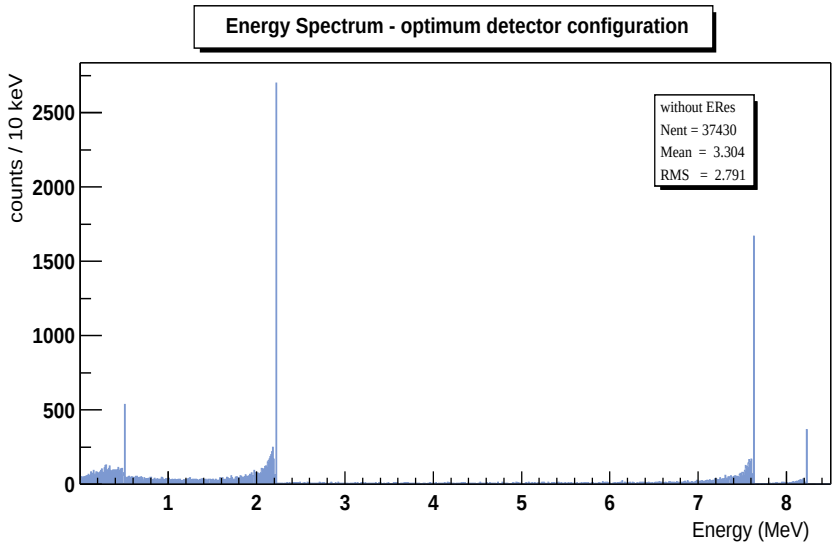

Figure 7.14: The energy spectrum measured with the optimum configuration of the neutron detector

For this configuration of the detector, the neutron detection efficiency is equal to 25.8%.
From the 100,000 simulated events events, 10% result in neutron capture on gadolinium.

An independent simulation has been performed to measure the energy deposition spectrum due to the Gd-decay gammas generated at the scintillators boundaries in Fig. 7.13. The result is shown in Fig. 7.15, for a background cut at 3 MeV.

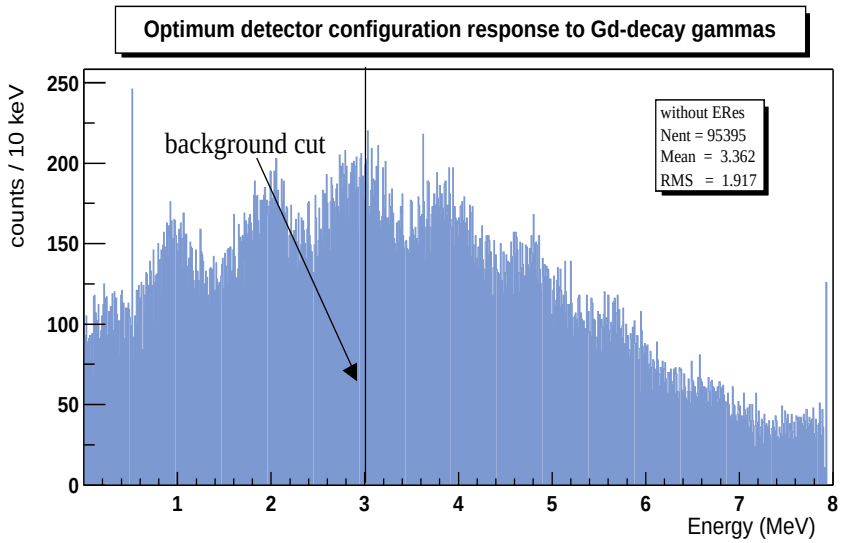

Figure 7.15: The energy spectrum from Gd-decay gammas measured with the optimum configuration of the neutron detector

It can be seen that a better signal-background discrimination can be achieved with the latter detector set up, as approximately 51.8% of the events result in an energy deposition above the background cut. Therefore the detector arrangement shown in Fig. 7.13 proves to be a better configuration compared to the one which was initially proposed (see Fig. 7.3).

This implies that the overall neutron detection efficiency for a 3 MeV cut has increased from 3.6% to 5.2%.

It is clear from all these considerations that the relatively high threshold of the 3 MeV cut is a significantly dominant feature contributing to the low efficiency. It is therefore desirable to consider ways in which this threshold might be reduced.
Neutrons and gamma backgrounds in the Boulby Mine have been previously studied in considerable detail for the design and interpretation of dark matter experiments [17]. It was found that the mean gamma background is largely time independent and can therefore be subtracted reliably. This would allow the 2.2 MeV gamma signal to be used for neutron identification and would significantly increase the neutron detection efficiency.

In order to illustrate this, the photo-peaks in Fig. 7.14 due to Gd-decay gammas have been replaced with the correct energy spectrum shown in Fig. 7.15, resulting in the following energy spectrum:

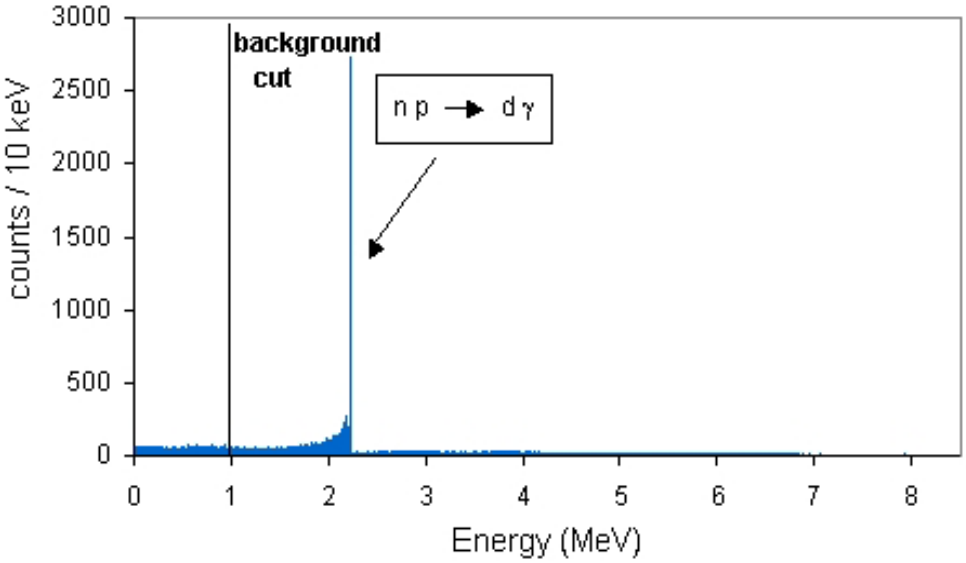

Figure 7.16: The simulated response of the detector to neutrons

As mentioned above, only 10% of the event result in neutron capture on Gd, and 15.8% result in neutron capture on protons inside the scintillators. It can be seen that the photo-peak due to the 2.2 MeV gammas from neutron capture on protons is the dominant signal in the gamma energy spectrum.

For a background cut at 1 MeV, the neutron detection efficiency increases from 5.2% (for a 3 MeV cut) to 20.4%.

7.3 The Possibility of Using Gd-loaded Scintillators

If the background cut at 3 MeV is applied to the measured spectra, the neutron detection efficiency is reduced for the optimum detector configuration from $\sim 26\%$ to only 5%. In this case a possible solution would be to use Gd-loaded scintillators. The use of Gd-loaded scintillators has the basic merit that the detector, the neutron moderator and the absorber are uniformly mixed, giving the best conditions for high detection efficiency.

This configuration was investigated and the results are presented here.
The energy spectrum measured with Gd-loaded scintillators, using the same detector geometry as in Fig. 7.13, is shown in the following figure:

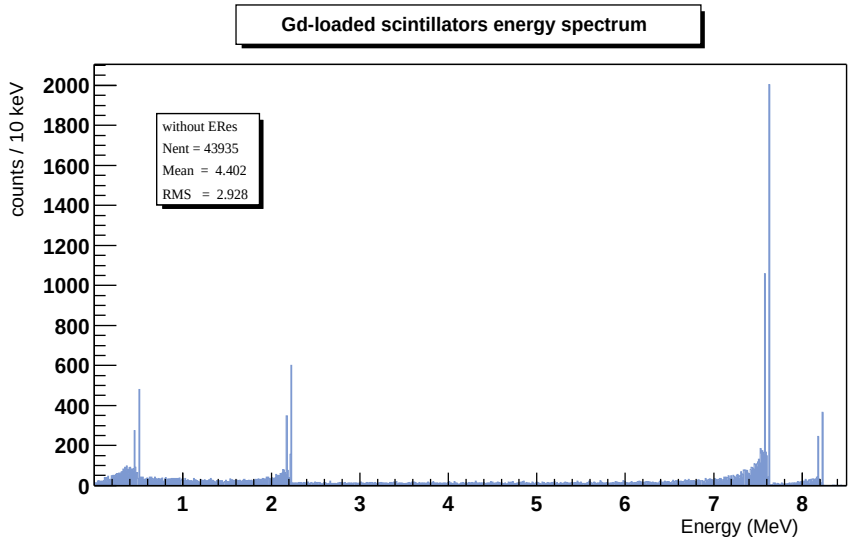

Figure 7.17: The energy spectrum measured with gadolinium loaded scintillators

The neutron detection efficiency for Gd-loaded scintillators is now equal to 24.7%.

From the 100,000 simulated events, 15.1% result in neutron capture on Gd, from which 79.5% will result in an energy deposition above the 3 MeV cut, as shown in

Fig. 7.18.

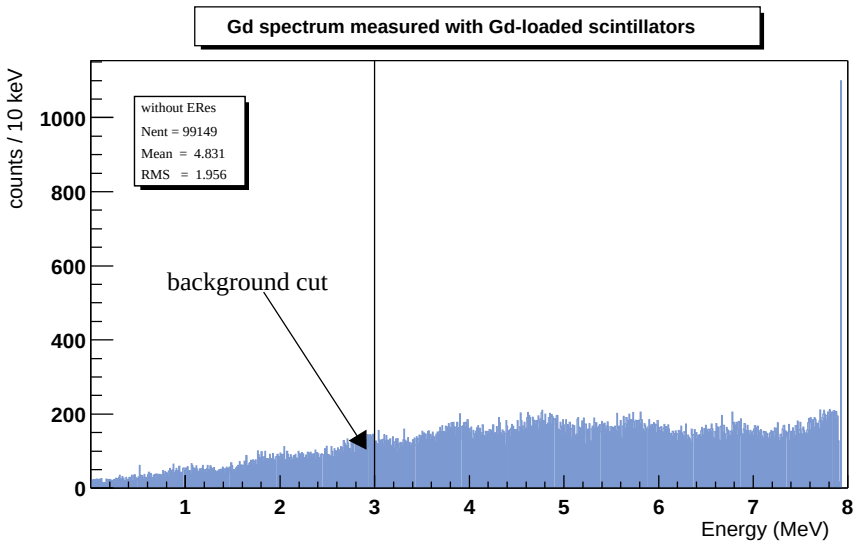

Figure 7.18: The energy spectrum from Gd-decay gammas measured with the Gd-loaded scintillators

If the 3 MeV cut is applied, the neutron detection efficiency of the Gd-loaded scintillators is equal to 12%.

As mentioned above, the mean gamma background is largely time independent and a background cut at 3 MeV may prove to be unnecessary. In this case, the use of Gd-loaded scintillators is no longer justified. The experimental set up described in Fig. 7.13 has a neutron detection efficiency of $\sim$ 26% (20.4% for a background cut at 1MeV) and proves to be the optimum configuration of the neutron detector.

Chapter 8

Summary and Conclusions

A full self-consistent simulation of the neutron detector was undertaken using the GEANT4 simulation code. The deposition of energy by neutrons was calculated on a step-by-step basis as secondary particles were tracked.

The neutron detector was calibrated and its energy resolution measured to be equal to 28.5% for a 1 MeV energy deposition inside the detector. A calibration experiment has been undertaken using several known gamma sources. Data from this experiment were compared with a detailed simulation using GEANT and show excellent agreement.

The GEANT simulation can be easily extended to any size and geometry of the detector, and was used to analyse and calibrate the neutron detection efficiency for various detector geometries.

For the optimum configuration of the detector (Fig. 7.13), $\sim 26\%$ of the neutrons are captured producing gammas which will interact through Compton scattering. These events are then converted into a signal leading to the detection of the original neutrino-nucleus interaction.

The parametrisation of the Gadolinium decay spectrum has been improved, enabling a more accurate simulation of the neutron's detection. The model shows very

good correlation with the measured spectrum, and the energy selection method is consistent with the genuine gamma decays. This allows the efficiency for detecting neutrons to be determined absolutely.

Different geometries of the detector were introduced into the GEANT4 simulation to study the response to the neutrons produced in the lead target and to determine the optimum detector configuration with respect to the neutron detection efficiency.

If a background cut of 3 MeV is applied then the neutron detection efficiency for the optimum configuration of the detector is reduced from ∼26% to 5.2%, while for Gd-loaded scintillators it is equal to 12%.

However, if the background cut can be reduced from 3 MeV to 1 MeV, this will result in a neutron detection efficiency of 20.4% for the experimental set up described in Fig. 7.13, which was found to be the optimum configuration of the neutron detector.

Appendix

Property	Measurement
Polymer Base	Polyvinyltoluene
Density	$1.032 g/cc$
Refractive Index	1.58
Light Output Temperature Dependence	At $+60°C = 95\%$ of that at $+20°C$; independent of temperature from $-60°C to + 20°C$
Light Output, % Anthracene	60
Rise Time, ns	1.0
Decay Time, ns	3.3
Pulse Width FWHM, ns	4.2
Light Attenuation Length, cm	400
Wavelength of Max. Emission, nm	434
No. of H Atoms per cm^3,($\times 10^{22}$)	5.23
No. of C Atoms per cm^3,($\times 10^{22}$)	4.74
Ratio H:C Atoms	1.104
No. of Electrons per cm^3,($\times 10^{23}$)	3.37
Principal uses/applications	general purpose

Table 8.1: Properties of NE110 plastic scintillators stated by the manufacturer

References

[1] H. Muayama "The origin of neutrino mass", Physics World, May 2002.

[2] The Standard Model
$http://www-donut.fnal.gov/web_pages/standardmodelpg/TheStandardModel.html$

[3] Y. Fukuda *et al.* "Evidence for oscillation of atmospheric neutrinos", Phys. Rev. Lett. 81 (1998) 1562.

[4] S. M. Bilenky, C. Giunti and C. W. Kim, Int. J. Mod. Phys. A 15 (2000) 625.

[5] Zatsepin, G. I., JETP Lett. 8 205, (1968).

[6] Y.-Z. Qian *et al.*, Phys. Rev. Letters 71, 1965 (1993).

[7] A. Colgate and R. H. White, Astrophys. J. 143, 626 (1966); J. R. Wilson *et al.*, Ann. N.Y. Acad. Sci. 470, 267 (1986); J. N. Bahcall, A. Dar., and T. Piran, Nature 326, 155 (1987).

[8] W. Kunkel. and B. Madore, IAU Circular No. 4316 (24 February 1987).

[9] Particle Physics Experiments Selection Panel Members.

[10] R. G. Strom, Astron. Astrophys., 288, L1-L4 (1994).

[11] B. Aschenbach, Nature 396, 141 (1998)

[12] Bionta R. M., *et al.*, 1987, Phys. Rev. D 38, 768.

[13] S. Van der Bergh, G. Tammann, Ann. Rev. Astron. Astrophys. 29, 363 (1991).

[14] Y. Totsuka, Rep. Prog. Phys. (1992) 377.

[15] S.M. Bilenky *et al.*, "Absolute Values of Neutrino Masses: Status and Prospects", hep-ph/0211462.

[16] D.B. Cline *et al.*, Phys. Rev. D 50 (1994) 720.

[17] *Omnis − Siren Proposal*, Manchester University, Imperial College of Science, Technology and Medicine, RAL, Sheffield University and Queen Mary & Westfield College.

[18] G. Raffelt, "Stars as Laboratories for Fundamental Physics" (Chicago, 1996) 395.

[19] R. M. Bionta *et al.*, The IMB Collab., Phys. Rev. Lett. 58, 1494 (1987).

[20] K. Hirata *et al.*, The Kamiokande II Collab., Phys. Rev. Lett. 58, 1490 (1987).

[21] E. Kolbe and K. Laganke, LANL preprint server, nucl-th/0003060, 27 Mar 2000.

[22] M. Boezio *et al.*, Phys. Rev. Lett. 82 24 (1999) 4757.

[23] R. Becker-Szendy *et al.*, Phys. Rev. D 46 9 (1992) 3720.

[24] W.W.M. Allison *et al.*, Phys. Lett. B, 449 (1999) 137.

[25] Y. Fukuda *et al.* (Kamiokande collaboration) Phys. Rev. Lett. 77 9 (1996) 1683.

[26] John Bahcall Homepage - Institute for Advanced Study
http://www.sns.ias.edu/ jnb/

[27] N. Fornengo, M.C. Gonzales-Garcia and J.W.F Valle, Nucl. Phys. B 580 (2000) 58.

[28] B.T. Cleveland *et al.*, Nucl. Phys. B, Proc. Suppl. 38 (1995) 47.

[29] K.S. Hirata *et al.*, Phys. Lett. B 280 (1992) 146.

[30] S. Wanninger *et al.*, Phys. Rev. Lett. 83 6 (1999) 1088.

[31] G.M. Fuller, W.C. Haxton and G.C. McLaughlin "Prospects for Detecting Supernova Neutrino Flavor Oscillations", astro-ph/9809164.

[32] D.B. Cline *et al.*, Phys. Rev. D 50 (1994) 720.

[33] A. Burrows, Ann. Rev. Nucl. Part. Sci. 40 (1990) 181.

[34] J.N. Abdurashitov *et al.*, Phys. Rev. Lett. 83 23 (1999) 4686.

[35] Y. Fukuda *et al.*, (Super-Kamiokande collaboration), Phys. Rev. Lett. 82 (1999) 2430.

[36] D.B. Cline, G.M. Fuller, W.P. Hong, B. Meyer and J. Wilson, Phys. Rev. D 50 (1994) 720.

[37] Neutron Interactions - MIT Deprtment of Nuclear Engineering 22.104 Spring 2002
$http://web.mit.edu/22.09/ClassHandouts/NeutronsS2002.PDF$

[38] NIST Centre for Neutron Research - Neutron scattering lengths and cross sections
$http://www.ncnr.nist.gov/resources/n-lengths/$

[39] L. V. Groshev, V. N. Lutsenko, A. M. Demidov, and V. I. Pelekov, "Atlas of Gamma Spectra from Radiative Capture of Thermal Neutrons", Pergamon Press, Inc., New York, 1959).

[40] NIST XCOM: Photon Cross Sections Database
$http://physics.nist.gov/PhysRefData/Xcom/Text/XCOM.html$

[41] Compton Scattering
$http://hyperphysics.phy-astr.gsu.edu/hbase/quantum/comptint.html$

[42] NIST X-Ray Mass Attenuation Coefficients
$http://physics.nist.gov/PhysRefData/XrayMassCoef/cover.html$

[43] Birks, J.B. Scintillation Counters. London: Pergamon Press, 1960.

[44] *RCA Photomultiplier Manual*, Technical Series PT-61, RCA Solid State Division, Electro-Optics and Devices, Lancaster, PA. (1970).

[45] Turner, James. Atoms, Radiation, and Radiation Protection. New York: McGraw-Hill Co., Inc., 1992.

[46] Meyerhof, Walter. Elements of Nuclear Physics. New York: McGraw-Hill Co., Inc., 1967.

[47] J. Byrne, "Neutrons, Nuclei and Matter - An Exploration of Physics of Slow Neutrons", p317, IOP Publishing Ltd 1994.

[48] A.F. Henry "Nuclear - Reactor Analysis", p90, The MIT Press 1975.

[49] A. Trzcinski *et al.*, "A Monte-Carlo Code for Neutron Efficiency Calculations for Large Volume Gd-Loaded Liquid Scintillation Detectors", GSI Report 98-07 Oktober 1998.

[50] J.J. Zach *et al.*, "Optimization of the Design of OMNIS, the Observatory of Multiflavor Neutrinos from Supernovae", nucl-ex/0205011.

[51] K.S. Krane, "Introductory Nuclear Physics", p448, Wiley & Sons, (1988).

[52] A. Piepke, "Note on the calibration of a 9 m cell using compton edges of γ point sources", California Institute of Technology internal report (1995) unpublished.

[53] Knoll, G.F, 'Radiation Detection and Measurement', p251-254, Wiley & Sons, (1989).

[54] Knoll, G.F, 'Radiation Detection and Measurement', p256-257, Wiley & Sons, (1989).

[55] Knoll, G.F, 'Radiation Detection and Measurement', p259, Wiley & Sons, (1989).

[56] H. Rauch, M. Zawisky, Ch. Stellmach and P. Geltenbort, Phys Rev Letts. 83, 4955 (1999).

[57] Malamatenia Avgoulea "The Measurement and Simulation of Light Yield from Plastic Scintillators", January 2002 unpublished.

[58] Knoll, G.F, 'Radiation Detection and Measurement', p729, Wiley & Sons, (1979).

[59] Evaluated Nuclear Data File (ENDF) - ENDF/B-VI library
$http://www.nndc.bnl.gov/exfor/endf00.htm$

[60] E.A. LORCH, Int. J. Appl. Radiat. Isotopes, 24, 588-9, 1973.

[61] GEANT Detector Description and Simulation Tool, CERN program library, CERN-CN Division, Geneva, Switzerland. GEANT ver. 5.0 - Patch 01 and G4NDL ver. 3.7 were used.

[62] GEANT4 - a simulation toolkit, GEANT4 Collaboration, Preprint submitted to Elsevier Science, 8 August 2002.

[63] Hans-Peter Wellisch, CERN, private communication (2003).

[64] L.V. Groshev, A.M. Demidov, V.A. Ivanov, V.N. Lutsenko and V.I. Pelekhov, $Izv. Akad. Nauk SSSR (Ser. Fiz.)$, **26**, 1119 (1962).

[65] J. Klora *et al.*, Nucl. Phys. A, **561**, 1 (1993).

[66] A. Bäcklin *et al.*, Nucl. Phys. A, **380**, 189 (1982).

[67] R.G. Helmer, Nucl. Data Sheets, **65**, 65 (1992).

[68] R.C. Greenwood *et al.*, Nucl. Phys. A, **304**, 327 (1978).

[69] M.A. Lee, Nucl. Data Sheets, **56**, 199 (1989).

[70] A. Gilbert and A. G. W. Cameron, Can. J. Phys. 43 (1965) 1446.

[71] A. Gavron, "Statistical-Model Calculations with Angular-Momentum Coupling" in *Computational Nuclear Physics 2 : Nuclear Reactions*, ed. K. Langanke, J.A. Maruhn, S.E. Koonin, Springer-Verlag, New York, N.Y. (1993); the code was run by Dr. Karlheinz Langanke.

[72] D. South, First Year PhD Transfer Report, Dept. of Physics & Astronomy, Univ. of Manchester, May 2000.

[73] A.G. Piepke, S.W. Moser, V.N. Novikov, Nucl. Instrum. Meth. A432 (1999) 392.